Iowa State University
Digital Repository

2009

Direct analysis of samples by mass spectrometry: From elements to bio-molecules using laser ablation inductively coupled plasma mass spectrometry and laser desorption/ionization mass spectrometry

David C. Perdian
Iowa State University

Recommended Citation

www.manaraa.com

Direct analysis of samples by mass spectrometry:

From elements to bio-molecules using laser ablation inductively coupled plasma mass

spectrometry and laser desorption/ionization mass spectrometry

by

David C. Perdian

A dissertation submitted to the graduate faculty

in partial fulfillment of the requirements for the degree of

DOCTOR OF PHILOSOPHY

Major: Analytical Chemistry

Program of Study Committee:
R. Sam Houk, Major Professor
Joseph Burnett
Victor S.-Y. Lin
Marek Pruski
Patricia Thiel

Iowa State University

Ames, Iowa

2009

TABLE OF CONTENTS

ABSTRACT

Mass spectrometric methods that are able to analyze solid samples or biological materials with little or no sample preparation are invaluable to science as well as society. Fundamental research that has discovered experimental and instrumental parameters that inhibit fractionation effects that occur during the quantification of elemental species in solid samples by laser ablation inductively coupled plasma mass spectrometry is described. Research that determines the effectiveness of novel laser desorption/ionization mass spectrometric methods for the molecular analysis of biological tissues at atmospheric pressure and at high spatial resolution is also described. A spatial resolution is achieved that is able to analyze samples at the single cell level.

CHAPTER 1 – GENERAL INTRODUCTION

Analytical methods that provide a means for the direct analysis of solid samples are valuable to countless areas of fundamental and applied research, as well as many practical applications. The direct analysis of inorganic, organic, and biological materials is often required for geological, environmental, material science, forensic science, and biological fields. Motivation behind the need for methods able to perform direct analysis of samples is as varied as their uses, but the major reasons include decreased or no sample preparation which leads to higher throughput, and the ability to gain knowledge of spatial composition of the sample.

Analysis using mass spectrometry offers many advantages over other analytical techniques. Mass spectrometry is both a qualitative and quantitative technique. Most mass spectrometric methods are very sensitive and have large dynamic ranges. Depending on the ionization source either elemental or molecular analysis can be performed. Mass spectrometry also offers the ability to perform isotopic analysis which is either impossible or very difficult to perform via spectroscopic techniques.

ELEMENTAL ANALYSIS BY LASER ABLATION INDUCTIVELY COUPLED PLASMA MASS SPECTROMETRY

The inductively coupled plasma (ICP) was first developed as an emission source for atomic spectroscopy[1], and has since become an invaluable tool for elemental analysis. Houk et al.

were the first to use the ICP as an ion source for the mass spectral analysis of elements in 1980.[2] ICP mass spectrometry (ICP-MS) is routinely used to analyze samples that are in a solution, usually aqueous with a small percentage (1-5%) of acid, by spraying the solution into the ICP with a nebulizer. Excess solvent is usually removed by a spray chamber or other type of desolvator before being introduced into the plasma.

The use of ICP-MS for elemental analysis of solid samples by laser ablation inductively coupled plasma mass spectrometry (LA-ICP-MS) was first carried out by Alan Gray in 1985[3], just five years after the ICP was first used as an ion source MS analysis. In this experimental setup the sample is placed in an ablation cell, which has inlet and outlet for a carrier gas to flow through the cell. The top of the ablation cell has a transparent cover so that the laser can be focused onto the sample. The carrier gas, typically argon or helium, then transports aerosol particles that are created by the laser ablation event to the plasma for subsequent vaporization, atomization, ionization, and extraction of ions by the mass spectrometer. Since 1985 LA-ICP-MS has steadily grown to become a valuable technique for the direct elemental analysis of solid samples. The use of LA-ICP-MS has shown to be a valuable tool for fundamental research as well as applications in the geochemical[4-6], biological[7, 8], environmental[9, 10], material science[11], forensic science[12] and semiconductor fields[13].

Quantification of elements by LA-ICP-MS is hindered by a phenomenon collectively referred to as fractionation effects. Fractionation causes a discrepancy between the analyte ratios that are measured and the stoichiometry of the original sample.[14] There are two main areas in which fractionation effects can occur, during the laser ablation event and during the

vaporization phase in the plasma. During the ablation event the absorption of laser energy heats the sample. This heating can cause the preferential vaporization of more volatile elements. The aerosol particles that are produced by subsequent laser shots have a different analyte stoichiometry than the bulk sample. This phenomenon has been described as LA-induced fractionation.

Many experimental parameters affect the severity of LA-induced fractionation effects during a LA-ICP-MS experiment. The biggest factors that affect the laser ablation event are the wavelength of the laser, the pulse width of the laser, and the type of carrier gas used to transport the aerosol particles to the ICP. The wavelength of the laser has a profound effect on the absorption of light by the sample.[15-17] It has been observed that shorter UV wavelengths allow for more direct absorption of the laser by the sample causing less fractionation.[16] Shorter wavelengths also produce signals with better reproducibility for multiple analyses, yielding lower relative standard deviation percentages.[17] The noble gas used as the carrier gas also has an effect on the level of fractionation seen.[18, 19] Helium, having a higher thermal conductivity is able to dissipate energy away from the laser ablation area reducing the amount of agglomeration and limiting the growth of large aerosol particles.[18] Helium also creates an environment that is less amendable for a laser-induced plasma to form, which promotes the formation of large agglomerations of particles.[18]

The pulse width of the laser has been found to have arguably the most significant impact on the level of fractionation observed.[20-25] Lasers with femtosecond long pulse widths have shown to exhibit significantly less fractionation effects than lasers with pulse widths in the nanosecond regime.[20-22, 24] The short pulse width produces an ablation event

where the absorption of photons by the sample is primarily caused by electronic transitions, and the absorption event is over before the sample can begin to thermally heat up.[23]

The laser ablation event produces aerosol particles with a distribution of sizes ranging from <1 nm to >2.0 μm.[26] Aerosol particles or large agglomerates of smaller aerosol particles that are greater in size than 300-400 nm are not completely vaporized in the ICP.[26, 27] When these aerosol particles are not completely vaporized more volatile elements will vaporize at a higher degree than more refractory elements. This can cause a signal ratio that does not match the original stoichiometry of the sample. This phenomenon has been described as ICP-induced fractionation.

Work presented here will explore experimental and instrumental conditions that promote or inhibit ICP-induced fractionation. The first two of three papers (Chapters 2 and 3) will show a method of data acquisition and subsequent analysis using time-resolved studies to look at the contribution of ICP-fractionation alone. By looking at only the difference between the signal from an experiment and the original sample stoichiometry it would be extremely difficult to distinguish contributions from LA-induced fractionation and ICP-induced fractionation. The third paper (Chapter 4) will discuss experiments that study why elemental ratios vary as the sample gas flow rate of an ICP is altered. Experimental data suggests that changes in the sample gas flow rate affect the plasma temperature which can drastically affect elemental ratios detected by the mass spectrometer.

MOLECULAR ANALYSIS BY LASER/DESORPTION IONIZATION MASS SPECTROMETRY

Direct molecular analysis of samples using mass spectrometry can be achieved by several techniques including fast atom bombardment (FAB)[28], secondary ion mass spectrometry (SIMS)[29], laser desorption/ionization (LDI) techniques, and desorption electrospray ionization (DESI)[30]. Since the development of matrix-assisted laser desorption/ionization (MALDI) [31, 32], it has become a popular mass spectrometric technique for the analysis of biological molecules. MALDI has also shown to be a very good method for the molecular imaging of biological molecules *in situ*.[33, 34] Imaging mass spectrometry (IMS) has been used to analyze the spatial distribution of many biological molecules[35-37] (proteins, peptides, lipids, etc.) as well as bio-markers[38], and drug molecules and their metabolites[39, 40]

Analysis by MALDI is performed by co-crystallizing the analyte with a matrix. A laser is then focused onto the crystal. The matrix molecules absorb most of the photons and assist in the desorption and ionization of the analyte molecule. Ionization is often done through donation of a proton from the matrix molecule to the analyte molecule to create a singly charged $[M+H]^+$ ion, where M represents the analyte molecule.[41]

Although MALDI has become a premiere method for the analysis of biological molecules, it does have limitations to the spatial resolution it can perform for IMS and the types of molecules the technique can analyze well. Traditional MALDI matrices are organic acids such as 2, 5-dihidroxybenzoic acid (DHB) and α-cyano-4-hydroxycinnamic acid (CHCA).[42, 43] Organic acid matrices such as DHB and CHCA provide a means for the soft ionization of peptides and proteins, including very large species with m/z values in excess of

100,000. Because the MALDI process requires the co-crystallization of the analyte and matrix small hydrophobic molecules are difficult to analyze. In addition, since the matrix molecules are present at such high concentrations, typically at a ratio of 3000:1 to the analyte, there can be large background signal originating from the matrix molecule at m/z values <300. Traditional MALDI matrices yield crystals >10 μm, which is not desirable for high spatial resolution imaging. A variety of sample preparation techniques have been developed to combat this problem.[44-46] These methods work quite well, but the added complexity of the sample preparation often add an "art" component to making the method work well and reproducibly, especially for imaging

Limitations from using traditional organic acids as matrices for MALDI experiments have lead to areas of research finding alternative materials or methods to carry out LDI experiments. Desorption/ionization on porous silicon (DIOS) provides a means of sample ionization without any additional matrix.[47] Molten salts, or room temperature ionic liquids (RTIL), have been used to analyze a variety of biological molecules including proteins, peptides, and oligosaccharides.[48, 49] Given the recent influx of research in applications of nanoparticles, it is no surprise that nanoparticles have also been used in MALDI experiments.[50, 51]

Recently colloidal silver and colloidal graphite have been used as pseudo matrices for LDI experiments analyzing a variety of small molecules.[52-54] Since the use of these colloids does not require co-crystallization with the analyte, small hydrophobic molecules which would not co-crystallize with a MALDI matrix ionize much more efficiently. It has also been shown that colloidal graphite and colloidal silver cover the samples more homogeneously for

IMS experiments than traditional MALDI matrices.[52, 54] The use of these colloids have been used to spatially track metabolite changes in plant tissue after genetic modifications.[54, 55]

In addition to the use of MALDI for IMS, several secondary ion mass spectrometry (SIMS) methods have been used. Matrix-enhanced SIMS (ME-SIMS)[56], metal-assisted SIMS[57, 58], and more recently cluster SIMS[59] have been used to perform molecular imaging of a variety of molecules from small lipid molecules[59] to large macromolecules with masses in excess of 10,000 daltons[56]. SIMS techniques are able to provide much higher spatial resolution than MALDI.[60] Researchers are able to perform sub-cellular imaging with a spatial resolution of 200 nm.[61] MALDI is inherently limited by the laser spot size, and laser spot sizes of 100-250 μm are typically used. MALDI however has a distinct advantage of being a much softer ionization technique than the SIMS techniques. MALDI is able to produce intact molecular ions with high sensitivity. Due to the high kinetic energy of the secondary ions used in SIMS the majority of ions produced are fragmented ions from the analyte molecule. Most SIMS analysis produce no molecular ions. MALDI instruments are often cheaper and easier to maintain and use when compared to SIMS instruments. MALDI instruments allow the sample to be ionized at higher pressure than SIMS techniques which can allow samples to be changed much faster. For these reasons and others MALDI has become a much more popular technique for IMS experiments, even though it typically has worse spatial resolution. Pushing the limits of spatial resolution for LDI techniques is an important field of research, and work described here will show the ability of colloidal silver LDI to image at the individual cell level.

Since MALDI mass spectrometry was first demonstrated it has become a valuable method for the analysis of biological macromolecules. Even from these early stages of MALDI experiments, the sample was always placed in the mass spectrometer vacuum chamber for subsequent analysis. This proved to be the most efficient way to analyze the greatest number of ions produced in the MALDI process. However, requiring that the sample be placed in a chamber at low pressure extends the amount of time that it takes to analyze a sample; this most likely immediately caused some research to focus on the task of taking the MALDI experiment out of the vacuum and into atmospheric pressure. Using existing mass spectrometers set up for atmospheric sampling of ESI ionization source would also create multifunctional mass analyzers capable of using MALDI, ESI, atmospheric pressure chemical ionization (APCI), or atmospheric pressure photoionizaiton (APPI) sources.

Reasons behind the movement toward the use of MALDI at atmospheric pressure are not merely to provide higher throughput and easier sample preparation. Mass accuracy and resolution is highly dependent on the sample conditions in vacuum based MALDI techniques. Factors such as sample thickness, morphology, variations of sample or position, and laser power all affect these figures of merit for the mass analysis.[62] Also, extraction of ions from the ionization site in vacuum is mass dependent, and complicated extraction procedures are needed to correct this problem. AP-MALDI has provided conditions that would be much less sensitive to these concerns.[62]

In 2000 Laiko and coworkers at both University of California in San Francisco, CA and The John Hopkins University in Baltimore, MD successfully performed MALDI

experiments with sample at atmospheric pressure.[63, 64] Both experiments produced promising results for AP-MALDI. The UCSF group found that AP-MALDI was an extremely soft ionization source, analysis of a six-peptide mixture provided a mass spectrum with no fragmentation.[63] The JHU research group showed that AP-MALDI is able to achieve good detection limits, achieving detection limit values of $10 - 50$ fmol of several different proteins. The JHU research group also showed that experiments could be conducted both in positive and in negative modes. They were also able to demonstrate the capability of tandem mass spectrometry.[64]

The focus of the research described here will push the analytical limits of colloidal graphite and colloidal silver LDI-MS. An experiment showing increased spatial resolution of IMS using colloidal silver will be discussed (Chapter 6) which shows the ability to use colloidal Ag LDI-MS for imaging at the single cell level. Using these colloids for atmospheric pressure LDI-MS experiments will be discussed (Chapter 5) through experiments analyzing both standards and plant tissue. Using colloidal graphite and colloidal silver LDI-MS at atmospheric pressure would provide many of the advantages described above, and will also provide the means to perform IMS *in vivo*. When these experiments are completed at high vacuum or even intermediate pressures the plant tissue needs to be removed from the living plant, which can quickly affect the metabolite distribution. Placing the tissue under any type of lowered pressure also introduces the possibility that volatile metabolites can be removed from the tissue lowering their perceived concentration or making their presence undetectable altogether. Conducting IMS experiments at atmospheric pressure solves these problems.

REFERENCES

1.   R. H. Scott, V. A. Fassel, R. N. Kniseley and D. E. Nixon, *Analytical Chemistry*, 1974, **46**, 75-80.

2.   R. S. Houk, V. A. Fassel, G. D. Flesch, H. J. Svec, A. L. Gray and C. E. Taylor, *Analytical Chemistry*, 1980, **52**, 2283-2289.

3.   A. L. Gray, *Analyst*, 1985, **110**, 551 - 556.

4.   M. Tiepolo, Alberto Zanetti, Riccardo Vannucci, *Geostandards and Geoanalytical Research*, 2005, **29**, 211-224.

5.   D. Bleiner, M. Macrì, P. Gasser, V. Sautter and A. Maras, *Talanta*, 2006, **68**, 1623-1631.

6.   G. L. Foster and D. Vance, *Journal of Analytical Atomic Spectrometry*, 2006, **21**, 288-296.

7.   J. S. Becker, H. Sela, J. Dobrowolska, M. Zoriy and J. S. Becker, *International Journal of Mass Spectrometry*, 2008, **270**, 1-7.

8.   J. S. Becker, M. Zoriy J. Su Becker J. Dobrowolska M. Dehnhardt A. Matusch, *physica status solidi (c)*, 2007, **4**, 1775-1784.

9.   L. Arroyo, T. Trejos, P. R. Gardinali and J. R. Almirall, *Spectrochimica Acta Part B: Atomic Spectroscopy*, 2009, **64**, 16-25.

10.   Y.-L. Lee, C.-C. Chang and S.-J. Jiang, *Spectrochimica Acta Part B: Atomic Spectroscopy*, 2003, **58**, 523-530.

11.   C. Latkoczy, Y. Müller, P. Schmutz and D. Günther, *Applied Surface Science*, 2005, **252**, 127-132.

12. S. J. Bajic, D. B. Aeschliman, N. J. Saetveit, D. P. Baldwin, and R. S. Houk, *Journal of Forensic Sciences*, 2005, **50**, 1123-1127.

13. P.-H. Chi, F.-H. Ko, C.-T. Hsu, H.-L. Chen, C.-K. Yang, Y.-C. Sun and M.-H. Yang, *Journal of Analytical Atomic Spectrometry*, 2002, **17**, 358-365.

14. H. Longerich, D. Günther and S. Jackson, *Fresenius' Journal of Analytical Chemistry*, 1996, **355**, 538-542.

15. M. Guillong, I. Horn and D. Gunther, *Journal of Analytical Atomic Spectrometry*, 2003, **18**, 1224-1230.

16. R. E. Russo, X. L. Mao, O. V. Borisov and H. Liu, *Journal of Analytical Atomic Spectrometry*, 2000, **15**, 1115-1120.

17. D. Gunther, and C. A. Heinrich, *Journal of Analytical Atomic Spectrometry*, 1999, **14**, 1369 - 1374.

18. I. Horn and D. Günther, *Applied Surface Science*, 2003, **207**, 144-157.

19. D. C. Perdian, S. J. Bajic, D. P. Baldwin and R. S. Houk, *Journal of Analytical Atomic Spectrometry*, 2008, **23**, 336-341.

20. D. C. Perdian, S. J. Bajic, D. P. Baldwin and R. S. Houk, *Journal of Analytical Atomic Spectrometry*, 2008, **23**, 325-335.

21. N. J. Saetveit, S. J. Bajic, D. P. Baldwin and R. S. Houk, *Journal of Analytical Atomic Spectrometry*, 2008, **23**, 54-61.

22. J. Koch and D. Günther, *Analytical and Bioanalytical Chemistry*, 2007, **387**, 149-153.

23. R. E. Russo, X. Mao, J. J. Gonzalez and S. S. Mao, *Journal of Analytical Atomic Spectrometry*, 2002, **17**, 1072-1075.

24. C. Liu, X. L. Mao, S. S. Mao, X. Zeng, R. Greif and R. E. Russo, *Analytical Chemistry*, 2004, **76**, 379-383.

25. F. Poitrasson, X. Mao, S. S. Mao, R. Freydier and R. E. Russo, *Analytical Chemistry*, 2003, **75**, 6184-6190.

26. B. Hattendorf, C. Latkoczy and D. Guenther, *Analytical Chemistry*, 2003, **75**, 341 A-347 A.

27. D. B. Aeschliman, S. J. Bajic, D. P. Baldwin and R. S. Houk, *Journal of Analytical Atomic Spectrometry*, 2003, **18**, 1008-1014.

28. M. Barber, R. S. Bordoli, R. D. Sedgwick and A. N. Tyler, *Journal of the Chemical Society, Chemical Communications*, 1981.

29. L. Van Vaeck, A. Adriaens, R. Gijbels, *Mass Spectrometry Reviews*, 1999, **18**, 1-47.

30. Z. Takats, J. M. Wiseman, B. Gologan and R. G. Cooks, *Science*, 2004, **306**, 471-473.

31. M. Karas, D. Bachmann and F. Hillenkamp, *Analytical Chemistry*, 1985, **57**, 2935-2939.

32. H. W. Koichi Tanaka, Yutaka Ido Satoshi, Akita Yoshikazu, Yoshida Tamio, Yoshida T. Matsuo, *Rapid Communications in Mass Spectrometry*, 1988, **2**, 151-153.

33. D. S. Cornett, M. L. Reyzer, P. Chaurand and R. M. Caprioli, *Nature Methods*, 2007, **4**, 828-833.

34. W. Hardesty and R. Caprioli, *Analytical and Bioanalytical Chemistry*, 2008, **391**, 899-903.

35. A. C. Crecelius, D. S. Cornett, R. M. Caprioli, B. Williams, B. M. Dawant and B. Bodenheimer, *Journal of the American Society for Mass Spectrometry*, 2005, **16**, 1093-1099.

36. K. E. Burnum, S. L. Frappier and R. M. Caprioli, *Annual Review of Analytical Chemistry*, 2008, **1**, 689-705.

37. S. N. Jackson, M. Ugarov, T. Egan, J. D. Post, D. Langlais, J. A. Schultz, A. S. Woods, *Journal of Mass Spectrometry*, 2007, **42**, 1093-1098.

38. P. H. Pevsner, J. Melamed, T. Remsen, A. Kogos, F. Francois, P. Kessler, A. Stern and S. Anand, *Biomarkers in Medicine*, 2009, **3**, 55-69.

39. D. M. Drexler, T. J. Garrett, J. L. Cantone, R. W. Diters, J. G. Mitroka, M. C. Prieto Conaway, S. P. Adams, R. A. Yost and M. Sanders, *Journal of Pharmacological and Toxicological Methods*, 2007, **55**, 279-288.

40. D. S. Cornett, S. L. Frappier and R. M. Caprioli, *Analytical Chemistry*, 2008, **80**, 5648-5653.

41. M. Karas, M. Glückmann, and Jürgen Schäfer, *Journal of Mass Spectrometry*, 2000, **35**, 1-12.

42. R. C. Beavis, T. Chaudhary B. T. Chait, *Organic Mass Spectrometry*, 1992, **27**, 156-158.

43. J. Kampmeier, K. Dreisewerd, M. Schürenberg and K. Strupat, *International Journal of Mass Spectrometry and Ion Processes*, 1997, **169-170**, 31-41.

44. P. Önnerfjord, S. Ekström, J. Bergquist, J. Nilsson, T. Laurell, and G. Marko-Varga, *Rapid Communications in Mass Spectrometry*, 1999, **13**, 315-322.

45. R. M. A. Heeren, B. Kükrer-Kaletas, I. M. Taban, L. MacAleese and L. A. McDonnell, *Applied Surface Science*, 2008, **255**, 1289-1297.

46. T. Tu, A. D. Sauter Jr, A. D. Sauter 3rd and M. L. Gross, *Journal of the American Society for Mass Spectrometry*, 2008, **19**, 1086-1090.

47. J. Wei, J. M. Buriak and G. Siuzdak, *Nature*, 1999, **399**, 243-246.

48. M. Mank, B. Stahl and G. Boehm, *Analytical Chemistry*, 2004, **76**, 2938-2950.

49. D. W. Armstrong, L.-K. Zhang, L. He and M. L. Gross, *Analytical Chemistry*, 2001, **73**, 3679-3686.

50. A. Dass, A. Stevenson, G. R. Dubay, J. B. Tracy and R. W. Murray, *Journal of the American Chemical Society*, 2008, **130**, 5940-5946.

51. M. T. Spencer, H. Furutani, S. J. Oldenburg, T. K. Darlington and K. A. Prather, *The Journal of Physical Chemistry C*, 2008, **112**, 4083-4090.

52. S. Cha and E. S. Yeung, *Analytical Chemistry*, 2007, **79**, 2373-2385.

53. H. Zhang, S. Cha and E. S. Yeung, *Analytical Chemistry*, 2007, **79**, 6575-6584.

54. S. Cha, Z. Song, B. J. Nikolau and E. S. Yeung, *Analytical Chemistry*, 2009, **81**, 2991-3000.

55. S. Cha, H. Zhang, H. I. Ilarslan, E. S. Wurtele, L. Brachova, B. J. Nikolau, and E. S. Yeung, *The Plant Journal*, 2008, **55**, 348-360.

56. K. J. Wu and R. W. Odom, *Analytical Chemistry*, 1996, **68**, 873-882.

57. A. Delcorte, N. Medard and P. Bertrand, *Analytical Chemistry*, 2002, **74**, 4955-4968.

58. A. Delcorte, J. Bour, F. Aubriet, J. F. Muller and P. Bertrand, *Analytical Chemistry*, 2003, **75**, 6875-6885.

59. P. Sjovall, J. Lausmaa and B. Johansson, *Analytical Chemistry*, 2004, **76**, 4271-4278.

60. R. M. A. Heeren, L. A. McDonnell, E. Amstalden, S. L. Luxembourg, A. F. M. Altelaar and S. R. Piersma, *Applied Surface Science*, 2006, **252**, 6827-6835.

61. S. G. Ostrowski, M. E. Kurczy, T. P. Roddy, N. Winograd and A. G. Ewing, *Analytical Chemistry*, 2007, **79**, 3554-3560.

62. S. C. Moyer and R. J. Cotter, *Analytical Chemistry*, 2002, **74**, 468 A-476 A.

63. V. V. Laiko, S. C. Moyer and R. J. Cotter, *Analytical Chemistry*, 2000, **72**, 5239-5243.

64. V. V. Laiko, M. A. Baldwin and A. L. Burlingame, *Analytical Chemistry*, 2000, **72**, 652-657.

CHAPTER 2. TIME-RESOLVED STUDIES OF PARTICLE EFFECTS IN LASER ABLATION INDUCTIVELY COUPLED PLASMA-MASS SPECTROMETRY: I. INVESTIGATION OF NANOSECOND AND FEMTOSECOND PULSE WIDTH LASERS AND DEVICES FOR PARTICLE SIZE SELECTION

D. C. Perdian, Stanley J. Bajic, David P. Baldwin, and R. S. Houk*

ABSTRACT

Transient signal responses for ablated samples as a function of particle size and laser parameters are characterized.   Data are acquired with time resolution of 5, 6, or 7 ms per data point. Large positive spikes in signal are observed and increase in both amplitude and frequency with increasing particle size. Particle sizes are selected using a differential mobility analyzer. Spikes in signal also increase with decreasing laser rastering rates. Comparison of lasers with pulse widths of 370 fs and 5 ns shows that shortening the pulse width significantly reduces the frequency and amplitude of positive spikes in signal. These large positive spikes are attributed to the vaporization, atomization, and ionization of individual large intact particles, which are considered to be a major cause of fractionation in laser ablation ICP-MS.

*Corresponding Author

INTRODUCTION

Laser ablation inductively coupled plasma mass spectrometry (LA-ICP-MS) has become a common method for trace and ultra trace elemental analysis of solid samples. Identification and determination of approximate concentration is straightforward. More accurate quantification, however, is hindered by fractionation. These effects can occur during ablation, aerosol transport, and/or in the plasma. ICP-induced fractionation has been attributed to preferential vaporization, atomization, and ionization of different elements from LA aerosols, particularly those with too many large particles.[1]

The absence of matrix-matched standards for a wide variety of samples has led to research in reducing fractionation effects for LA-ICP-MS. Successful experiments have been completed using solution based calibration methods for quantification with LA-ICP-MS.[2, 3] However, both solution-calibration methods fail to account for non-stoichiometric signal arising from fractionation effects. Fundamental research with the goal of exploring experimental conditions that reduce or eliminate the error in quantification caused by fractionation effects will allow LA-ICP-MS to become a routine analytical technique for quantification of elements in solid samples, much like solution based methods are now.

High speed digital photographic studies of the fate of aerosol particles in the ICP created by LA were conducted by Aeschliman et al. Many particles are obviously not completely vaporized in the plasma.[4] In fact, it was discovered that particles remain intact through the initial radiation zone as well as through the normal analytical zone,[5] far downstream from the usual sampling position for ICP-MS. A large excess of atomic ions surrounds the large particles in the plasma, which can be seen from the "cloud" of local

atomic ion emission that is more intense than surrounding areas of the plasma. This excess of atomic ions can lead to large positive spikes in signal. The presence of a large positive spike in signal corresponds to a large aerosol particle in the plasma. Volatile elements may preferentially vaporize from these aerosol particles, causing an ion signal ratio that is not representative of the original sample, which is the definition of ICP-induced fractionation. There are also other problems that can arise from these large particles, such as clogging of the sampling cone. This deposition can cause a higher atomic ion background, which adversely affects the detection limits of the analytical process.

The present paper shows that large positive spikes in signal rising above the steady state signal are more common and larger in magnitude in laser-ablation experiments than solution-nebulization experiments, as more large particles are being introduced into the plasma during laser ablation. Such large positive spikes in signal are often seen during mass scans during LA-ICP-MS.   The large positive spike in signal occurs because of the excess of M^+ ions surrounding the large particles that make it to the plasma from the laser ablation. This brief burst of M^+ ions is only seen on one of many scans, when the mass analyzer happened to be set to transmit the m/z value corresponding to M^+.

Previous studies on the effect of particle size distribution on the ICP-MS signal have shown it has a profound effect on signal.[6,7] Other studies show that small (~ 10 nm) aerosol particles, created by the laser ablation event, agglomerate and reach μm sizes when they enter the ICP.[8]

Numerous time-resolved studies have been conducted using solutions and nebulizers to study the fate of individual sample droplets in the plasma. Fast data acquisition methods

have been used to determine calcium content in individual biological cells in real time by ICP atomic emission spectrometry.[9] Olesik used data acquisition on a time scale of ~20 µs to show that, at flow rates lower than what would produce an optimum ICP-MS signal at a given sampling position, many large positive spikes in signal occurred, as many as 2,620 spikes per second.[10,11] This phenomenon was attributed to the vaporization of individual desolvated particles, when combined with previous information from fluorescence measurements.[11] Time-resolved experiments with various laser and experimental parameters for LA-ICP-MS in the present work will shine light on the causes of this phenomenon, and possibly identify ways to reduce the frequency and amplitude of these large positive spikes, i.e., remove large particles or prevent their formation.

The use of fast data acquisition to investigate droplet effects with ICP-MS alone has been demonstrated recently on a magnetic sector instrument.[12] A solution containing bacteria was nebulized into the plasma, which enabled the characterization of the temporal behavior of intact cells in the ICP. The behavior of bacteria in the plasma was studied with time resolution of ~4 ms. Short-lived U^+ signal spikes were observed, which corresponded to uranium from individual bacteria grown in an uranium enriched culture medium. The time scale achieved on the magnetic sector instrument is slower than the typical transit time of an individual particle through the plasma (~ 1 ms), however it is fast enough to see signals from individual particles if they are introduced infrequently enough so that their signal spikes can be discerned from the steady-state level from other particles in the plasma.

Many experimental factors affect the signal during the laser ablation process, such as laser parameters, transport gas, plasma conditions, and the composition of the aerosol.

Effects of laser parameters such as wavelength, pulse duration, and energy have been studied previously.[13-16] It has been reported that shorter wavelengths reduce fractionation effects.[17] Most samples absorb better at shorter wavelengths. This increased absorption creates laser-ablation plumes and subsequent aerosol by the direct absorption of the laser radiation, rather than an aerosol generated from the transfer of the laser energy by thermal processes and melting of the sample.[13]

The effects of laser pulse width on ICP-MS performance have been studied with some vigor recently.[18-22] Reducing the laser pulse width into the femtosecond regime (<1 ps) can dramatically reduce ablation related fractionation effects.[18] The ablation process in the femtosecond regime is drastically different from that for a nanosecond laser. The laser-ablation process for lasers with femtosecond pulse widths is much less dependent on thermal processes. It has been reported that no melting is observed with lasers that have pulse lengths less than 1 ps, which leads to more stoichiometric signals as the thermal properties of the elements do not affect their removal during the laser-ablation process.[20]

Kozlov et al. used an orthogonal acceleration time-of-flight (TOF) mass spectrometer to measure isotope ratios on time scales of 100 ms.[23] The use of a TOF mass spectrometer allowed the researchers to measure isotopic ratios with good precision during laser ablation ICP-MS experiments because of its ability to measure multiple isotopes in very rapid succession. Kozlov et al. could see fast variations in the signal and sudden enrichments of some elements during the analysis of an Australian coin. They attributed these variations to the presence of large particles in the plasma.[23]

Coiled tubes have been used to remove large particles from the laser ablation aerosol.[24] These devices function as low-pass filters and successfully remove a large portion of particles above ~200 nm in size. The resulting filtered aerosols are more nearly stoichiometric, and the resulting ICP-MS signals change less extensively with time, two symptoms of fractionation.[24]

This is the first of two articles exploring time-resolved studies of particle effects in LA-ICP-MS experiments. The second article will discuss the effect of experimental parameters, specifically sample composition, transport gas, and the use of a binding agent in preparing samples. The second article will also discuss the behavior of MO^+ ions.

EXPERIMENTAL SECTION

Samples - National Institute of Standards and Technology (NIST) standard reference materials (610 and 612 glass, C1102 brass, and 1648 urban dust, Gaithersburg, MD, USA) were used. The NIST 1648 dust pellet was made by manually pressing approximately 0.4 g of NIST 1648 into an aluminum planchet without a binder.

Magnetic Sector ICP-MS Device – Except where stated otherwise, the experiments were done with a magnetic sector instrument (Element 1, Thermo Finnigan, Bremen, Germany). In hot plasma mode, most instruments are usually tuned to maximize signal sensitivity. In the present study, this procedure yields too many signal spikes to examine them in isolation. Therefore, the aerosol gas flow rate was set between 1.1 and 1.25 L min^{-1}, about 0.1 L/min lower than that which maximizes M^+ signal. This criterion maintained reasonable stability

during laser ablation while retaining adequate sensitivity. Depending on the sample, the sensitivity obtained by this procedure was ~ 50 to 75 % of the maximum. Auxiliary gas flow rates and outer gas-flow rates were typically set between 0.80 to 0.95 L min^{-1} and 14 to 15 L min^{-1}, respectively.

The instrument acquired data in low resolution mode (m/Δm ~ 300) for all experiments. Parameters for data acquisition are listed in Table 1. The result of these instrument settings is that a data point is collected at 6 ms intervals, although the signal is integrated for approximately 1.5 ms. To achieve the fastest time resolution possible, signal can be measured at only one m/z value during a single data acquisition event with the mass spectrometer.

TOF-ICP-MS Device. A few experiments (Figures 10 and 11) were done with an orthogonal acceleration time of flight instrument (Optimass 8000 ICP-TOF-MS, GBC Scientific Equipment, Dandenong, VIC Australia) for very rapid measurement of many isotopes. The ICP-TOF-MS was able to achieve faster time resolution; values of 1 ms per data point were achieved. Data were acquired with time resolution between 5 or 6 ms per data point, because in this time regime the signal was more stable and sensitive. With the TOF-MS, multiple isotopes could be measured in a single experiment with the time resolution desired. Optimization of signal sensitivity and stability during laser ablation was performed by tuning the sample, auxiliary, and outer gas flow rates, which were 1.18, 0.875, and 10.0 L min^{-1} respectively.   These gas flow rates also resulted in signal levels of 50-75% of maximum signal intensity. Voltage settings for the TOF mass spectrometer are listed in

Table 2. The detector was operated in analog mode so that relative peak intensities could be measured during each mass scan. Mass spectra are measured at a repetition rate of 30 kHz. Data taken with a time resolution of 5 ms is the sum of 150 spectra, 6 ms is the sum of 180 spectra.

Nanosecond Laser - A Q-switched Nd:YAG laser (LSX 500, energy 9 mJ, pulse width ~ 5 ns, CETAC Technologies, Omaha, NE, USA), quadrupled to a wavelength of 266 nm, was used for the majority of the experiments. The LSX 500 can be operated at varying laser spot sizes by controlling the diameter of an internal aperture. The laser was set to a repetition rate of 20 Hz with a spot size of 50 μm. The ablation cell rests on a translation stage, which controls the ablation location, raster rate, and raster pattern.   The laser-raster rate was set to 100 μm/s, except where the effect of laser-raster rate was studied.

Femtosecond Laser - To compare the effect of pulse width, a Yb-doped fiber chirped pulse amplification (FCPA) laser was also used (wavelength 1045 nm, repetition rate of 100 kHz, pulse energy 4 μJ, pulse width 370 fs, μJewel FCPA, IMRA Inc, Ann Arbor, MI, USA). Operation of the FCPA laser has been discussed elsewhere.[25]

LA Cells – Both lasers used cylindrical ablation cells with the gas entering the ablation region at the bottom and exiting at the top. For the ns laser, the standard ablation cell from CETAC was used: 25 mm high x 60 mm diam., total volume 70 cm^3, inlet 2 mm ID. For the fs laser, a homemade, double-walled cell was used: 45 mm high x 50 mm diam., total

volume 90 cm^3, inlet 4 mm ID. The same Tygon tubing (4 mm ID x ~ 1 m long) was used to conduct the aerosol to the ICP in both cases. The same brass sample was ablated with the ns laser using either cell; the signal levels and noise behavior were similar. Thus, the cell geometry does not greatly affect the signal or noise behavior described below.

Particle-Size Selection - A differential mobility analyzer (DMA) was employed (TSI Model 3080L DMA, TSI Inc, Shoreview, MN, USA) to separated particles based on electrical mobility, as described in detail elsewhere.[26] Briefly, the polydisperse aerosol created from the laser-ablation process is sent through a bipolar discharger, which imparts a neutral equilibrium distribution of positive, negative, and neutral charges on the aerosol particles. The aerosol then passes through a differential mobility analyzer, which only allows particles with a specified electrical mobility to pass out to the plasma.

The DMA is said to transmit size values from 0.001 to 1 μm, so that the user can select the size of particle that passes through as a monodisperse aerosol. Under typical conditions the particle-size bandpass window is said to be 5% at small sizes and increases to 10% at larger particle sizes.

It must be noted that the actual size of the particles may be somewhat different from the nominal size determined from the DMA settings. Differences in composition, shape and/or morphology between the particles used for size calibration and the particles generated from the samples may cause this behavior. The size calibration supplied with the device assumes air or nitrogen is the carrier gas, not the argon used in the present work. In particular, loose agglomerates of fine particles, like those seen by Günther et al., may be

transmitted at different settings than a single particle of the equivalent mass or diameter.[27]

Also, the DMA arcs occasionally, especially when argon is the carrier gas and it is set to

transmit the largest particles, i.e., when the applied voltage is highest. Arcing causes

unstable signals; such results were discarded. In our experience, the DMA did operate

reliably for long periods with argon as carrier gas.

Coiled metal tubes, like those produced by Guillong et al., were also used in several

experiments.[24] They consist of a 20 gauge stainless steel needle (tube dimensions 0.56 mm

ID x 15.3 cm long), either straight or bent in 1 to 5 complete revolutions. The diameter of

the coils was approximately 6 mm. One goal was to characterize the calibration function of

the DMA, so the LA particles passed through the coil first, then the DMA. The subsequent

M^+ signal was then measured with the ICP-MS device as a function of particle size selected

by the DMA. For the data shown below, these coils were used only where noted.

Histograms and Skew Values. The data were exported to Excel and plotted as histograms

with (individual signal)/ (average signal) as the horizontal axis. Skew values were calculated

using the corresponding statistical function in Excel.

RESULTS AND DISCUSSION

Solution Nebulization and Data Evaluation – As a point of reference, the signal of $^{69}Ga^+$

from a 1-ppb solution of Ga as a function of time using fast data acquisition is shown in Fig.

1a. The Ga$^+$ signal at this time resolution is quite noisy with much of the variance coming

just from counting statistics. The mean signal of this plot is 2.04 x 10^5 c/s, with a standard

deviation of $\pm1.24 \times 10^4$. The standard deviation expected from counting statistics is $n^{1/2}$, where n is the number of counts measured. The signal variation caused by counting statistics is calculated in the following manner; 2.04×10^5 c/s x 1.5×10^{-3} s = 300 counts, the absolute standard deviation is $300^{1/2}$ = 17, for a count rate of 17 counts/1.5×10^{-3}s = 1.13×10^4 counts/s. Although there are some spikes, both positive and negative in direction, that extend beyond this range, the bulk of the noise is caused just by counting statistics. The other cause(s) of signal variance could come from many areas and do not warrant further discussion, as the spikes in signal that will be investigated are much larger in intensity and are only positive in direction, i.e., the spikes only increase the signal.[12]

To examine the effect of positive spikes in signal, a histogram plot (Figure 1b) is created to display the distribution of the ratio of individual signal in each data bin to average signal. The numerical value of skew of the histogram is also shown. Measurement of the skew for the signal histograms shows how much the steady state signal is affected by positive spikes in signal. As the amplitude and frequency of positive spikes increases, the skew of the histogram increases. The skew of a symmetrical distribution of signal would be zero. A negative skew value indicates that the signal has a large portion of negative spikes in signal (signal values much lower than the mean signal value). We suggest that, as the skew of the histogram increases, there is a larger fraction of aerosol particles that are not completely vaporized and atomized, and thus have a greater possibility of promoting fractionation effects in the ICP.

Particle Diameter – ICP-induced fractionation is believed to be related largely to particle size.[1] Thus, the effect of particle size on signal is of great interest. The DMA electrostatic classifier was used to select particles in a specific size range from the LA aerosol to be transported to the plasma. Nominal particle sizes from 100 to 1000 nm, in 100 nm increments, were studied. As noted above, the actual sizes transmitted may differ somewhat from those cited.

Figure 2 shows four plots of $^{238}U^+$ signal as a function of time for 100, 200, 500, and 1000 nm particles, while ablating NIST 610 glass in raster mode. As the particle size increases the amplitude and frequency of the positive spikes increase. The signal from 100 nm particles is noisy. However, the noise again is mainly just counting statistics (mean signal: 4.06×10^3 c/s $\pm 2.00 \times 10^3$ c/s; counting statistics noise: $\pm 1.63 \times 10^3$ c/s). As the particle size increases to 200 nm the steady state signal rises almost 10X, and a few positive spikes appear. The spikes become more frequent and larger for 500 nm particles. Finally when looking at the signal produced from 1000 nm particles, the frequency and amplitude of positive spikes is quite significant. The vertical axis maximum is increased from Fig. 2a – d because of the increase in signal caused mainly by the size of the spikes. This trend stretches across the particle sizes examined; only the plots for 100, 200, 500, and 1000 nm particle sizes are shown for the sake of brevity. This phenomenon was seen with all atomic ions studied (Li, Si, Ti, Ni, Cu, Zn, Ga, Sr, Y, Ce, Cd, Sn, Tl, Pb, Th, and U).

We attribute the large spikes in signal to the local excess of ions surrounding the vaporizing/atomizing particles in the plasma.[3] The influence of a large particle on signal is linked to size, position and trajectory (Figure 3). If an aerosol particle is sufficiently small

(Figure 3a), typically considered to be 150 nm or less (although this size limit is somewhat dependent on instrument and operating conditions),[28] it will be efficiently vaporized and atomized and the ions created will contribute to the steady state signal. Composition and thermal properties of the particle may also affect this 150 nm limit.

Particles larger than 150 nm are less extensively vaporized and atomized in the ICP.[28] A pair of elements of different volatility from these bigger particles may generate signals whose ratio is different from the stoichiometry of the original sample.[29] The exact influence of such particles on signal also depends on their position in the ICP. Such effects are exacerbated by the fact that the ICP-MS signal basically reflects the composition of the plasma region one skimmer diameter wide just in front of the sampler.[30] If the particle is displaced off the axis through the sampler and skimmer (Figure 3b), its M^+ vapor cloud is also off-axis, and it mainly contributes to the steady state signal. If the large particle is on-axis and is still intact as it approaches the sampler (Figure 3c), the excess of M^+ ions surrounding the intact particle generates a large positive increase in M^+ signal, but only for a brief time, comparable to the flight time of the particle through the ICP. Such a particle causes the large signal spikes seen in previous figures.

Histograms of the individual signal/average signal intensity for 200, 300, 400, and 800 nm particle sizes are shown (Figure 4) for $^{238}U^+$ from NIST 610 glass. The skew values of the distributions for both 200-nm and 300-nm size particles are almost the same and are significantly lower than the skew for both 400-nm and 800-nm size particles. A plot of skew as a function of particle size (Figure 5) for $^{238}U^+$ in NIST 612, $^{238}U^+$ in NIST 610, and $^{118}Sn^+$ in NIST 610 shows that, for a given sample type, the skew values for 100, 200, and 300-nm

sizes are similar and low. This behavior is expected, as the plasma completely vaporizes and atomizes particles below the size of 150-nm. For particles far above this 150-nm threshold, vaporization and atomization in the plasma are less complete.[28] The skew value increases sharply at a DMA setting of 400 nm and trends upward as the particle size increases further.

Effect of Coiled Particle Separation Devices – These coiled metal tubes select particles below a certain cutoff value for transmission to the ICP. The more coils, the smaller the cutoff diameter.[21, 27] Thus, use of these coiled metal tubes should decrease the occurrence of signal spikes produced from large particles. A straight metal tube is also evaluated as a control.

In one experiment, a coil is used to select particles, followed by the DMA and ICP-MS. The subsequent M^+ signal is used to evaluate whether the DMA transmits particles as advertised. Figure 6 shows signal as a function of DMA setting for particle separation devices of the same overall length but different numbers of coils. The signal for Cu^+ from NIST C1102 brass was measured while the DMA was set to transmit particles of various sizes from 50 ± 3 through 1000 ± 100 nm.

At low DMA settings (<400 nm) the signal is actually moderately higher when the particles are first filtered with a coil or tube, compared to the signal when a coiled particle separation device is not used. This increase in signal is a result of several phenomena. There are different fates of the large species (i.e., agglomerates and large solid particles) in the separation device, which could possibly cause the increase in signal. The large species that collide with the interior of the device can either lose momentum and eventually fall out of the

transport gas stream, and remain in the device. Some large species, particularly agglomerates, can break up into particles of smaller diameter upon impact with the interior of the separation device. These newly created, fine particles would not be produced without a particle separation device and could also cause the increase in signal.

With a straight tube, there is some drop in signal for particle sizes above 500 nm compared to the signal when there is no tube or coils. This drop in signal for large particle sizes is likely caused by the change in inner diameter of the transport material. The transport tubing has an inner diameter of 0.32 cm, whereas the inner diameter of the stainless steel needle is 0.056 cm, greater than 5X smaller. This thin needle causes a drop in transport efficiency, particularly for larger particles.

Signal, histogram plots and skew values were measured for $^{238}U^+$ from a NIST 1648 Urban Dust pellet with the LA aerosol filtered only by one of the coil devices, not the DMA. As shown in Table 3, the coils drastically reduce the skew of the signal distribution from 24.3 with a straight tube to 5.09 with two turns to 3.99 with four turns. For this dust pellet, the coils also greatly attenuate the steady state signal from ~3 x 10^5 counts/s with no tube to ~ 1 x 10^5 counts/s for a particle separation device with 5 turns (data not shown). This signal loss could be a problem if sensitivity is considered more important than signal stability for a specific analysis. The loss of steady state signal may also be the reason why the skew does not continually decrease as the number of coils increases. It must be noted that the large signal losses using particle separation devices are more pronounced when ablating the dust sample rather than the glass or brass samples. This is a function of the sample morphology. The dust pellet is already an agglomerate and ablates largely by being shattered by the laser.

This is expected to produce more particles with a large diameter. These large agglomerates would not be expected to have the same mechanical strength as the large particles produced from the ablation of a glass or metal sample.

In general, these results support the previous studies by Günther and coworkers. In particular, the M^+ signal maximizes when the DMA is set to transmit particles in the range 200 to 300 nm, particularly when more coils are used (Figure 6). As noted above, the skew of the distributions increases markedly when the DMA is set to transmit 400 nm particles, which is more or less the size range where large-particle effects would be expected. These observations argue that the DMA does indeed select particles based on size, and that the size calibration is at least approximately correct. However, we do see larger sacrifices of signal using particle separation devices than the previous workers. [21, 27]

Laser Rastering Rate - To study the effect of laser rastering rate, NIST 610 glass was ablated while moving the laser spot at 25, 50, 75, and 100 μm/sec. Figure 7 shows the histograms for $^{118}Sn^+$ signal as a function of time for 800 nm particles. The skew value decreases as the raster rate increases up to 75 μm/s; the skew value is about the same between 75 and 100 μm/s. Similar effects were seen for other size settings of the DMA, or when the DMA was not used.

This observation can be attributed to the following effect. The laser both removes material and heats the material left behind adjacent to the crater. In raster mode, the laser beam continuously moves onto previously heated areas of the sample, which may ablate differently than pristine zones. These areas near an existing crater also have material

deposited from previous laser shots. Slower laser rastering rates result in more overlap of adjacent laser spots, more extensive reheating and/or re-ablation, and more contribution to the signal from large particles.

It should also be noted that there seem to be two distinct groups of skew values in Figure 7. The two lower rastering rates have similar skew values. The two higher rastering rates also behave similarly. A significant decrease in both frequency and amplitude of the positive spikes in signal and therefore skew, occurs from 50 to 75 μm/s, which was somewhat surprising, and its cause is not obvious.

Single Laser Shots – A plot of signal versus time for $^{238}U^+$ in which the LSX 500 fired just one laser shot at the NIST 610 sample is displayed in Fig. 8. Here the coils or DMA were not employed. Similar plots are obtained for other elements; only one is shown for brevity.

The plot in Fig. 8 shows the typical signal shape for single laser shots, a rapid increase in signal followed by slow decay back to the background level. However, using fast data acquisition, large spikes can be seen throughout the evolution of each signal pulse, even in the short time frame between the onset and the apex of the signal. There are many such spikes during the slow signal decay after the apex. Some of these latter spikes have greater net count rates than the initial apex, and occur several seconds after the laser pulse.   This shows that ICP-induced fractionation can occur throughout the signal evolution of a single laser shot experiment.

Laser Pulse Width - Signal versus time plots for laser ablation with the 370-fs pulse NIR laser are compared to those obtained with the 5-ns UV laser. As noted in the Experimental section, the two lasers are compared with each one operating under conditions close to what would be used analytically. Most parameters such as energy, repetition rate, and wavelength could not be made similar between the two lasers.

The plots for both $^{63}Cu^+$ and $^{66}Zn^+$ in NIST C1102 brass standard reference material are shown in Fig. 9 for both lasers. The steady state signal levels are similar for both lasers; indeed, they were operated to make them so. However, there are many fewer large spikes with the fs laser. The Cu/Zn signal ratios for both lasers are higher than values expected from the known sample composition and isotope abundance and the expected ionization efficiencies of Cu and Zn in the ICP. The Cu/Zn signal ratios are 13.6 for the NIR fs laser, and 23.8 for the UV ns laser, whereas the Cu/Zn percent by weight ratio for NIST C1102 is 11.6. Previous studies have shown that even with an excess of Cu in the sample an excess of Zn is measured in the plasma.[31,32] However, the Cu/Zn signal ratio for the NIR fs laser is closer to that in the samples, as seen previously,[33,34] which is good news for the fs laser.

In our experiment, the aerosol gas flow rate is less than that which maximizes the signal. This optimization criterion accounts for much of the disparity between the "high" Cu/Zn signal ratios reported here and the lower ratios measured by other labs.[31,32] We have previously reported Cu/Zn ratios from brass with the ns laser that agree better with those obtained elsewhere.[33] Recent measurements with the ns laser show that the Cu/Zn signal ratio goes from 22.3 at 1.00 L min^{-1} (i.e., an aerosol gas flow rate similar to that used in this paper)

to 13.4 at 1.20 L min^{-1}. The most important result here, however, is the observation that using the fs laser significantly reduces the presence of large signal spikes.

At laser pulse widths in the fs regime, the ablation process occurs due to the direct absorption of the laser energy by the electrons in the sample. The atoms do not move much during the very short laser pulse, so thermal effects such as melting or thermally-induced changes in composition are reduced or eliminated.[35] The decrease in melting with the fs laser causes the distribution of particle sizes to be shifted toward smaller diameters. This reduces the appearance of large spikes in signal, which subsequently could lead to a decrease in ICP-induced fractionation effects. These data support previous findings by other groups performing laser ablation with fs lasers.[22,34]

Although the two lasers compared have different specifications in addition to pulse width (i.e., wavelength, power, repetition rate), previous research suggests that this phenomenon is mainly caused by the pulse length. High repetition rate ablation has been studied before with ns lasers, and precision and sensitivity did improve. However, this improvement is not as significant as that seen using a laser with a much shorter pulse width.[36] As for the wavelength, it has been known for some time that fractionation effects are reduced as the wavelength is decreased for ns lasers.[17] The longer wavelength and lower pulse energy of the NIR laser would both be expected to cause more fractionation effects.[37,38] The opposite of this expectation is observed, providing more evidence that the pulse width is the predominant feature in causing the significant reduction in spikes in signal observed in these experiments.

Time-of-Flight Measurements – With the magnetic sector device, neither the magnetic field nor the accelerating voltage can be changed fast enough to measure different elements during the passage of a single particle through the plasma. The use of an ICP-TOF-MS device enables the fast measurement of many isotopes from a given particle during LA experiments. A plot of signal as a function of time for $^{117}Sn^+$, $^{118}Sn^+$, $^{119}Sn^+$ and $^{121}Sb^+$ isotopes (Figure 10) shows two large positive spikes in signal at 2.763 s and 3.003 s. Both spikes are observed for the Sn isotopes as well as the Sb isotope. The isotope ratios for the Sn isotopes measured during the spikes (Table 4) are similar to the expected natural isotope ratios for Sn. This simultaneous occurrence of large signal spikes is also seen for $^{117}Sn^+$, $^{118}Sn^+$, $^{119}Sn^+$, $^{206}Pb^+$, $^{207}Pb^+$, $^{208}Pb^+$, and $^{209}Bi^+$ isotopes at 2.972 and particularly 3.788 s (Figure 12). The Sn and Pb isotope ratios are approximately correct, indicating that the spikes actually come from the various elements in the sample rather than from some unknown signal artifact.

These results show that the spikes in signal occur for many isotopes and elements at essentially the same time, most likely corresponding to atomization from an intact large particle surrounded by a large excess of atomic ions from many elements in the sample. It is interesting to note that the magnitude of signal spikes does vary from element to element for a single large signal spike event. For instance, the spike at 2.763s (Fig. 10) has signal increase of twenty times for Sn signal compared to average baseline signal for the immediate area surrounding the spike. However, the signal increase for Sb at the same time is only 11X. A similar difference is seen at 3.003 s, the Sn signal increases 10X greater than the surrounding baseline average, whereas the Sb signal only increases 5X. Differences in signal spike magnitudes are even more apparent in Fig. 11. The signal spike/average signal ratio is

5X, 6X, and 5X for Sn, Pb, and Bi respectively for the spike at 2.972 s. The signal spike/average signal ratios at 3.788 s are 70X, 22X, and 5X for Sn, Pb, and Bi respectively. Differences in the magnitude of signal spikes can be the result of many phenomena, such as sample inhomogeneity, and/or element-to-element differences in the vaporization and atomization behavior in the plasma.

CONCLUSIONS

In this study the effect of particle size and several laser types were investigated using fast data acquisition to determine those experimental parameters that influence the frequency and amplitude of large positive spikes in signal. Rapid measurement of many isotopes by TOF-MS shows that large increases in signal occur with correct isotopic abundance and occur at the same time for many different elements, although with varying degrees of magnitude. Further elucidation of experimental parameters and processes that decrease fractionation effects and promote stable, stoichiometric signals during laser ablation will further solidify LA-ICP-MS as an excellent tool for elemental analysis of solid samples.

REFERENCES

1. B. Hattendorf, C. Latkoczy, D. Günther, *Analytical Chemistry*, 2003, **75**, 341A-347A

2. J. J. Leach, L. A. Allen, D. B. Aeschliman, R. S. Houk, *Analytical Chemistry* 1999, **71**, 440-445

3. S. F. Boulyga, C. Pickhardt, J. S. Becker, *Atomic Spectroscopy*, 2004, **25**, 53-64

4. D. B. Aeschliman, S. J. Bajic, D. P. Baldwin, R. S. Houk, *Journal of Analytical Atomic Spectrometry*, 2003, **18**, 1008-1014

5. S. R. Kolrtyohann, S. J. Jones, D. A. Yates, *Analytical Chemistry,* 1980, **52**, 1965 - 1966

6. S. H. Jeong, O. V. Borisov, J. H. Yoo, X. L. Mao, R. E. Russo, *Analytical Chemistry*, 1999, **71**, 5123-5130

7. M. Guillong, D. Günther, *Journal of Analytical Atomic Spectrometry*, 2002, **17**, 831-837

8. H. R. Kuhn, D. Günther, *Analytical Bioanalytical Chemistry*, 2005, **17**, 434-441

9. T. Nomizu, S. Kaneco, T. Tanaka, D. Ito, H. Kawaguchi, *Analytical Chemistry*, 1994, **66**, 3000-3004

10. J. W. Olesik, *Applied Spectroscopy*, 1997, **51**, 158A-175A

11. S. E. Hobbs, J. W. Olesik, *Analytical Chemistry*, 1992, **64**, 274-283

12. F. Li, D. W. Armstrong, R. S. Houk, *Analytical Chemistry*, 2005, **77**, 1407-1413

13. M. Guillong, I. Horn, D. Günther, *Journal of Analytical Atomic Spectrometry*, 2003, **18**, 1224-1230

14. I. Horn, D. Günther, M. Guillong, *Spectrochimica Acta Part B: Atomic Spectroscopy*, 2003, **58**, 1837-1846

15. J Koch, A. Von Bohlen, R. Hergenroder, K. Niemax, *Journal of Analytical Atomic Spectrometry*, 2004, **19**, 267-272

16. D. Günther, C. A. Heinrich, *Journal of Analytical Atomic Spectrometry*, 1999, **14**, 1369-1374

17. I. Horn, M. Guillong, D. Günther, *Applied Surface Science*, 2001, **182**, 91-102

18. C. Liu, X. L. Mao, S. S. Mao, X. Zeng, R. Greif, R. E. Russo, *Analytical Chemistry*, 2004, **76**, 379-383

19. R. E. Russo, X. Mao, J. J. Gonzalez, S. S. Mao, *Journal of Analytical Atomic Spectrometry*, 2002, **17**, 1072-10757

20. V. Margetic, A. Pakulev, A. Stockhaus, M. Bolshov, K. Niemax, R. Hergenroder, *Spectrochimica Acta Part B: Atomic Spectroscopy*, 2000, **55**, 1171-1785

21. R. Hergenroder, O. Samek, V. Hommes, *Mass Spectrometry Reviews*, **2006**, 25, 551-572

22. I. Horn, F. von Blanckenburg, *Spectrochimica Acta Part B: Atomic Spectroscopy*, 2007, **62**, 410-422

23. B. Kozlov, A. Saint, A. Skroce, *Journal of Analytical Atomic Spectrometry*, 2003, **18**, 1069-1075

24. M.Guillong, H. R. Kuhn, D. Gunther, *Spectrochimica Acta Part B: Atomic Spectroscopy*, 2003, **58**, 211-230

25. H. Endert, A. Galvanauskas, G. Sucha, R. Patel, M. Stock, *RIKEN Rev*, 2002, **43**, 23-27

26. E. O. Knutson, K. T. Whitby, *J. Aerosol Sci.*, 1975, **6**, 443-451

27. H. R. Kuhn, J. Koch, R. Hergenroder, K. Niemax, M. Kalberer, D. Günther, *Journal of Analytical Atomic Spectrometry*, 2005, **20**, 894-900

28. H. R. Kuhn, M. Guillong, D. Gunther, *Analytical and Bioanalytical Chemistry*, 2004, **378**, 1069-1074

29. S. E. Jackson, D. Günther, *Journal of Analytical Atomic Spectrometry*, 2003, **18**, 205-212

30. D. J. Douglas, J. B. French, *Journal of Analytical Atomic Spectrometry*, 1988, 3, 743-747

31. H. R. Kuhn, D. Günther, *Analytical Chemistry*, 2003, **75**, 747-753

32. J. Koch, L. Feldmann, N. Jakubowski, K. Niemax, *Trends in Optics and Photonics*, 2002, **69**, 5/1-5/3

33. N. Saetveit, S. J. Bajic, D. P. Baldwin, R. S. Houk, *Journal of Analytical Atomic Spectrometry*, in press

34. J. Gonzalez, C. Liu, X. Mao, R. E. Russo, *Journal of Analytical Atomic Spectrometry,* 2004, **19**, 1165-1168

35. F. Poitrasson, X. Mao, S. S. Mao, R. Freydier, R. E. Russo, *Analytical Chemistry*, 2003, **75**, 6184-6190

36. H. Pang, D. R. Wiederin, R. S. Houk, E. S. Yeung., *Analytical Chemistry*, 1991, **63**, 390-394

37. R. E. Russo, X. L. Mao, O. V. Borisov, H. Liu, *Journal of Analytical Atomic Spectrometry*, 2000, **15**, 1115-1120

38. J. S. Becker, D. Tenzler, *Fresnius' Journal of Analytical Chemistry*, 2001, **370**, 637-640

Table 1. Parameters for Data Acquisition for Thermo Finnigan Element ICP-MS

Magnet Settling Time	0.001 s
Sampling Time	0.0015 s
Samples Per Peak	10
Mass Window	10%
Time per Data Point	**0.006 s**

Table 2. Voltage Settings for Optimass 8000 ICP-oa-TOF-MS.

Skimmer	-1200 V	Fill	-35 V
Extraction	-1000 V	Fill Bias	0.50 V
Z1	-800 V	Fill Grid	0 V
Y Mean	-200 V	Pushout Plate	455 V
Y Deflection	0 V	Pushout Grid	-580 V
Z Lens Mean	-1150 V	Blanker	200 V
Lens Body	-180	Reflectron	690 V

Table 3. Measured skew values for tube or coiled particle separation devices.

Number of Turns	Skew
0	24.3
1	4.11
2	5.09
3	4.23
4	4.99
5	4.98

Table 4. Isotope ratios for Sn$^+$ signal spikes in Figure 10.

	m/z	*117*	*118*	*119*
Entire Signal	Integrated Signal (c/s)	1.82×10^8	5.55×10^8	2.10×10^8
	Measured Abundance (%)	7.77	23.72	8.96
Spike at 2.763 s	Signal (c/s)	5.17×10^6	8.75×10^6	6.30×10^6
	Measured Abundance (%)	10.34	17.50	12.62
Spike at 3.003 s	Signal (c/s)	2.29×10^6	4.31×10^6	1.86×10^6
	Measured Abundance (%)	10.96	20.62	8.88
	Natural Abundance (%)	**8.58**	**24.20**	**7.68**
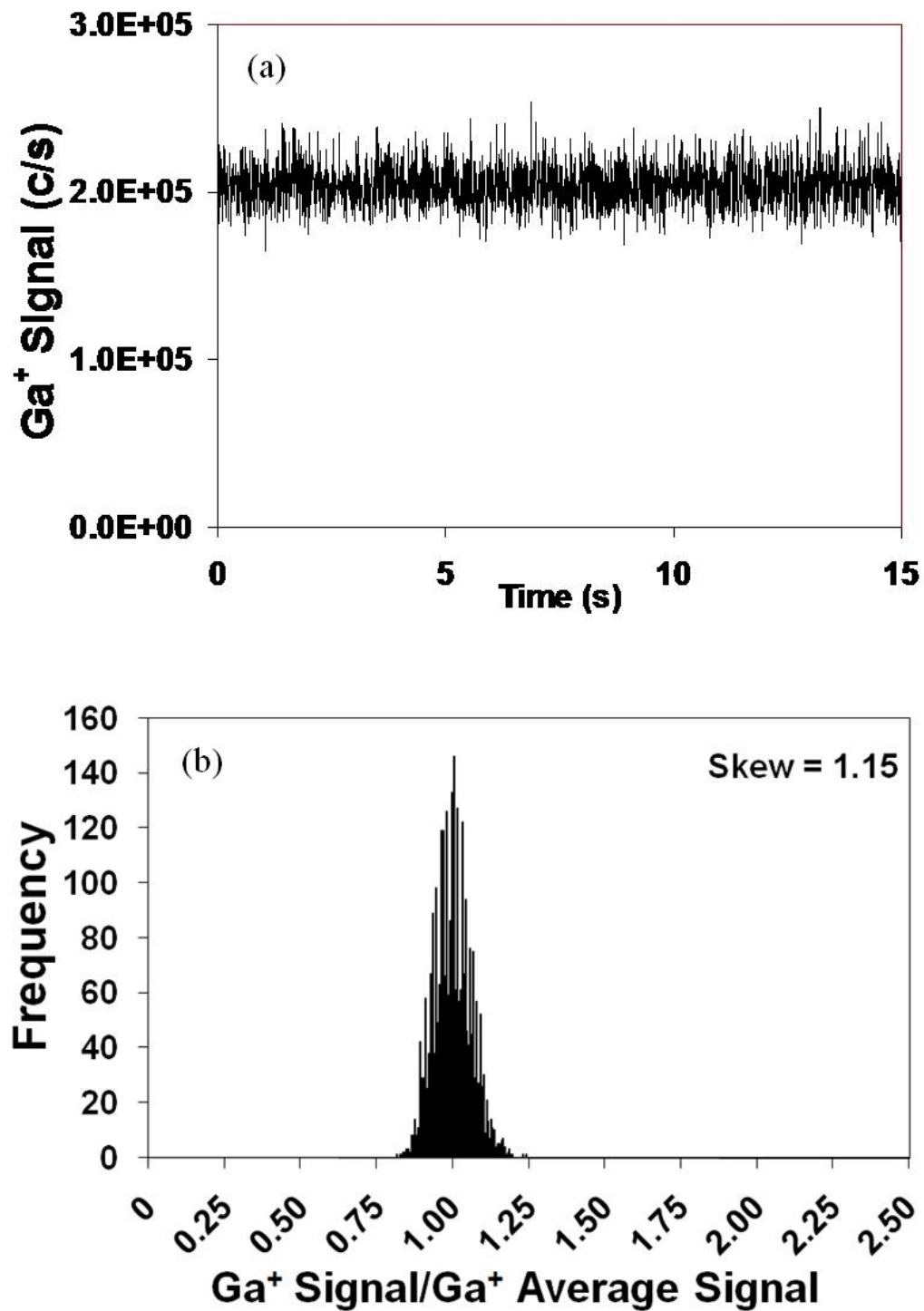
Figure 1. Plots of (a) signal as a function of time for 1 ppb solution of Ga with the magnetic sector ICP-MS, and (b) its histogram with a bin size of 0.005.
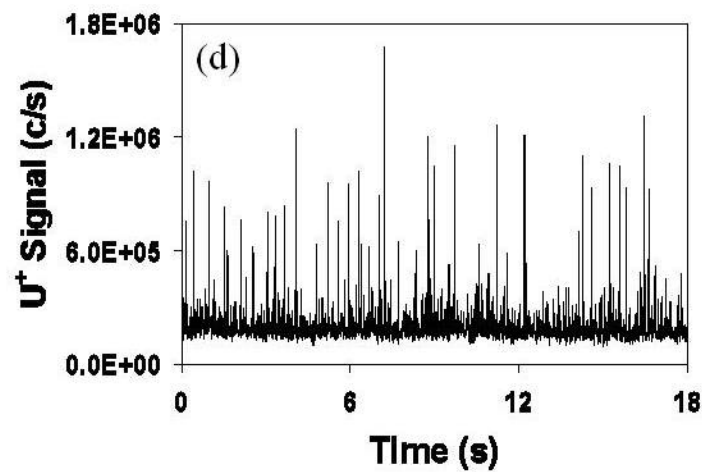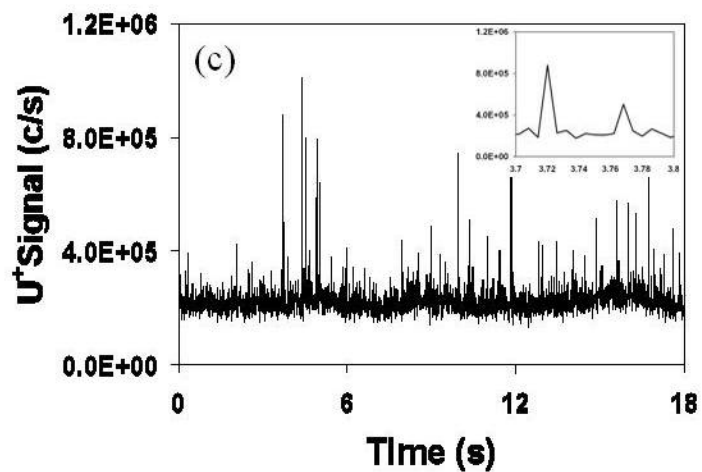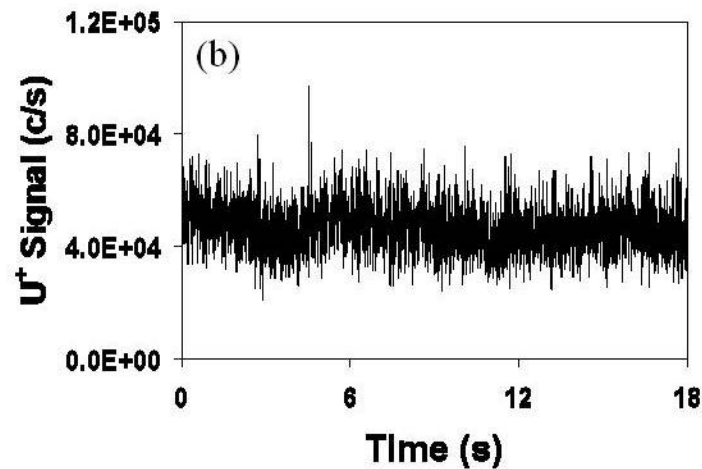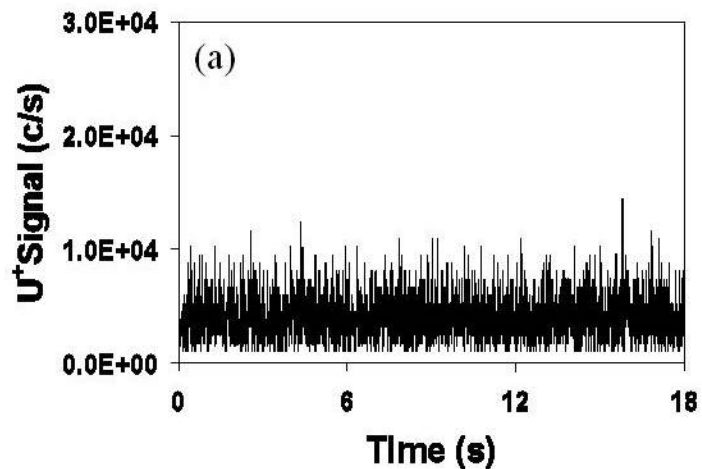
Figure 2. Signal vs. time plots for $^{238}U^+$ from NIST 610 for aerosols at DMA settings of (a) 100 nm (b) 200 nm (c) 500 nm (d) 1000 nm. Note changes in vertical scale. Inset of (c) shows finer time resolution for the plot. The magnetic sector was used.
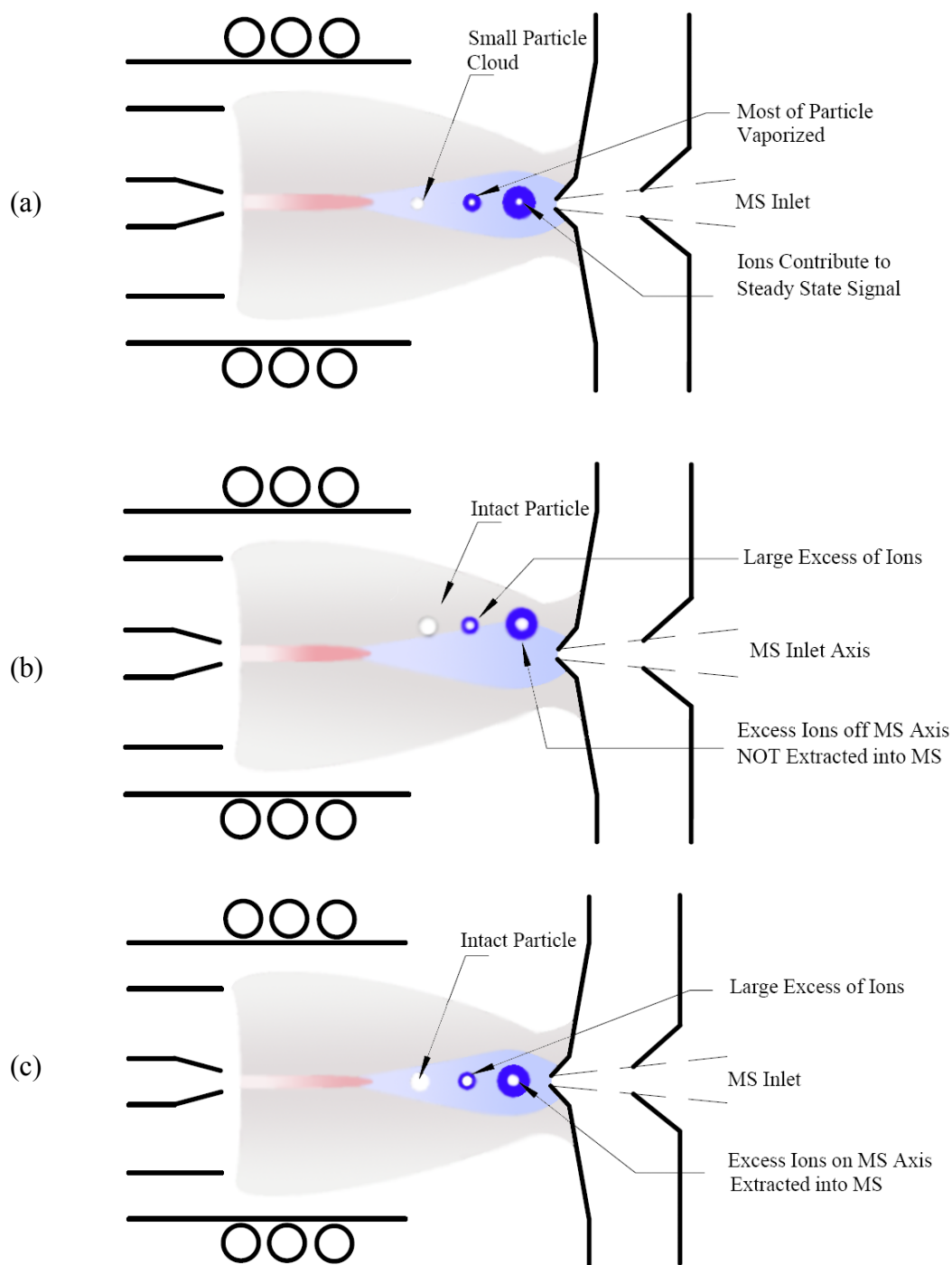
Figure 3. Illustrations depicting the fate of (a) a small particle being completely vaporized in the plasma, (b) a large particle off center of the MS axis, and (c) a large particle on-center with respect to the MS axis which would produce a large spike in signal intensity. The sampler is further downstream than usual to illustrate the effect.
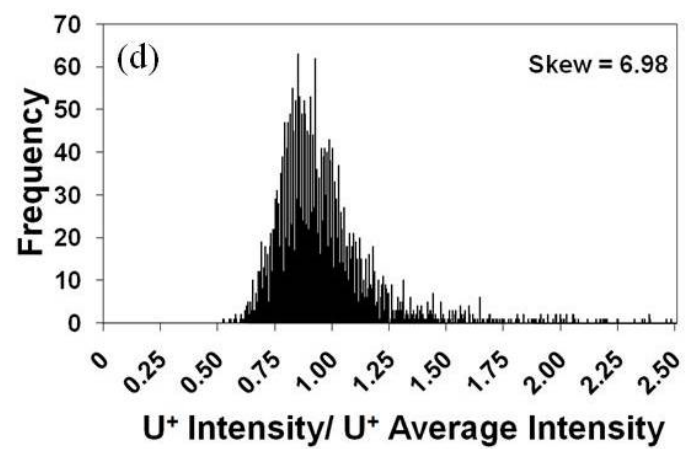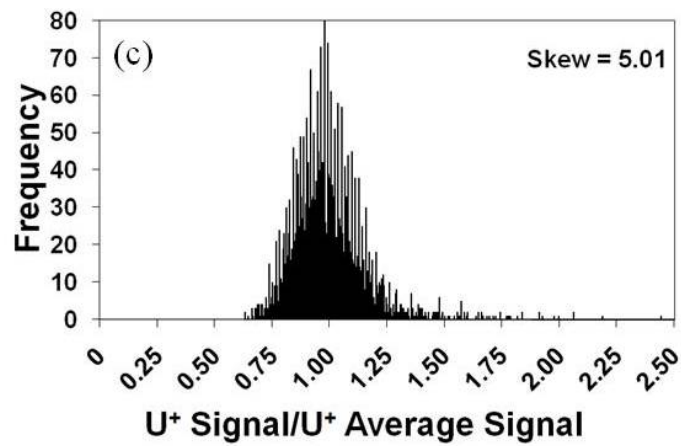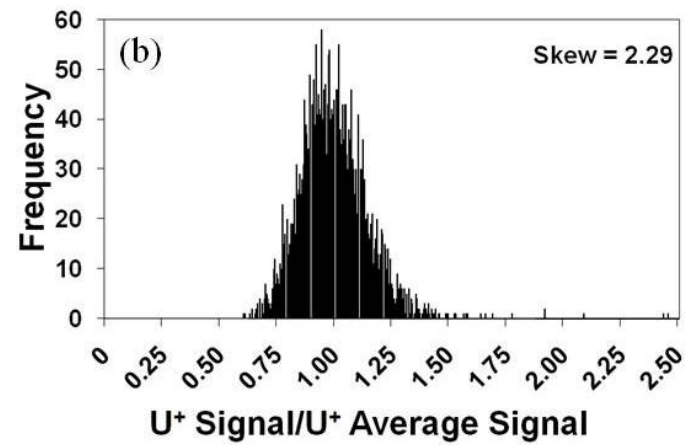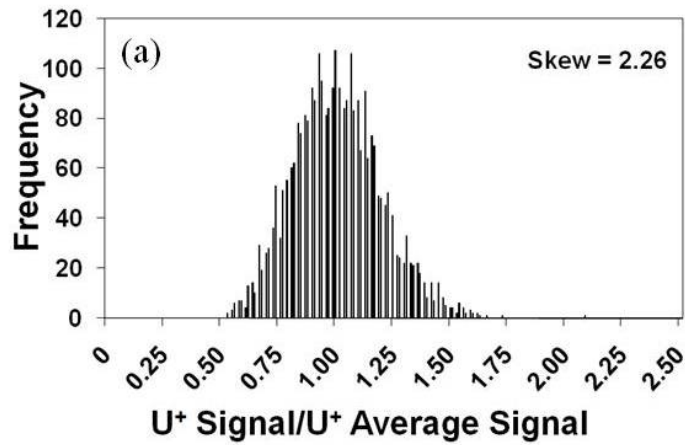
Figure 4. Histogram (bin size=0.005) plots of U^+ signal/U^+ average signal for particle sizes of (a) 200 nm (skew = 2.26), (b) 300 nm (skew = 2.29), (c) 400 nm (skew = 5.01), and (d) 800 nm (skew = 6.98).
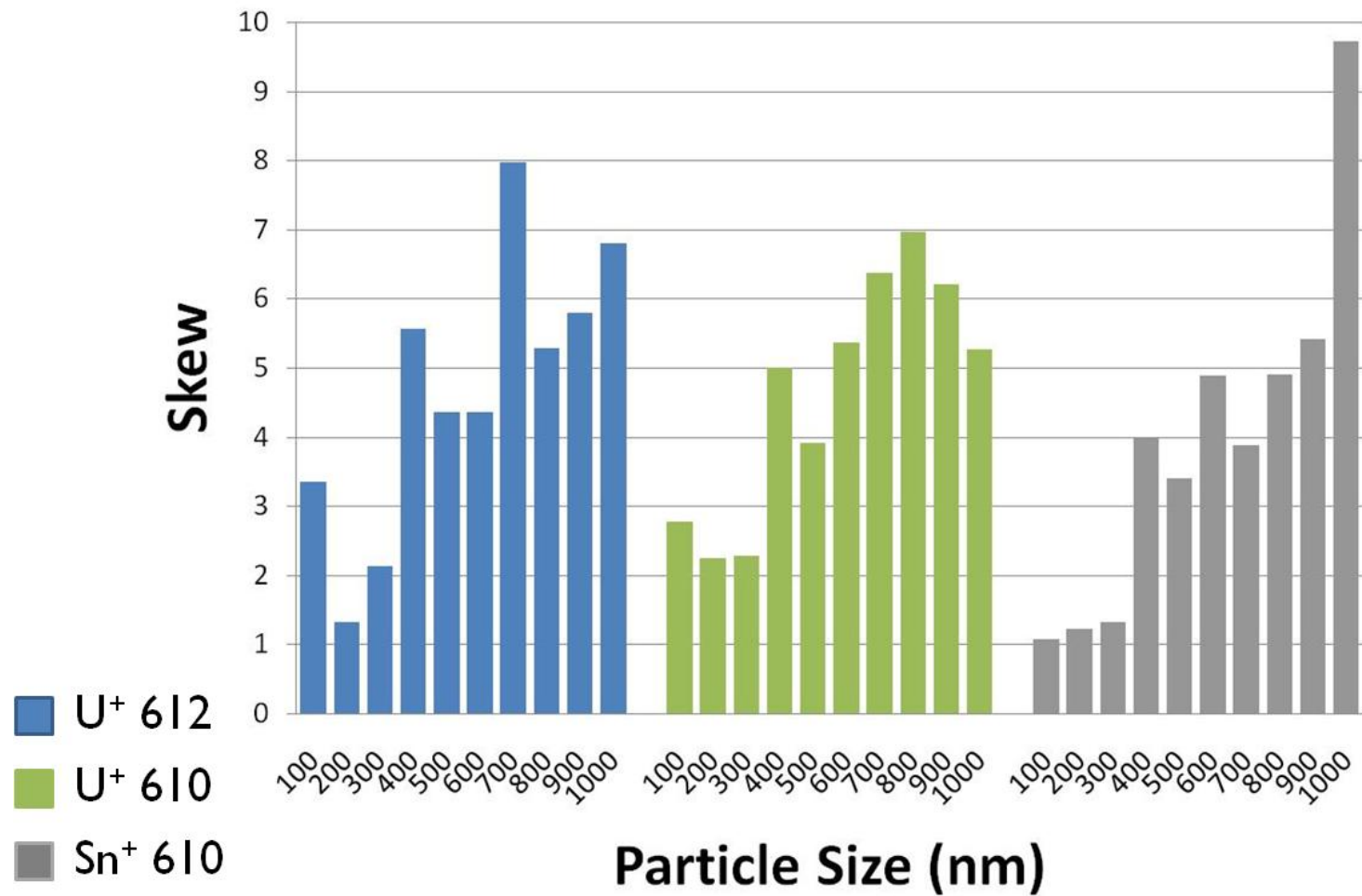
Figure 5. Skew value as a function of particle size selected by the DMA for U^+ signal/U^+ average signal from NIST 612, U^+ signal/U^+ average signal from NIST 610, and Sn^+ signal/Sn^+ average signal from NIST 610. The magnetic sector was used.
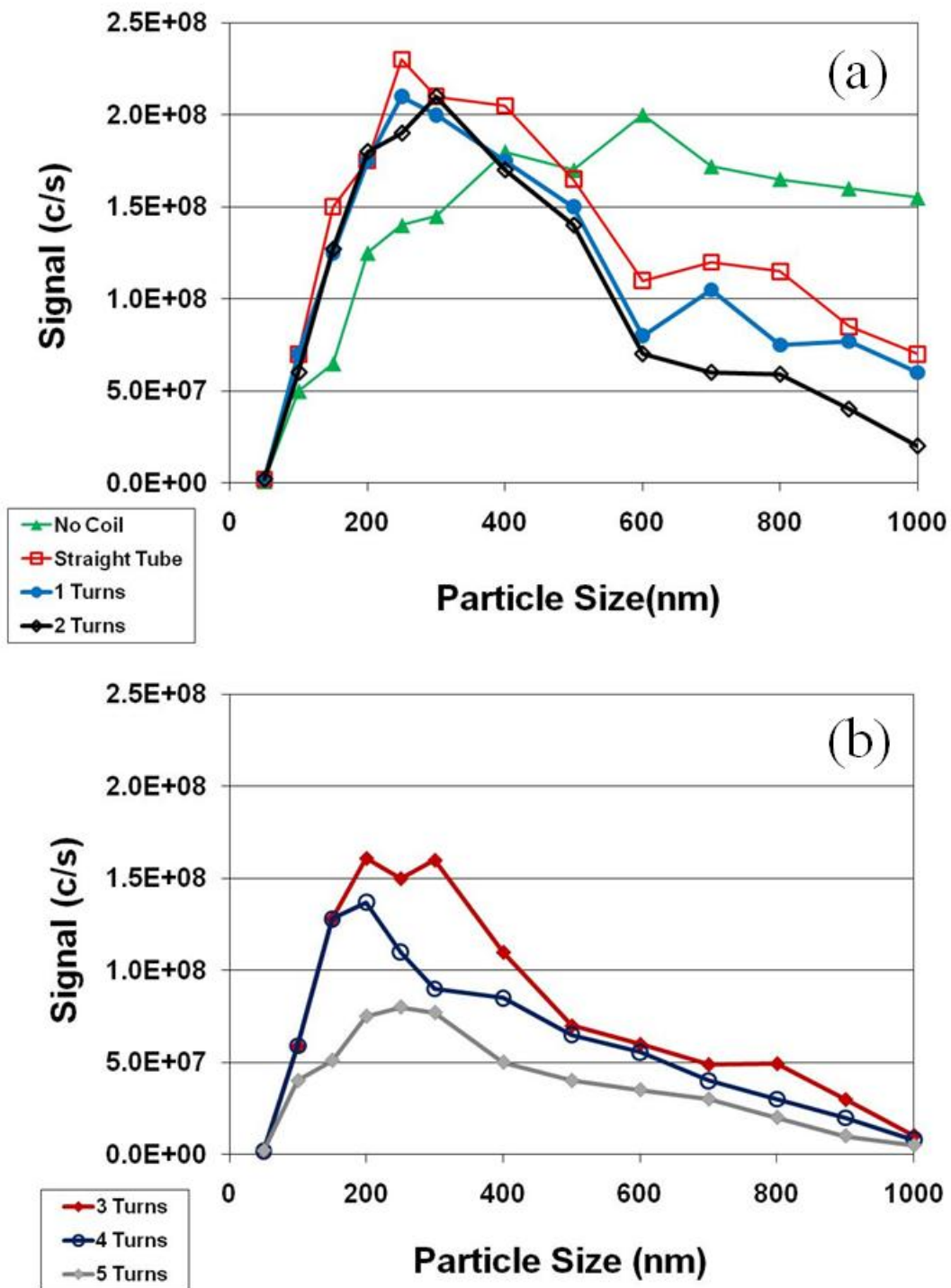
Figure 6. Plot of Cu$^+$ signal from NIST C1102 brass as a function of particle diameter selected by the DMA. The particle separation devices were either a straight tube or coils with 1 to 5 turns. Signal was measured with the magnetic sector ICP-MS.
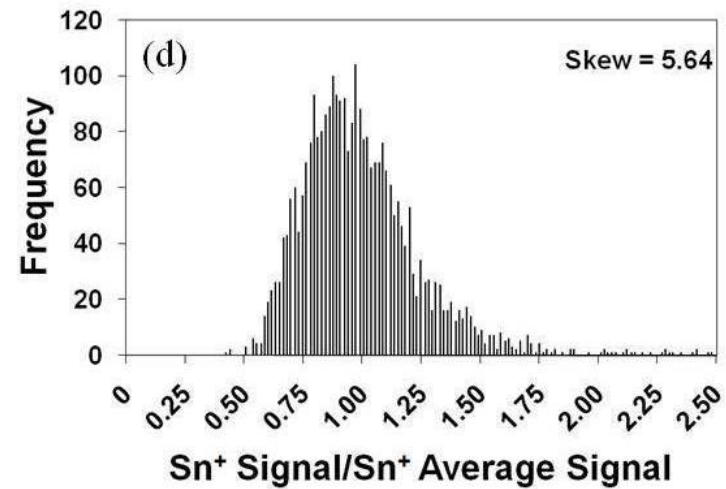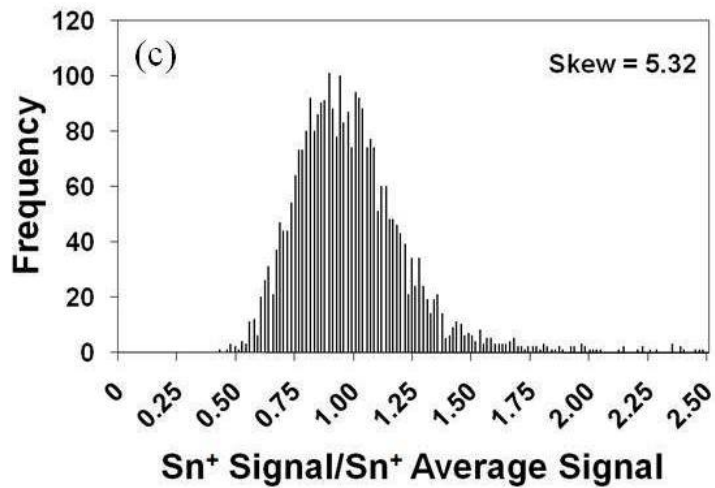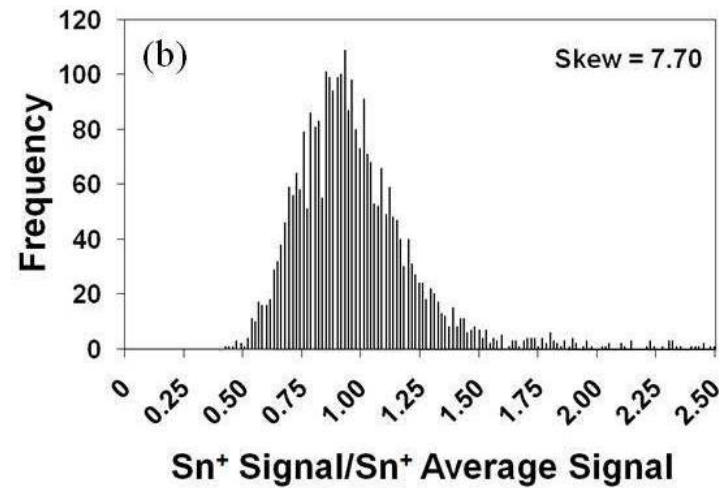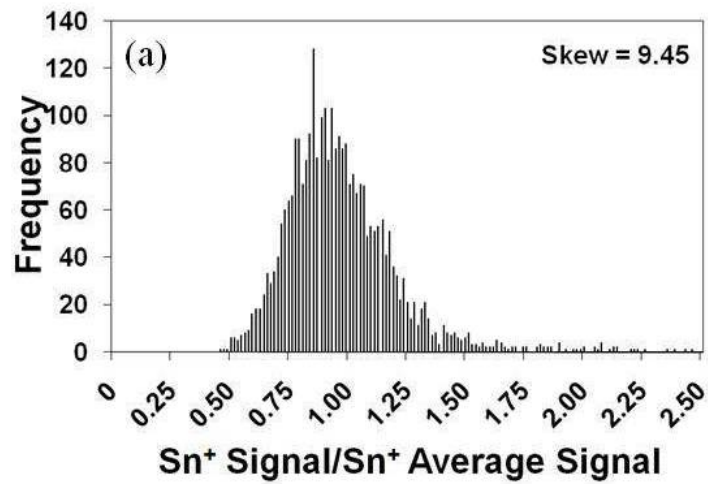
Figure 7. Histograms (bin size=0.005) for $^{118}Sn^+$ in NIST 610 while the LSX-500 laser was rastered at (a) 25 μm/s (b) 50 μm/s (c) 75 μm/s and (d) 100 μm/s. The DMA was set to pass only 800 nm particles. The magnetic sector was used.
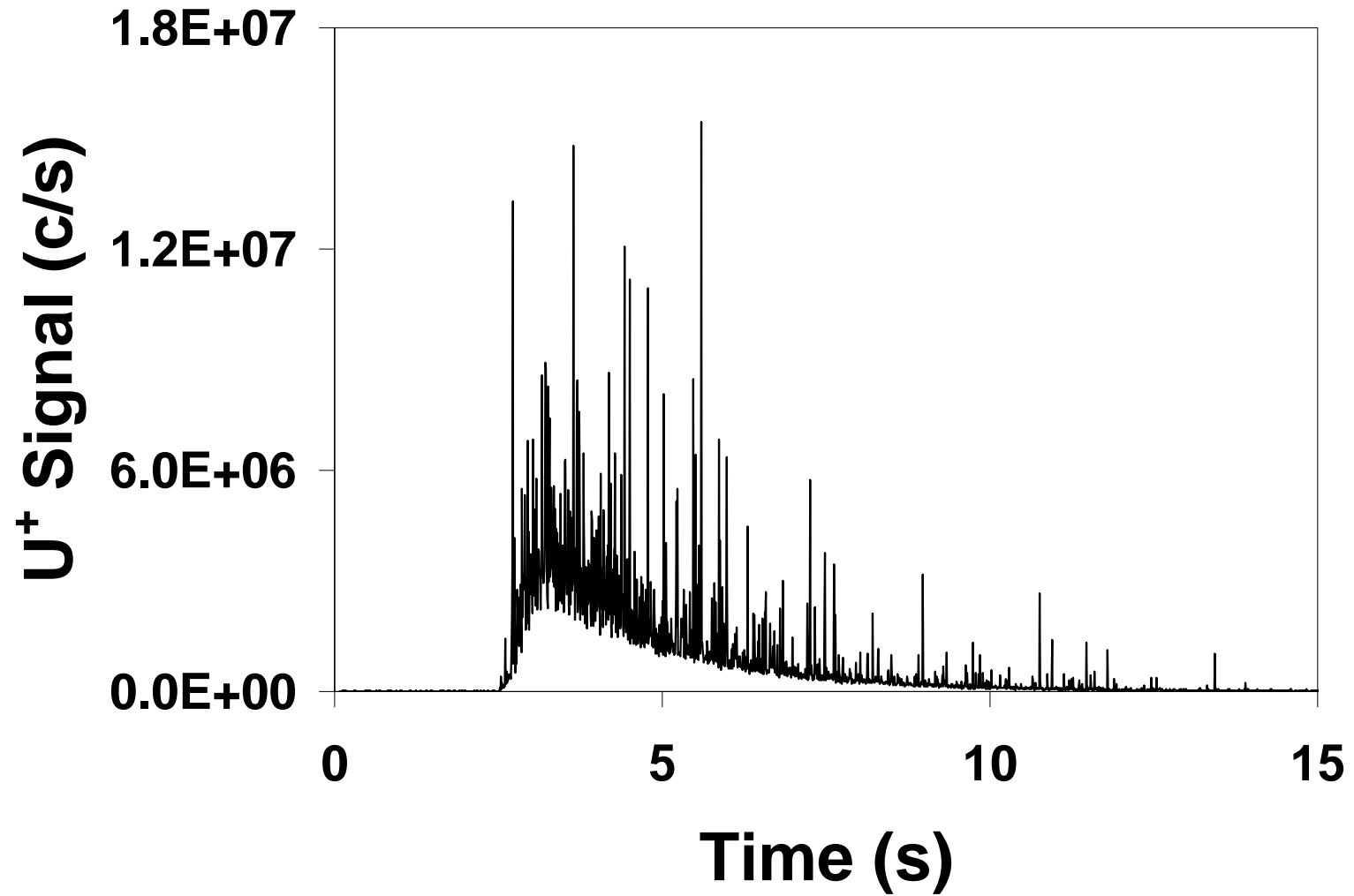
Figure 8. Signal plot as a function of time for single laser shot from the LSX 500 on NIST 610 glass standard reference material while monitoring the m/z for $^{238}U^+$. The magnetic sector was used without coils or the DMA.
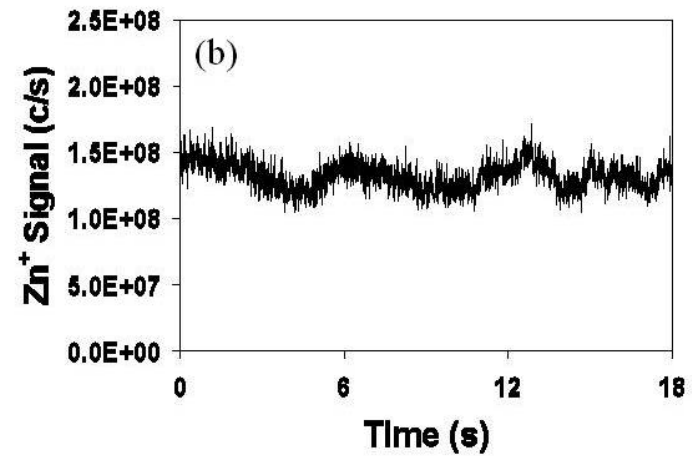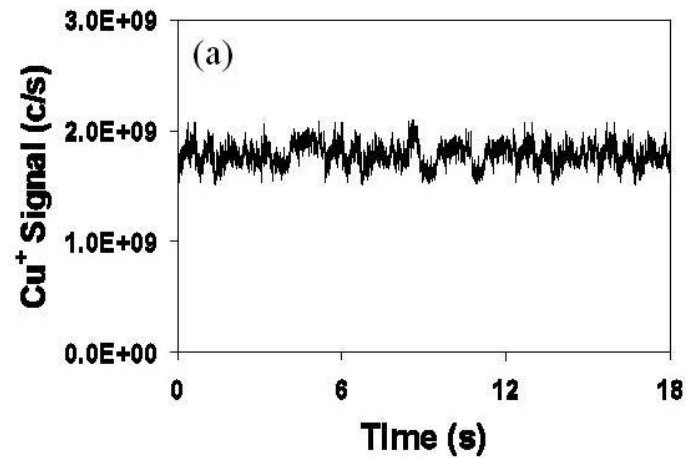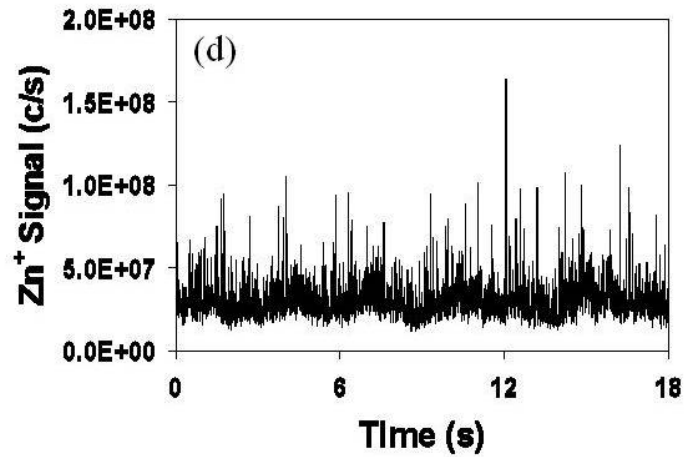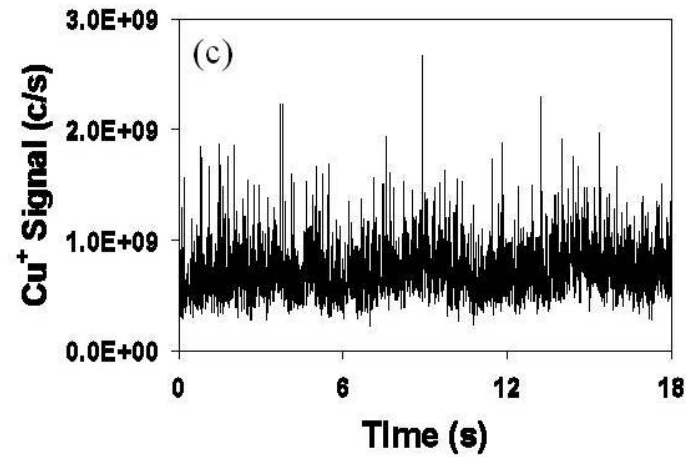
Figure 9. Signals from the magnetic sector ICP-MS for copper and zinc while ablating NIST C1102 brass. The lasers had pulse widths of 370 fs (a & b) and approximately 5 ns (c & d). Laser spot diameters were both approximately 50 μm, the laser raster rate was 32.5 μm/s, and the DMA was not used.
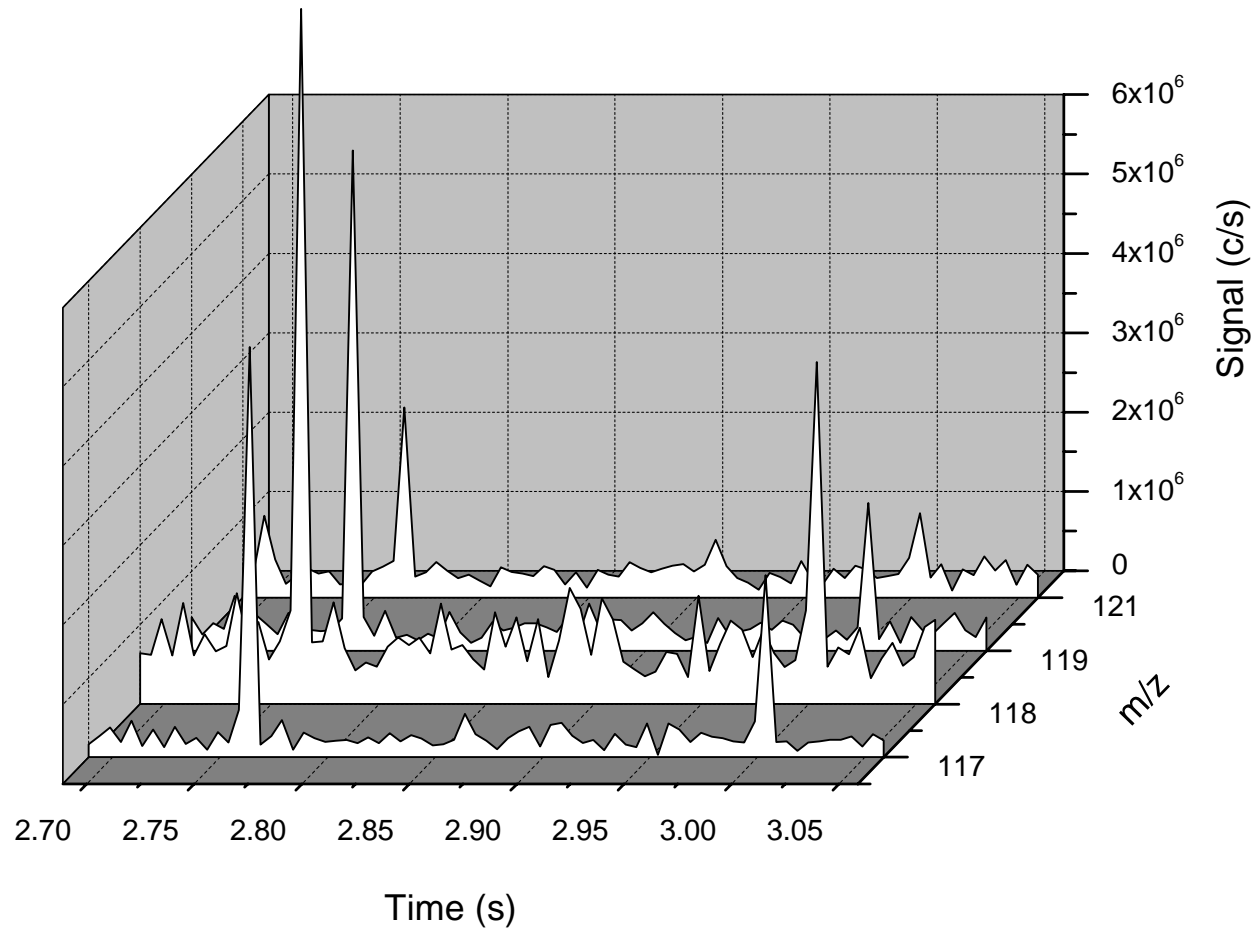
Figure 10.   TOF-MS signal as a function of time for m/z values 117, 118, 119, and 121 for NIST 1648 dust. The LSX 500 laser parameter were one laser shot, 200 μm laser spot diameter. Data acquisition time was 5 ms per data point. The coils or DMA were not used, here and in Figure 11.
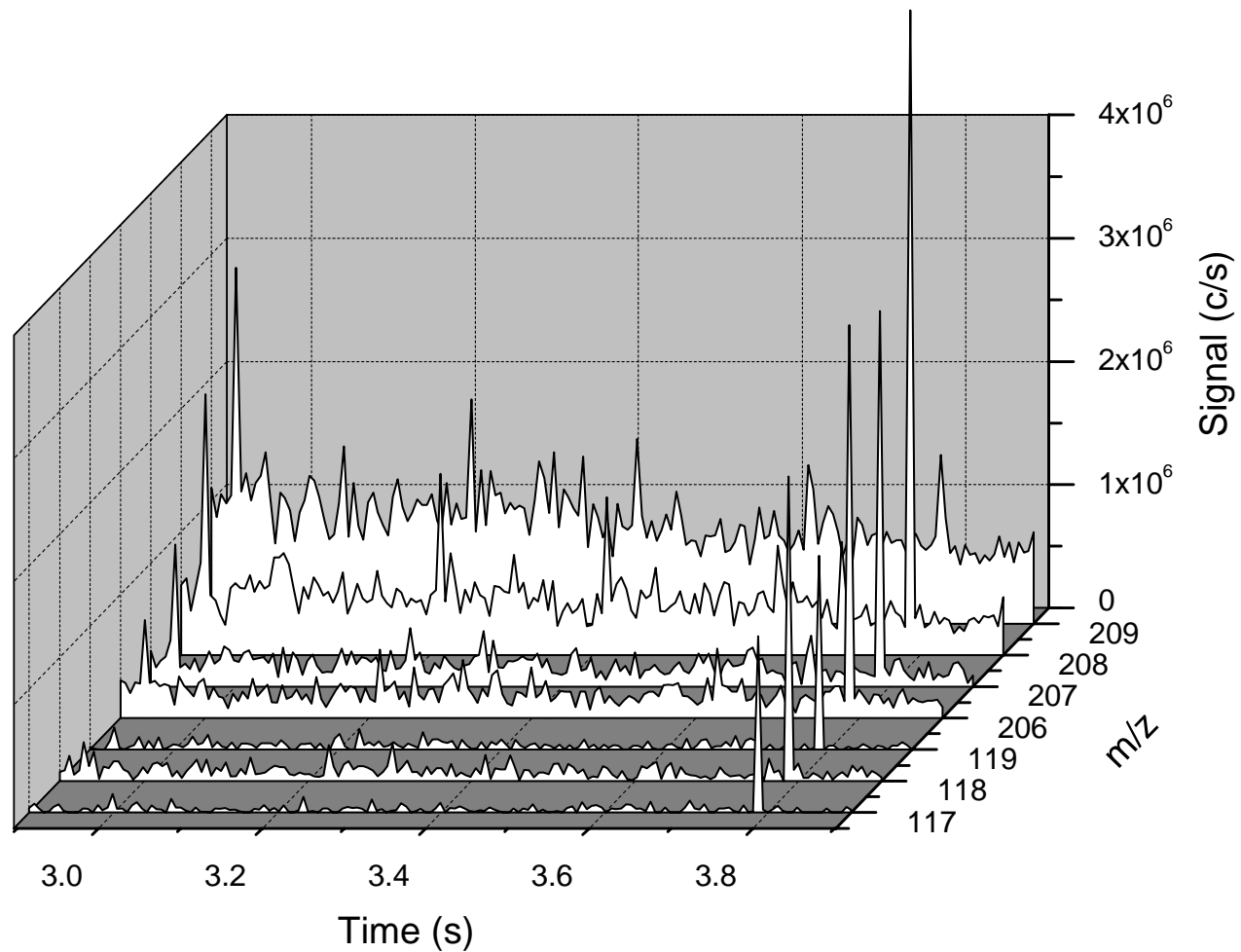
Figure 11. TOF-MS signal as a function of time for m/z values of 117, 118, 119, 206, 207, 208, and 209 for NIST 610 glass, The LSX 500 fired one laser shot with a 200 μm laser spot diameter. The TOF-MS acquired data at a rate of 6 ms per data point. The various elements are present at ~ 500 ppm.

CHAPTER 3. TIME-RESOLVED STUDIES OF PARTICLE EFFECTS IN LASER ABLATION INDUCTIVELY COUPLED PLASMA-MASS SPECTROMETRY: II. INVESTIGATION OF MO$^+$ IONS, EFFECT OF SAMPLE MORPHOLOGY, TRANSPORT GAS, AND BINDING AGENTS

D. C. Perdian, Stanley J. Bajic, David P. Baldwin, and R. S. Houk*

ABSTRACT

Time-resolved signals in laser ablation inductively coupled plasma mass spectrometry (LA-ICP-MS) are studied to determine the influence of experimental parameters on ICP-induced fractionation effects. Differences in sample composition and morphology, i.e. ablating brass, glass, or dust pellets, have a profound effect on the time-resolved signal. Helium transport gas significantly decreases large positive signal spikes arising from large particles in the ICP. A binder for pellets also reduces the abundance and amplitude of spikes in signal. MO$^+$ ions also yield signal spikes, but these MO$^+$ spikes generally occur at different times than their atomic ion counterparts.

* Corresponding Author

INTRODUCTION

Laser ablation inductively coupled plasma mass spectrometry (LA-ICP-MS) is now a common technique for the determination of trace and ultra trace elements in solid samples. However, there is still room for improvement. In particular, fractionation effects and a lack of matrix-matched standards often hinder quantification of the elements of interest.[1-5] Ongoing research to investigate the basic causes of fractionation may eventually increase the value of LA-ICP-MS as a quantitative technique.[6-8]

Our group has recently reported results exploring ICP-induced fractionation effects using fast data acquisition.[9] Large positive spikes in signal were observed that come from particles that have not completely vaporized and have a large excess of atomic ions surrounding the intact particle. When these intact particles pass through the plasma along the axis of the sampler-skimmer cones, the large excess of atomic ions around the intact aerosol particles causes a large, sudden increase in signal above the steady state or average level.[9] Photographic studies of aerosol particles in the ICP from LA experiments support our conclusions and show that large intact particles are often not completely vaporized. Additionally, a large excess of atomic ions surrounding the particles can be seen using optical emission.[10,11]

In general, these photographic observations during LA are consistent with many early studies from Olesik's lab on the fates of wet droplets and solid particles from nebulized solutions.[12,13] Recent studies have shown that laser ablation aerosols can consist of many large agglomerates and a few round solid particles (sizes > 200 nm). The big particles are largely responsible for ICP-induced fractionation.[14]

The first part of this study[9] showed that the amplitude and frequency of the spikes in signal are affected by the size of the aerosol particles that reach the plasma. Ablated aerosol particles smaller than a DMA size setting of 400 nm produce many fewer signal spikes than those aerosols that contain particles between 400 and 1000 nm. Also, laser parameters determine the degree to which the signal is affected by signal spikes. Specifically, the frequency and intensity of the large positive spikes increase as the laser is rastered across the sample more slowly. Large positive spikes are still observed with single laser shots.[9]

Reducing the pulse width of the laser has the greatest success at reducing the presence of spikes in signal. Many fewer spikes are seen when a 370 fs laser is used, compared to a 5 ns laser.[9] This supports previous research performed using lasers with pulse widths <1 ps for LA-ICP-MS.[14,15]

Others have shown that helium has many advantages over argon as the transport gas.[16] Because helium has a higher thermal conductivity it can remove energy from the ablation site more efficiently than argon. Faster removal of energy around the ablation site favors nucleation of ablated atoms into fine particles rather than condensation of material onto large particles. Reducing the opportunity for condensation onto existing particles decreases the number of large particles (> 200 nm diameter) in the resulting aerosol. Also, because helium is lighter than argon, it does not transport large (heavier) particles to the plasma as efficiently. Günther et al. also show that using helium as the transport gas significantly reduces the amount of material deposited around the ablation crater.[17] This deposited material may have different composition than the original solid. When re-ablated, it may also have an effect on the presence and amplitude of signal spikes.

Elemental analysis of solids often requires the measurement of samples that are comprised of various matrices, such as metals, powders, glasses, dust, etc. Sample composition affects the laser ablation process, specifically absorption of the laser light, crater formation, and aerosol generation.[18-20] Differences in sample composition (i.e., metals vs. powders vs. glass) can cause significant variations in analyte signal as well as differences in frequency and amplitude of signal spikes.

When LA-ICP-MS is employed for the analysis of solids in the form of powders, dust particulates, or other loose solid materials, a binder is often added to the sample. This mixture is then pressed into a pellet. The binder aids in the formation of the pellet; it essentially holds the pellet together giving it more mechanical strength.[22] In this experiment time-resolved signal behavior from urban dust particulate matter that is combined with a solid paraffin binding agent is compared to signal from a pellet that is prepared with no binder.

EXPERIMENTAL SECTION

Samples - NIST standard reference materials (National Institute of Standards and Technology, Gaithersburg, MD, USA) were used for this study, specifically NIST 610, 612, and 614 glasses, C1102 brass, as well as 1648 and 1649 urban dust particulates.

ICP-MS Devices - The ICP-MS devices are the same as those used in the previous study:[9] a magnetic sector instrument (Element 1, Thermo Finnigan, Bremen, Germany, integration time 1.5 ms) left sitting on one m/z value, and a time-of flight instrument (Optimass 8000 oa-

TOF ICP-MS, GBC Scientific Equipment, Dandenong, VIC Australia, scan time 3 ms). All ICP-MS conditions are the same as in Part I of this study.[9] Both the magnetic sector instrument and TOF instrument were not operated under conditions that maximize signal, as there are too many spikes too close together to be resolved readily. Rather, the aerosol gas flow rate is decreased by ~ 0.1 L/min from the value that provides the highest M^+ signals. Most results shown below were obtained using the magnetic sector instrument, except where it is specifically noted that the data were obtained using the TOF-MS.

Transport Gas - For experiments using helium as the transport gas, all the flow through the cell was helium at 0.70 L/min. Argon was added as additional gas downstream from the ablation cell in order to maintain a stable plasma. The gases were combined using a Y-shaped intersection. Total flow rates (transport + additional) were 1.20 to 1.40 L/min for both helium and argon. When argon was used for comparison to helium, the same experimental set up was used. An argon flow rate of 0.6 to 0.70 L/min was sent through the ablation cell, and additional argon was added via the Y-shaped intersection. As noted above, the aerosol gas flow rates were tuned individually for stable signal, which compromised maximum signal. These flow rate values were not corrected for differences in gauge response in the mass flow controller between He and Ar.

Laser – Only the Q-switched Nd:YAG laser, (LSX 500, CETAC Technologies, Omaha, NE, USA, 5 ns pulse width) was available for these experiments. Laser parameters and design were reported previously.[9]

Particle Selection – Devices for particle filtering or size selection were used only in Part I, not in this study.

Binder – Solid paraffin wax (Sigma Aldrich, St. Louis, MO USA) was combined with NIST 1649 urban dust particulates in a mass ratio of 5:1 or approximately 0.5 g dust sample to 0.1 g binding agent. The mixture was combined in a mull and pressed into an aluminum planchet. A pellet consisting only of NIST 1649 urban dust was also made without binder, for comparison.

Histograms and Skew Values. The data were exported to Excel and plotted as histograms with (individual signal)/(average signal) as the horizontal axis. Skew values were calculated using the corresponding statistical function in Excel.

RESULTS AND DISCUSSION

Effect of Sample Morphology - Sample composition and structure play an important role in the laser ablation process. The initial absorption, amount ablated, crater formation, redeposition of material, aerosol generation, and particle size distribution can vary widely for different sample materials such as urban dust, glass, and brass. Thus, the number and height of spikes in signal would also be expected to differ from material to material.

Figure 1 shows the signal vs. time plots for $^{238}U^+$ from NIST 612 glass (Fig. 1a) and NIST 1648 urban dust pellet (Fig. 1b). There are many more, larger spikes in U^+ signal

observed from the dust pellet (NIST 1648), made without a binding agent, and compared to NIST 612 glass, even though the steady state signals are comparable. Histogram plots (Fig. 1c & 1d) also show a large difference between the two different sample types. The skew value for the NIST 612 signal is 1.26, while the skew for the NIST 1648 signal is 23.5, for a bin size of 0.01.

These observations were expected because the NIST 1648 dust sample is merely a pressed agglomerate of particulates ranging in size from 3 to 50 μm.[24] The NIST glass reference material, however, is one solid piece of glass doped with trace metals. Ablation shatters the urban dust pellet and dislodges large pieces of material. The resulting aerosol is a distribution of much larger particles than those created during ablation of the smoother, more homogeneous glass sample.[25] This effect produces a greater number of large positive spikes in signal from the dust pellet, compared to the smooth, homogeneous glass sample. This behavior is seen for other elements; only U^+ is shown for brevity.

Signal vs. time plots for Sn^+ from NIST 610 glass and NIST C1102 brass (Fig. 2) are much more similar with respect to large signal spikes, compared to the Fig. 1. The histograms and subsequent skew values (3.42 for glass, 5.32 for brass, data not shown) are also much more similar than when comparing glass to the dust pellet.

Effect of Transport Gas - Prior research suggests that using helium as the ablation-transport gas would provide fewer large particles and signal plots with fewer, smaller spikes than argon.[17, 18] The signal as a function of time plots for $^{89}Y^+$ in NIST 1648 urban dust (Fig. 3) support this expectation. The plot for ablation in helium (Fig. 3a) has many fewer spikes,

and their amplitude is smaller. As stated previously the reduction of signal spikes is due to two phenomena. First, the high thermal conductivity of He removes energy from the ablation site more efficiently than argon, suppressing the coalescence of ablated material into overly large particles. Second, helium is approximately ten times lighter than argon and therefore cannot support larger aerosol particles as efficiently.

However, the histograms show that the signal distribution is not inherently better for helium than argon. The helium histogram has a skew value of 4.28, similar to that for argon (2.43). We offer the following explanation for this anomaly. In this instance, with helium there are far fewer large positive spikes, but many of the medium-sized particles are also lost. The removal of the medium sized particles contributes to a large loss of steady state signal, which is evident from comparison of the baselines signals in Figs. 3a and 3b. This effect amplifies the contribution of the large spikes to the skew value.

Under normal conditions helium usually offers a signal enhancement compared to argon.[26] For this experiment, though, the plasma conditions were tuned for maximum signal stability, and the M^+ signal observed with helium carrier gas is lower than that for argon.

MO^+ Behavior - The plots of signal as a function of time for oxide ions have important similarities, as well as differences, compared to plots for atomic ions. MO^+ ions do indeed produce spikes in signal, much like their M^+ progeny (Figure 4). However the frequency and prominence of the MO^+ spikes occur is significantly less than for M^+.

The magnetic sector ICP-MS can measure signals at only one m/z value at a time at this time resolution. Concurrent measurement of U^+ along with UO^+ ion (Figure 5) using the

TOF-MS supports these results. Consider the five prominent $^{238}U^+$ spikes indicated by asterisks in Fig. 5. The spike/average signal ratios from these five spikes are 2.15, 2.70, 5.21, 3.68, and 2.24. The spike/average signal ratios for $^{238}U^{16}O^+$ spikes at the same times are 0.44, 3.84, 0.97, 0.72, and 1.17. Only one of these five $^{238}U^+$ spikes (i.e., the one at ~ 0.68 s) also has a prominent spike for $^{238}U^{16}O^+$.

This observation can be explained from previous photographic studies using YO, Y and Y^+ emission.[10,11] The region of visible Y^+ emission is much larger than that of YO surrounding the particles in the ICP. The region around the particles that contains a large concentration of both Y^+ and YO^+ is most likely very small and not sampled frequently by the sampler and skimmer cones. The white streaks from YO and/or neutral Y atoms are very thin, showing that these species are quickly converted into Y^+ ions, which make thick, spherical, blue vapor clouds. The Y^+ ions form at the expense of YO and YO^+ species. Thus, M^+ spikes are much more abundant than MO^+ spikes, assuming the behavior of Y is typical of that for other elements.

Effect of a Binder - Signal versus time plots and histograms for $^{89}Y^+$ are shown for NIST 1649 dust pellet pressed with and without a binder (Fig. 6). For the Y^+ signals, the frequency and amplitude of spikes is reduced when the binder is included in the pellet. The binder holds the pellet together better, making it more like one complete solid mass, rather than the particulates merely pressed together loosely. The binder allows the sample to be ablated more cleanly with respect to crater formation and aerosol generation, and has been used to provide better precision for laser ablation experiments.[27] The sample pressed with a binder

most likely produces an aerosol with a lower fraction of large particles than the sample that is prepared without the binder.

Using the binder does not affect the skew value much (3.03 vs 3.70). Such a small difference in skew value is not statistically significant given the precision of the experiments. However a bimodal distribution is seen in the histogram when the binder is used (Fig. 6d); there may be two distinct sizes of aerosol particles. Another important aspect of this experiment is that the use of a binding agent reduces the amount of spikes, but there is also a loss of steady state signal. The baseline signal for Y^+ drops by roughly a factor of two, when comparing the sample of NIST 1649 alone versus NIST 1649 sample prepared with the binder. This drop in signal would be problematic if ultra trace analysis was the goal of the experiment. Recently, Sharp et al.[28] have shown that using highly absorbing binders can actually increase the signal for a given sample. This idea shows promise for quantification of unknown samples using standards that do not closely match the samples.

Closer examination of the steady state signals for Y^+ ions in Fig. 6a shows slow fluctuations as the signal is being measured. The Y^+ signal decreases from the start of the scan until about 6 seconds have passed and then starts to increase again until the end of the run. The Y^+ signal takes a significant dip in intensity from 2 to ~7 seconds. These fluctuations in signal were consistently seen throughout the experiments analyzing the NIST 1649 when the binder was used. It must be noted that this variation in signal very well may occur without the binder as well; however the large spikes could mask their appearance. This problem of fluctuating signal may be attributed largely to the inhomogeneity of the sample; some areas may be more concentrated with binder whereas some areas are more concentrated

with the sample. Inhomogeneity of the sample causing a dip in signal at ~4s may also contribute to the bimodality of the histogram (Fig. 6d).

CONCLUSIONS

Experimental parameters have a profound effect on signal variation in laser ablation ICP-MS experiments. Use of helium as the transport gas reduced the number of signal spikes, but at the expense of steady-state signal. The use of a binding agent when ablating loose solid materials pressed into pellet form reduced the amount of positive spikes in signal, but also introduced a new signal variation stemming from the heterogeneity of the sample pellet. Further fundamental experiments for laser ablation could provide insight into ways to reduce the effect of ICP-induced fractionation effects.

ACKNOWLEDGEMENTS

REFERENCES

1. D. Guenther, B. Hattendorf, *Trends Analytical Chemistry*, 2005, **24**, 255-265

2. D. J. Figg, J. B. Cross, C. Brink, *Applied Surface Science* 1998, **129**, 287-291

3. O. V. Borisov, X. Mao, R. E. Russo, *Spectrochimica Acta Part B: Atomic Spectroscopy*, 2000, **55**, 1693-1704

4. A. J. G. Mank, P. R. D. Mason, *Journal of Analytical Atomic Spectrometry,* 1999, **14**, 1143-1153

5. B. Kozlov, A. Saint, A. Skroce, *Journal of Analytical Atomic Spectrometry*, 2003, **18**, 1069-1075

6. Z. Chen, J. Anal. Atom. Spectrom., 1999, 14, 1823-1828

7. R. E. Russo, X. L. Mao, O. V. Borisov, H. Liu, *Journal of Analytical Atomic Spectrometry*, 2000, **15**, 1115-1120

8. S. E. Jackson, D. Guenther, *Journal of Analytical Atomic Spectrometry*, 2003, 18, 205-212

9. D. C. Perdian, Stan J. Bajic, David P. Baldwin, and R. S. Houk, *Journal of Analytical Atomic Spectrometry*, 2008, **23**, 325-335.

10. D. B. Aeschliman, S. J. Bajic, D. P. Baldwin, R. S. Houk, *Journal of Analytical Atomic Spectrometry*, 2003, **18**, 1008-1014

11. D. Zamzow, S. J. Bajic, D. P. Baldwin, R. S. Houk, manuscript in progress. European Winter Conference Plasma Spectrometry, KN02, Taormina, Italy, Fall 2007

12. J. W. Olesik, *Applied. Spectroscopy*, 1997, **51**, 158A-175A

13. S. E. Hobbs, J. W. Olesik, *Analytical Chemistry*, 1992, **64**, 274-283

14. B. Hattendorf, C. Latkoczy, D. Günther, *Analytical Chemistry*, 2003, **75**, 341A-347A

15. R. E. Russo, X. Mao, J. J. Gonzalez, S. S. Mao, *Journal of Analytical Atomic Spectrometry*, 2002, **17**, 1072-1075

16. R. Hergenroder, O. Samek, V. Hommes, *Mass Spectrometry Reviews*, 2006, **25**, 551-572

17. D. Günther, C. A. Heinrich, *Journal of Analytical Atomic Spectrometry*, 1999, **14**, 1363-1368

18. I. Horn, D. Günther, *Appl. Surf. Sci.*, 2003, **207**, 144-157

19. P. M. Outridge, W. Doherty, and D. C. Gregoire, *Spectrochimica Acta Part B: Atomic Spectroscopy*, 1996, **51**, 1451-1462

20. P. M. Outridge, W. Doherty, and D. C. Gregoire, *Spectrochimica Acta Part B: Atomic Spectroscopy*, 1997, **52**, 2093-2102

21. M. Guillong, H. R. Kuhn, D. Günther, *Spectrochimica Acta Part B: Atomic Spectroscopy*, 2003, **58**, 211-220

22. K. E. Jarvis, A. L. Gray, R. S. Houk, *Handbook of ICP-MS*, Blackie, New York, 1992, ch. 10, pp. 295-296

23. E. O. Knutson, K. T. Whitby, *J. Aerosol Sci.*, 1975, **6**, 443-451

24. A. Fajgelj, R. Zeisler, *Fresnius' Journal Analytical Chemistry*, 1998, **360**, 442-445

25. D. Bleiner, personal communication, 2003

26. D. Gunther, C. A. Heinrich, *Journal of Analytical Atomic Spectrometry*, 1999, **14**, 1363-1368

27. A. A. Van Heuzen, Morsink, J. B. W., *Spectrochimica Acta Part B: Atomic Spectroscopy*, 1991, **46**, 1819-1828

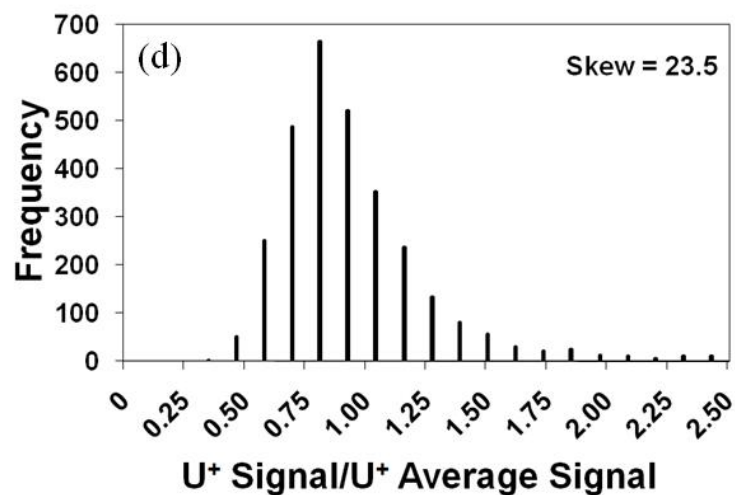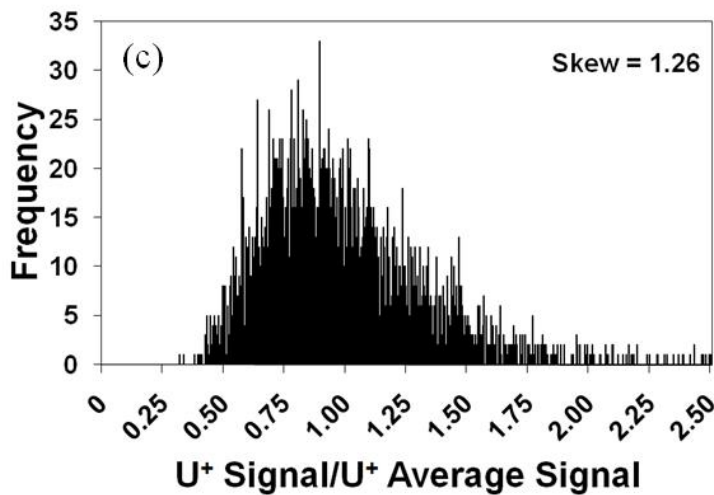28. C. O'Connor, M. R. Landon, B. L. Sharp, *Journal of Analytical Atomic Spectrometry*, 2007, **22**, 273-282
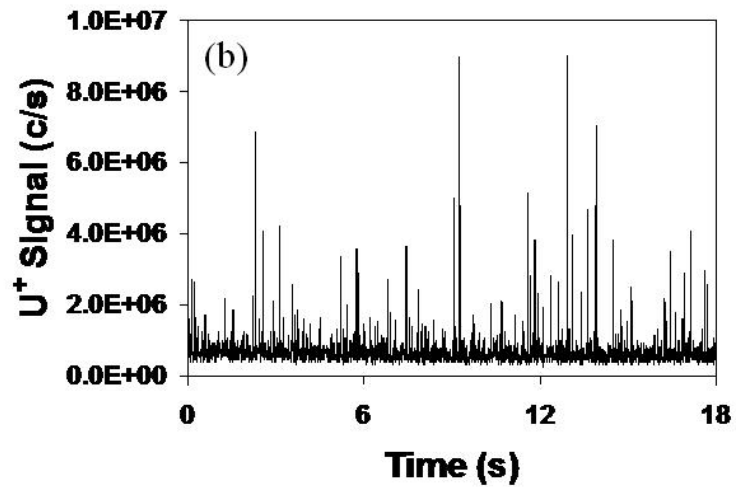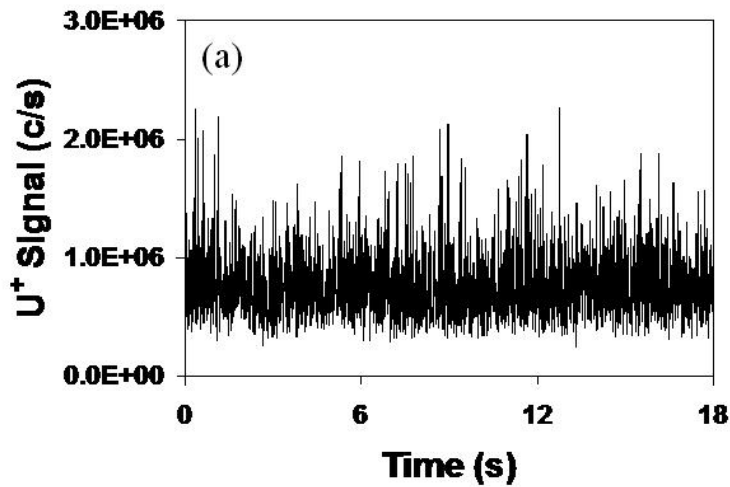
Figure 1. Plots of signal for $^{238}U^+$ as a function of time while ablating (a) NIST 612 glass and (b) NIST 1648 urban dust samples. Note difference in vertical scales. Histogram plots for the signals of $^{238}U^+$ in (c) NIST 612 glass and (d) NIST 1648 urban dust. Signal was measured with the magnetic sector ICP-MS.
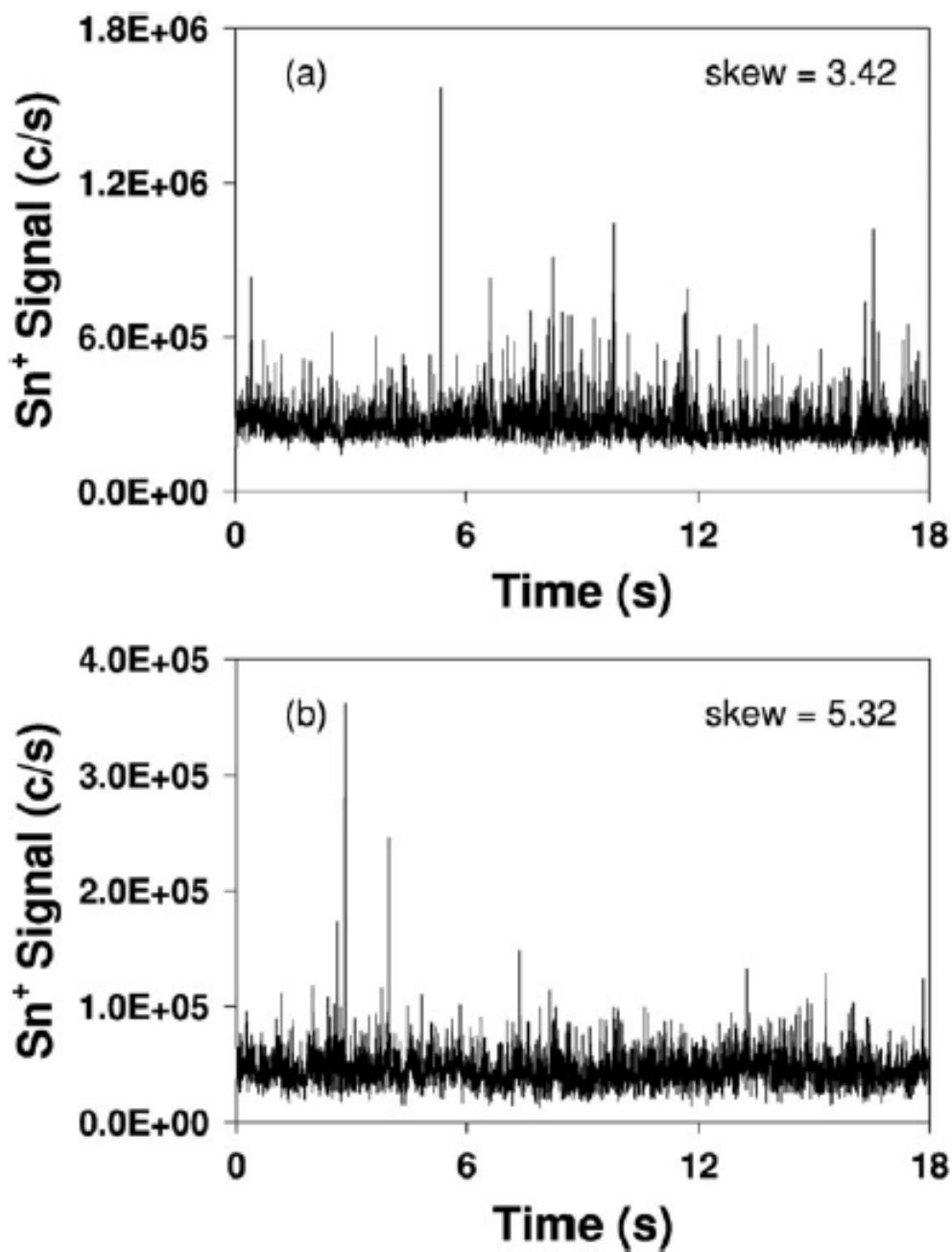
Fig. 2 Signal versus time plots for $^{118}Sn^+$ signal from (a) NIST 612 Glass, and (b) NIST C1102 Brass standard reference materials. The vertical scales have been selected to put the baseline signals at about the same levels. Skew values from histograms are also given. Signal was measured with the magnetic sector ICP-MS.
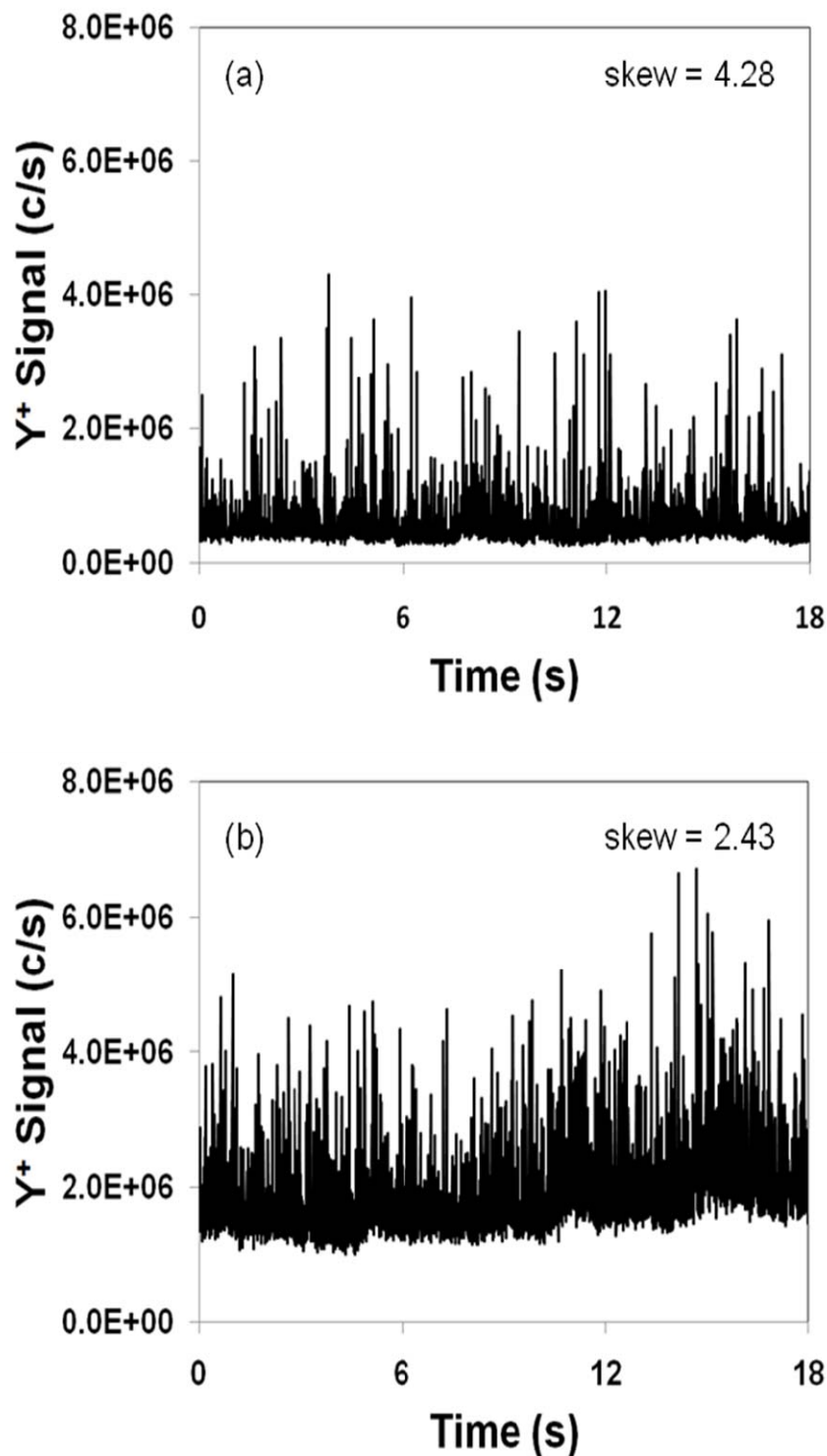
Figure 3. Yttrium ion signal a function of time and skew values while ablating NIST 1648 dust pellet using (a) helium and (b) argon as the transport gas through the ablation cell. Signal was measured with the magnetic sector ICP-MS.
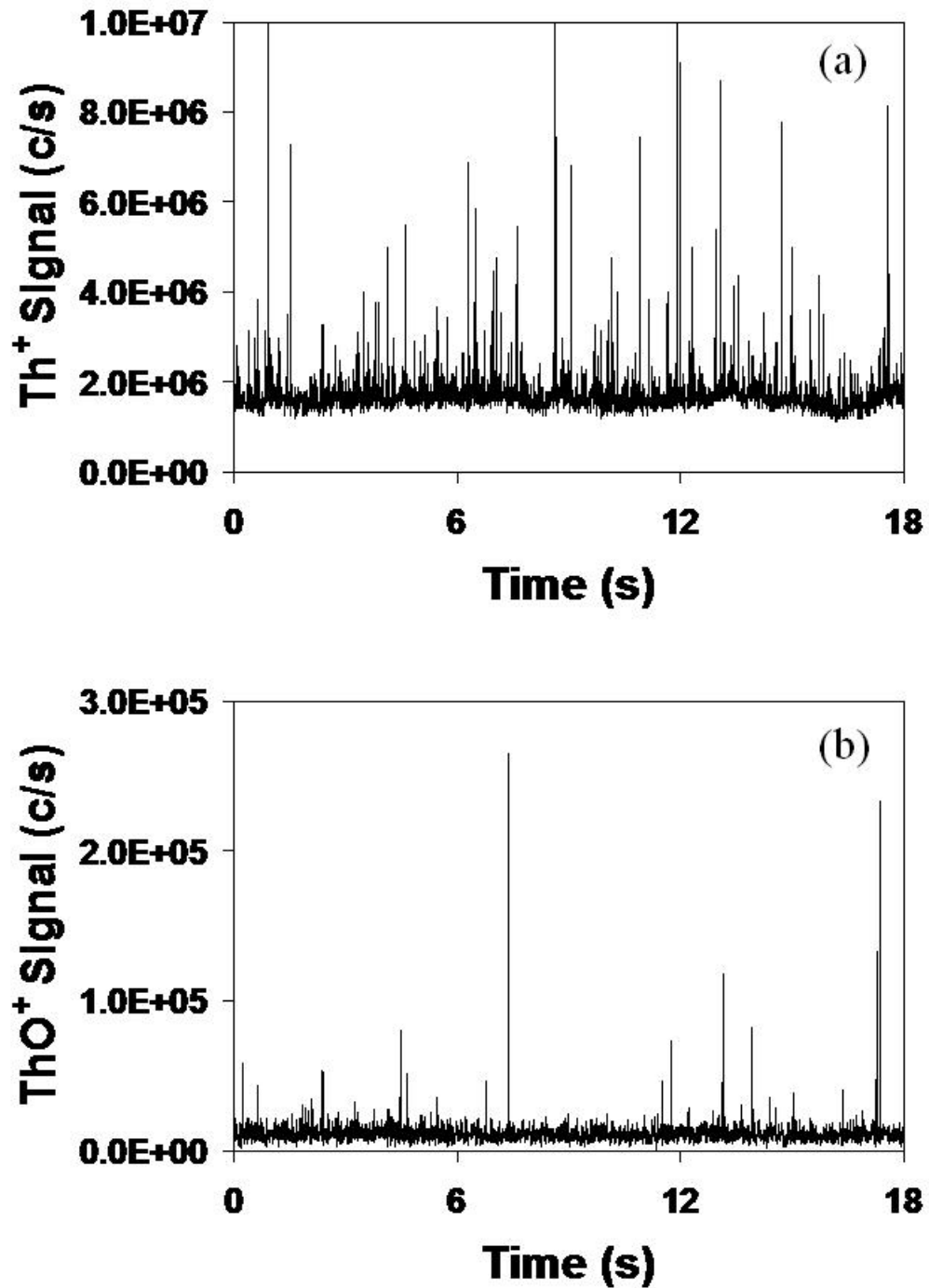
Figure 4. Plots of signals for (a) Th^+ and (b) ThO^+ while ablating NIST 1648 urban pellet. These plots were measured in separate acquisitions with the magnetic sector ICP-MS.
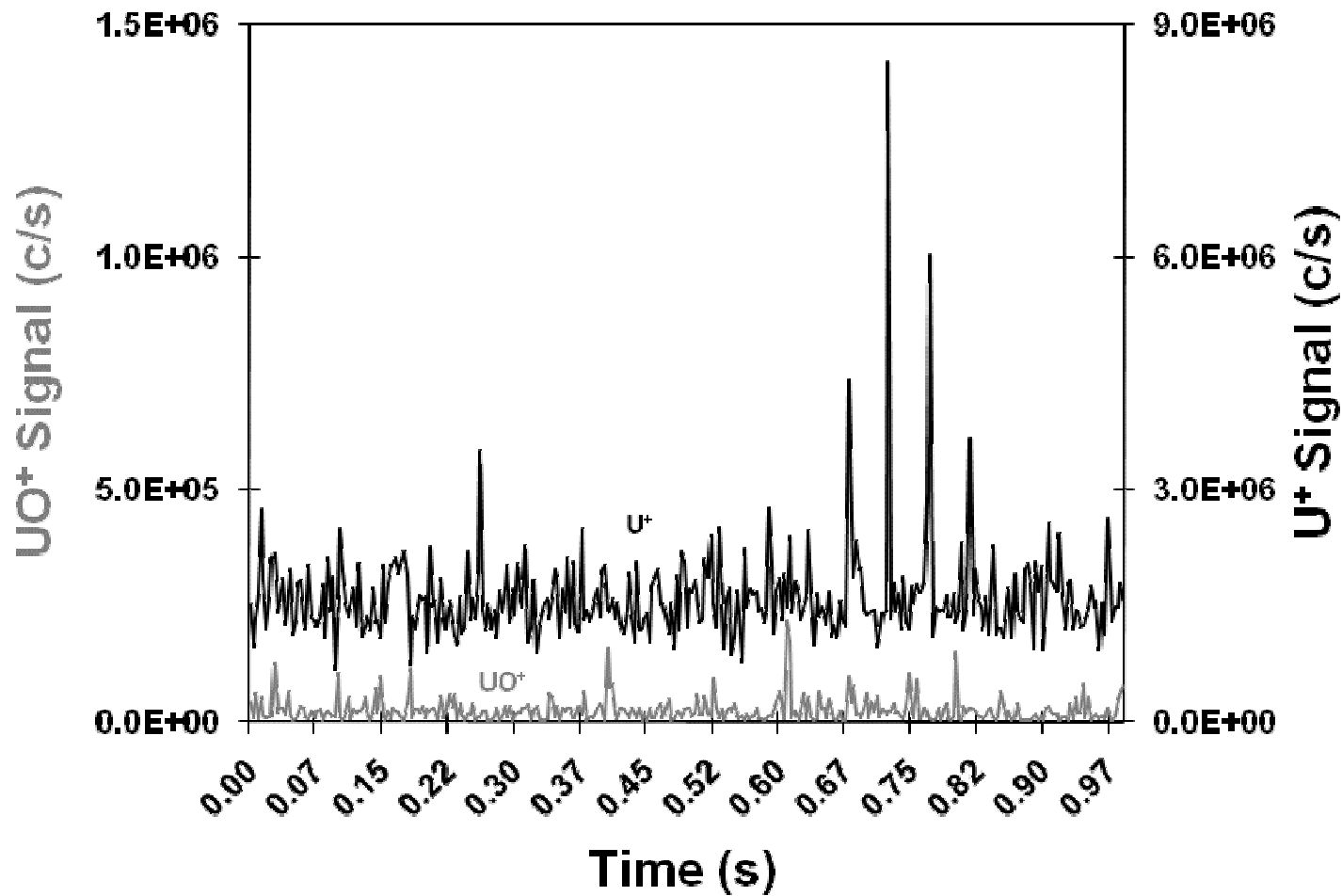
Figure 5. Signal as a function of time (a & b) and histogram plots (bin size = 0.01) (c & d) for $^{89}Y^+$ in NIST 1649 dust pellet prepared (a) and (c) without a binder, and (b) and (d) which were prepared with the use of a binder. Signal was measured with the magnetic sector ICP-MS.
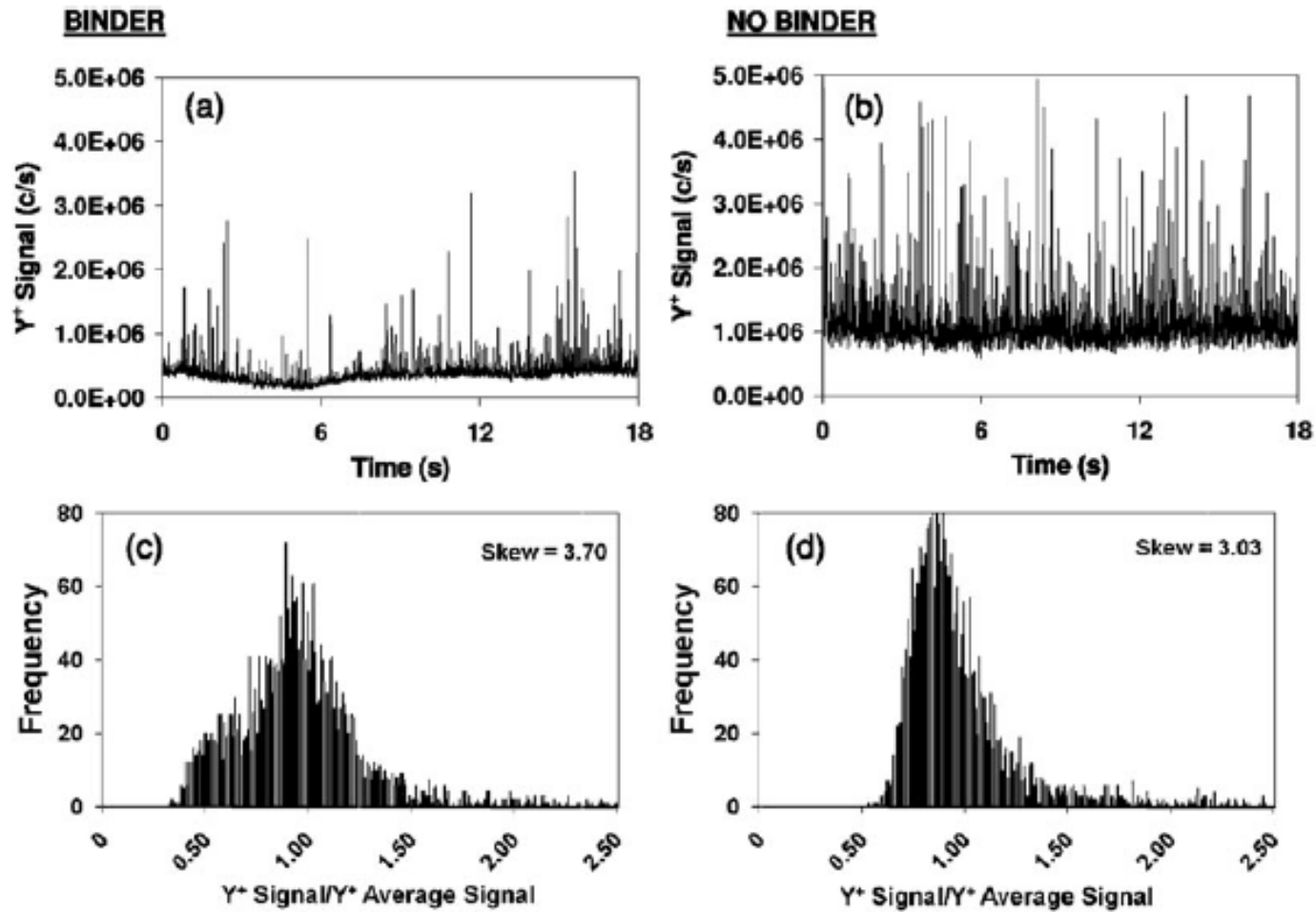
Figure 6. LA-ICP-TOF-MS measurement of $^{238}U^{16}O^+$ and $^{238}U^+$ signal intensity as a function of time with a time resolution of 3 ms per data point. Sample was NIST 1648, laser parameters were 20 Hz, 100 μm spot diameter, 50 μm/s raster rate.

CHAPTER 4 – PRELIMINARY STUDIES OF THE INFLUENCE OF AEROSOL PARTICLE SIZE AND SAMPLE GAS FLOW RATES ON ELEMENTAL RATIOS

D . C. Perdian, Daniel S. Zamzow, Stan S. Bajic, David P. Baldwin, and R. S. Houk*

ABSTRACT

Changes in sample gas flow rates as well as the size of the particle have a profound effect on the extent of inductively coupled plasma induced fractionation. Cu^+/Zn^+ signal ratios can decrease by a factor of 2 when either the sample gas flow rate is decreased or the size of the particle introduced into the plasma is increased. The difference in elemental ratios caused by changing sample gas flow rates can have a significant impact on analysis. Experimental data suggest that changes in signal ratios are a result of changes in plasma temperature, caused by changes in gas flow rates, which can influence the vaporization efficiency of the aerosol particles in the plasma.

*Corresponding Author

INTRODUCTION

Since the development of inductively coupled plasma atomic emission spectroscopy[1] (ICP-AES) and inductively coupled plasma mass spectrometry[2] (ICP-MS), the two techniques have become widely used for trace elemental analysis. The majority of analysis by ICP-MS is carried out via solution nebulization. Analysis of solid samples was by laser ablation (LA) introduced by Gray in 1985[3], but has not gained the volume of usage as the solution nebulization counterpart, even though it has many advantages. One of the biggest advantages of the LA-ICP-MS technique is that little or no sample preparation is required. LA can be used to precisely determine the isotopic abundances of solid samples which is very useful for geochemical research and analysis.[4] The use of LA-ICP-MS to determine a trace elemental fingerprint of samples has also been used for a variety of forensic evidence applications.[5, 6]

Isotopic and qualitative analysis by LA-ICP-MS is often a straightforward technique, as long as interference ions are identified or removed. Collision cells are methods that remove polyatomic ion interferences before mass analysis.[7] The use of high resolution mass spectrometers enables the distinction between the analyte ion of interest and polyatomic and/or isotopic interferences.[8] Accurate quantification of elements in solid samples using LA-ICP-MS, however, is more troublesome due to fractionation effects.[9] Fractionation effects, or the difference in analyte levels in the sample compared analyte ratios measured can be induced by the laser ablation event and the ICP. Fractionation effects can also cause deviations in transient signal levels. Laser ablation induced fractionation effects are caused by the preferential vaporization of volatile elements if the laser ablation event causes heating of the sample. ICP-induced fractionation is caused when LA generated particles are not

completely vaporized and atomized by the plasma. If a particle is not completely vaporized, volatile elements can preferentially vaporize and cause a higher signal when compared to more refractory elements. It has even been reported that the measured isotopic abundance of an element can deviate because of fractionation effects.[10]

Many factors of the laser ablation process such as wavelength[11-13], pulsewidth[14-16], and transport gas[17] can cause LA-induced fractionation and aerosol particles that are too large to be completely vaporized in the plasma which can cause ICP-induced fractionation[18, 19]. One such factor is incomplete vaporization of large aerosol particles in the ICP. Aeschilman et al. showed photographic evidence that intact aerosol particles can survive through the entire length of the plasma.[20] We have recently shown that particles that are not completely vaporized can cause large positive spikes in signal due to a large excess of ions surrounding the particle. It can be assumed that the large excess of ions may not be at a stoichiometric ratio representative of the sample due to preferential vaporization of more volatile elements. Because the spikes in signal occur very fast and occur randomly, valid elemental ratios are difficult to measure using scanning MS devices.

One such experimental factor that can cause very different signal levels and signal ratios is gas flow rate. The sample gas flow rate can often have the most profound effect on instrument tuning and often has the largest change from one day to the next of any tuning parameter. Changing the sample gas flow rate also may change the transport efficiency of aerosol particles created from the laser ablation. The sample gas flow rate also affects the position of analyte signal intensities in the plasma and changes the position of maximum analyte ion concentration within the plasma relative to the sampling cone of the mass

spectrometer which extracts the ions for mass analysis.[21] Variations in sample gas flow rate also affect the plasma temperature which can in turn cause changes in vaporization efficiency and subsequent ion signal.[22, 23] Internal and external calibration methods usually account for these phenomena for solution nebulization ICP-MS experiments.

A variety of quantification strategies have been developed for LA-ICP-MS experiments. Isotope dilution methods have been used for crude oil samples[24] and soil samples[25]. However isotope dilution methods are not amendable for many types of samples and it is only applicable for elements with multiple stable isotopes. There have been several successful experiments that used solution calibration techniques for quantification of elements analyzed by LA-ICP-MS.[26, 27] These methods, however, cannot account for fractionation that occurs as a result of the laser ablation event. Research focused on determining ways to minimize or eliminate fractionation effects completely will improve the success of quantitative analysis by LA-ICP-MS.

Copper to zinc ratios have been studied in the past because of their differences in volatility. Cu/Zn ratios have been shown to be different as aerosol particle size increases.[16, 28] The Cu/Zn ratios is also affected by vaporization efficiencies in the plasma.[28] The Cu/Zn ratios measured by LA-ICP-MS also have a dependence on the laser pulse width used[16, 29], and the bulk Cu/Zn ratio of the original sample[29].

This paper will describe experiments that show that the sample gas flow rate can have a profound effect on signal ratios. This effect is worse as the size of aerosol particles increase. Agglomerations of small particles most likely also cause this problem as well. This effect is most likely caused by plasma temperature changes or changes to the sampling position

incurred by the increasing or decreasing the sample gas flow rate. This experimental observation is often overlooked when discussing ICP-induced fractionation, but must be addressed if fractionation effects are to be overcome.

EXPERIMENTAL SECTION

Experimental Setup – The experimental setup for the first preliminary experiment is a typical LA-ICP-MS setup, i.e., a laser ablation system directly coupled the torch of an ICP-MS device with transport tubing. The second experimental setup used for LA experiments is shown (Fig.1), and is slightly more complex. The carrier gas which was argon was varied from 0.9 to 1.2 L min^{-1} in 0.1 L min^{-1} increments. To be able to vary the carrier gas flow rate while maintaining a constant plasma sample gas flow rate (and vice-versa), a second flow of argon, described as additional gas, is added after the laser ablation cell via a Y-shaped intersection. The polydisperse aerosol particles are transported from the ablation cell to the differential mobility analyzer (DMA), where particle sizes are filtered by their differential mobility. After the aerosol particles exit the DMA they are split to a condensation particle counter and the ICP-MS via a second Y-shaped intersection. The CPC accepts a constant 0.3 L min^{-1} argon flow to enter the device, which is regulated a pressure modulator. The flow rate that enters the ICP-MS as sample gas flow rate is then carrier gas flow rate + additional gas flow rate – 0.3 L min^{-1}. All experimental devices are described in more detail below.

Samples - National Institute of Standards and Technology (NIST) standard reference material (NIST C1102 brass, Gaithersburg, MD, USA) was used for all laser ablation

experiments. A standard solution of 1% $HNO_{3(aq)}$ containing 10 ppb copper and zinc was used for the solution nebulization experiments (Fig 4).

ICP-MS Device – The experiments were done with a magnetic sector instrument (Element 1, Thermo Finnigan, Bremen, Germany). The instrument was tuned for maximum sensitivity and stability. All instrumental conditions were kept constant, except of course the sample gas flow rate. Auxiliary gas flow rates and outer gas-flow rates were typically set between 0.90 to 0.95 L min^{-1} and 14 to 15 L min^{-1}, respectively. The instrument has shielded load coil which grounded. The sampling cone of the mass spectrometer is 12 mm from the load coil. The instrument acquired data in low resolution mode (m/Δm ~ 300) for all experiments.

Laser Ablation System - A Q-switched Nd:YAG laser (LSX 500, energy 9 mJ, pulse width ~ 5 ns, CETAC Technologies, Omaha, NE, USA), quadrupled to a wavelength of 266 nm, was used for these experiments. The LSX 500 can be operated at varying laser spot sizes by controlling the diameter of an internal aperture. The laser was set to a repetition rate of 10 Hz with a spot size of 100 μm diameter. The ablation cell rests on a translation stage, which controls the ablation location, raster rate, and raster pattern.   The laser-raster rate was set to 100 μm/s.

Differential Mobility Separation - A differential mobility analyzer (DMA) was employed (TSI Model 3080L DMA, TSI Inc, Shoreview, MN, USA) to separated particles based on electrical mobility, as described in detail elsewhere.[30] Briefly, the polydisperse aerosol

created from the laser-ablation process is sent through a bipolar discharger, which imparts a neutral equilibrium distribution of positive, negative, and neutral charges on the aerosol particles. The aerosol then passes through a differential mobility analyzer, which only allows particles with a specified electrical mobility to pass out to the plasma.

The DMA is said to transmit size values selectable from 1 nm to 1 μm. Under typical conditions the particle-size bandpass window is said to be 5% at small sizes and increases to 10% at larger particle sizes. For the experiments described in this work, the DMA scanned aerosol particle size from 16 nm to 400 nm during a 3 minute run. The DMA aerosol separation was corrected for the use of argon as the carrier gas, rather than air with which it was originally calibrated. This was done by changing the DMA default values for air to the values of argon gas viscosity, 2.26 x10^{05} kg / (m*s), and mean free path, 7.10 x10^{-8} m. The difference between the sheath gas flow settings for the DMA and the actual argon flow was measured for argon by a Gilian® Gilibrator-2 Calibration System (Sensidyne, Clear Water, FL, USA), and adjusted accordingly.

Condensation Particle Counter – A condensation particle counter (CPC) was employed (TSI Model 3080L DMA, TSI Inc, Shoreview, MN, USA) to monitor the number of aerosol particles exiting the laser ablation cell. The CPC is also able to determine the mass aerosol particles exiting the laser ablation cell. The CPC uses butanol as the working fluid. The operation and mechanism of detection of a CPC has described previously.[31, 32] Briefly, the CPC used butanol vapor to enlarge the aerosol particles size so that they can be measured

using optical scattering methods. The CPC was set to accept an aerosol gas flow rate of 0.3 L min^{-1} to enter the device.

Solution Nebulization – A PFA low flow nebulizer (ESI Inc. Omaha, NE USA) with an uptake rate of 100 µL/min was used for the solution nebulization experiment. A Teflon double pass Scott-type spray chamber was used to remove solvent before introduction into the plasma.

RESULTS AND DISCUSSION

Changing the flow rate of sample/carrier gas in a LA-ICP-MS experiment affects many parameters that determine the quality of the analysis. Altering the flow of the carrier gas in the ablation cell can affect the composition and transport efficiency of the laser ablated aerosol. Changing the sample gas flow rate effectively changes the analyte ionization region with respect to position of the mass spectrometers sampling cone. Changing the sample gas flow also alters the plasma temperature at the sampling cone position which is an important parameter affecting vaporization efficiency of the aerosol particles. All of these factors affect the signal levels measured.

The focus of these experiments is to document the trends of Cu^+/Zn^+ ratios as a function of carrier gas and sample gas flow rates. The results discussed here to do not try to determine the correct ratio of Cu^+/Zn^+ ratios as this number is affected by sampling position, ionization energies, mass bias factors, and differential atomization efficiencies.

Preliminary Experiments of Sample Gas Flow Rate

Changing the sample gas flow rate also changes the relative signal levels measured for different analytes. As a preliminary measure of this phenomenon, an experiment using a standard LA-ICP-MS experiment (LA System and ICP-MS Only) are used to measure the signal ratios of ^{65}Cu and ^{66}Zn (Fig 2). These ratios reflect raw signal levels only, and are not corrected for ionization efficiency, isotopic abundance, or certified concentration. As the carrier/sample gas flow is increased from 1.0 to 1.2 L min^{-1} the $^{65}Cu/^{66}Zn$ signal levels decrease by a factor of 1.7. This change in signal ratio can have a profound impact on the quality of analytical data if not taken into consideration. The cause of signal ratio deviation can be from increased carrier gas flow in the ablation cell, the change in relative sampling position of the plasma, or the changes of the plasma conditions.

Effect of Carrier Gas Flow in the Ablation Cell

In order to determine how much the signal ratio deviation is affected by changing the flow rate through the ablation cell, the $^{65}Cu^+/^{66}Zn^+$ signal ratio was measured while the carrier gas flow rate was increased in 0.1 L min^{-1} increments and the additional argon flow rate was decreased in 0.1 L min^{-1} increments so that the final sample gas flow reaching the plasma remained constant (Fig 3a). The ratios reported are the average of two separate experiments. To determine the impact of the aerosol particle size, the DMA scanned the aerosol particles sizes created from the laser ablation event. It was found that changing the carrier gas flow rate while keeping the final sample gas flow rate constant had little to effect on $^{65}Cu^+/^{66}Zn^+$ signal levels.

Effect of Sample Gas Flow through the Plasma

To determine the amount of impact of plasma temperature variations from sample gas flow rates has on the changing $^{65}Cu^+/^{66}Zn^+$ signal levels, the carrier gas flow rate was held constant while the additional gas flow rate was increased by 0.1 L min^{-1} increments (Fig 3b). Once again, the ratios reported are the average of two separate experiments. To determine the impact of the aerosol particle size, the DMA scanned the aerosol particles sizes created from the laser ablation event. The $^{65}Cu^+/^{66}Zn^+$ signal levels steadily decrease as the sample gas flow rate is increased, just as happened in the preliminary experiment (Fig 1). The magnitude of signal ratio reduction also increased as the aerosol particle size increases. At very low aerosol particle sizes < 50 nm, the $^{65}Cu^+/^{66}Zn^+$ signal levels are very similar. Whereas at aerosol particle sizes > 300 nm the $^{65}Cu^+/^{66}Zn^+$ signal levels are the most severely deviated as a function of sample gas flow rate.

The signal levels for $^{65}Cu^+$ and ^{66}Zn at several particle sizes from Figure 3a and 3b are listed in Tables 1 and 2, respectively. The signal levels increase as gas flow rates are increased for both experiments. The increase in signal as the sample gas flow rate is increased (Table 2) is much more pronounced than when the carrier gas flow rate is increased (Table 1). The increase in signal as the carrier gas is increased is caused by more efficient removal of aerosol particles from the ablation cell. This assumption is only valid for smaller particles (50 and 100 nm) as the signal is not altered significantly at a DMA setting of 300 nm. Larger particles transportation is not affected by carrier gas flow rates as much as smaller particles. The increase in signal seen when the final sample gas flow rate is increased (constant carrier gas flow rate) is caused by changing the plasma properties (i.e., plasma

temperature and relative sampling position. Changes in plasma properties have large affect on signal levels. These changes in plasma properties are also what cause the changes in $^{65}Cu^+/^{66}Zn^+$ signal ratio, which is not seen when changing only the carrier gas flow rate.

Effect of Relative Sampling Position

To determine if the signal ratios deviation is caused by the plasma temperature changes and not instead caused by changing the relative sampling position, a simple solution nebulization experiment was carried out (Fig 4). As the sample gas flow rate is increased the plasma shape and characteristics are altered. The position in which the maximum amount of analyte atoms are ionized is moved relative to the position which the mass spectrometer sampling cone extracts ions from the ICP. For solution nebulization, the $^{65}Cu^+/^{66}Zn^+$ signal ratio increases as the sample gas flow rate is increased. Because it is well known that copper and zinc are efficiently vaporized, atomized, and ionized during a solution nebulization experiment it can be inferred that the change in $^{65}Cu^+/^{66}Zn^+$ signal ratio is cause by the change in relative sampling position. Because the $^{65}Cu^+/^{66}Zn^+$ signal ratio increases as the sample gas flow rate increase, which is the inverse of what occurred during the laser ablation experiment (Fig 3b), it can be inferred that the plasma conditions are the dominant factor causing the change in $^{65}Cu^+/^{66}Zn^+$ signal levels. The raw signal levels of $^{65}Cu^+$ and ^{66}Zn as a function of sample gas flow rate are reported in Table 3. It is interesting to note that the maximum signal for $^{65}Cu^+$ is not achieved until a sample gas flow rate of 1.2 L min^{-1}. The $^{66}Zn^+$ maximum signal is achieved at a sample gas flow rate of 1.1 L min^{-1} showing that the relative sampling position that achieves maximum ion signal may be different for these two ions.

Monitoring of Aerosol Particle Composition with CPC

To ensure that aerosol composition (size, mass, etc.) was not the cause of the observed signal ratio change, a CPC monitored the number of LA-produced aerosol during the LA experiments described above. As described in the experimental section a flow rate of 0.3 L min^{-1} was split from the transport line after the DMA and was sent to the CPC. The remainder of the aerosol flow rate was delivered to the plasma.

The number of particles and the mass associated with the particles was measured by the CPC as a function of aerosol particle size scanned by the DMA (Fig 5). The number of particles cm^{-3} as a function of aerosol particle size is measured when both the carrier gas flow is varied (Fig 5a), and when the sample gas flow rate is varied (Fig 5b). The mass of the aerosol particles (μg cm^{-3}) is also measured as a function of aerosol particle size when carrier gas flow is varied (Fig 5c), and when the sample gas flow rate is varied (Fig 5d). Except for Figure 5a, where there is a relationship between particle density and carrier gas flow, there is no direct or inverse relationship that can explain the change in $^{65}Cu^+/^{66}Zn^+$ signal ratios from an aerosol particle composition point of view. Since there was not a change in $^{65}Cu^+/^{66}Zn^+$ signal ratio while the carrier gas flow rate was increased (Fig 3a) the increase of number of particles cm^{-3} as the carrier gas flow increases is not causing any of the experimental findings that we observe. All the CPC measurements (Fig 5a-d) correspond to the exact same laser ablation experiments which produced the results displayed in Figures 3a and 3b.

CONCLUSIONS

It was found that increasing the sample gas flow rate the causes a decrease in the signal ratio for $^{65}Cu^+/^{66}Zn^+$. Experimental evidence shows that the overriding factor that causes this phenomenon is a change in plasma conditions. This phenomenon is exacerbated as the size of aerosol particles entering the plasma is increased. Future experiments will be performed to study how much the sample gas flow rates and plasma temperature affects other elemental ratios.

ACKNOWLEDGEMENTS

REFERENCES

1.   R. H. Scott, V. A. Fassel, R. N. Kniseley and D. E. Nixon, *Analytical Chemistry*, 1974, **46**, 75-80.

2.   R. S. Houk, V. A. Fassel, G. D. Flesch, H. J. Svec, A. L. Gray and C. E. Taylor, *Analytical Chemistry*, 1980, **52**, 2283-2289.

3.   A. L. Gray, *Analyst*, 1985, **110**, 551 - 556.

4.   R. A. Cox and D. H. C. Wilton, *Chemical Geology*, 2006, **235**, 21-32.

5.   S. J. Bajic, D. B. Aeschliman, N. J. Saetveit, D. P. Baldwin, and R. S. Houk, *Journal of Forensic Sciences*, 2005, **50**, 1123-1127.

6.   S. Berends-Montero, W. Wiarda, P. d. Joode and G. v. d. Peijl, *Journal of Analytical Atomic Spectrometry*, 2006, **21**, 1185-1193.

7.   S. D. Tanner, V. I. Baranov and D. R. Bandura, *Spectrochimica Acta Part B: Atomic Spectroscopy*, 2002, **57**, 1361-1452.

8.   J. W. Ferguson and R. S. Houk, *Spectrochimica Acta Part B: Atomic Spectroscopy*, 2006, **61**, 905-915.

9.   B. Hattendorf, C. Latkoczy and D. Guenther, *Analytical Chemistry*, 2003, **75**, 341 A-347 A.

10.   H.-R. Kuhn, N. J. Pearson and S. E. Jackson, *Journal of Analytical Atomic Spectrometry*, 2007, **22**, 547-552.

11.   J. S. Becker and D. Tenzler, *Fresenius' Journal of Analytical Chemistry*, 2001, **370**, 637-640.

12. R. E. Russo, X. L. Mao, O. V. Borisov and H. Liu, *Journal of Analytical Atomic Spectrometry*, 2000, **15**, 1115-1120.

13. M. Guillong, I. Horn and D. Gunther, *Journal of Analytical Atomic Spectrometry*, 2003, **18**, 1224-1230.

14. J. Pisonero, Detlef Günther, *Mass Spectrometry Reviews*, 2008, **27**, 609-623.

15. F. Poitrasson, X. Mao, S. S. Mao, R. Freydier and R. E. Russo, *Analytical Chemistry*, 2003, **75**, 6184-6190.

16. N. J. Saetveit, S. J. Bajic, D. P. Baldwin and R. S. Houk, *Journal of Analytical Atomic Spectrometry*, 2008, **23**, 54-61.

17. I. Horn and D. Günther, *Applied Surface Science*, 2003, **207**, 144-157.

18. D. C. Perdian, S. J. Bajic, D. P. Baldwin and R. S. Houk, *Journal of Analytical Atomic Spectrometry*, 2008, **23**, 325-335.

19. D. C. Perdian, S. J. Bajic, D. P. Baldwin and R. S. Houk, *Journal of Analytical Atomic Spectrometry*, 2008, **23**, 336-341.

20. D. B. Aeschliman, S. J. Bajic, D. P. Baldwin and R. S. Houk, *Journal of Analytical Atomic Spectrometry*, 2003, **18**, 1008-1014.

21. A. E. Holliday and D. Beauchemin, *Spectrochimica Acta Part B: Atomic Spectroscopy*, 2004, **59**, 291-311.

22. J. W. Olesik, *Applied Spectroscopy*, 1997, **51**, 158A-175A.

23. S. E. Hobbs and J. W. Olesik, *Analytical Chemistry*, 1992, **64**, 274-283.

24. J. Heilmann, S. F. Boulyga and K. G. Heumann, *Journal of Analytical Atomic Spectrometry*, 2009, **24**, 385-390.

25. S. Boulyga, M. Tibi and K. Heumann, *Analytical and Bioanalytical Chemistry*, 2004, **378**, 342-347.

26. J. J. Leach, L. A. Allen, D. B. Aeschliman and R. S. Houk, *Analytical Chemistry*, 1999, **71**, 440-445.

27. S. F. Boulyga, Carola Pickhardt, and J. Sabine Becker, *Atomic Spectroscopy*, 2004, **25**, 53-63.

28. H.-R. Kuhn and D. Gunther, *Analytical Chemistry*, 2003, **75**, 747.

29. C. Liu, X. L. Mao, S. S. Mao, X. Zeng, R. Greif and R. E. Russo, *Analytical Chemistry*, 2004, **76**, 379-383.

30. E. O. Knutson and K. T. Whitby, *Journal of Aerosol Science*, 1975, **6**, 443-451.

31. J. C. Wilson, E. D. Blackshear and J. H. Hyun, *Journal of Aerosol Science*, 1983, **14**, 387-391.

32. P. H. McMurry, *Aerosol Science and Technology*, 2000, **33**, 297 - 322.

Table 1. $^{65}Cu^+$ and $^{66}Zn^+$ signal levels, from Figure 3a, as a function of carrier gas flow rates (constant sample gas flow rates) at different particle sizes.

Gas Flow Rate (L min^{-1})		Particle Size (nm)		
Carrier	Additional	50	150	300
0.9	0.4	16/3.0	65/12	39/6.3
1.0	0.3	20/3.9	63/13	32/6.5
1.1	0.2	20/3.4	78/13	31/6.4
1.2	0.1	39/7.9	82/15	35/6.7
				$^{65}Cu^+$/$^{66}Zn^+$ Signal Levels (x10^4 cps)

Table 2. $^{65}Cu^+$ and $^{66}Zn^+$ signal levels, from Figure 3b, as a function of final sample gas flow rates (constant carrier gas flow rates) at different particle sizes.

Gas Flow Rate (L min^{-1})		Particle Size (nm)		
Carrier	Additional	50	150	300
0.9	0.2	9.5/1.5	23/3.6	11/1.6
0.9	0.3	11 /1.6	36/5.7	24/3.7
0.9	0.4	16/3.0	65/12	39/6.3
0.9	0.5	40/8.9	180/42	72/24
				$^{65}Cu/^{66}Zn$ Signal Levels (x10^4 cps)

Table 3. $^{65}Cu^+$ and $^{66}Zn^+$ signal levels, from Figure 4, as a function of sample gas flow rates for a solution nebulization experiment.

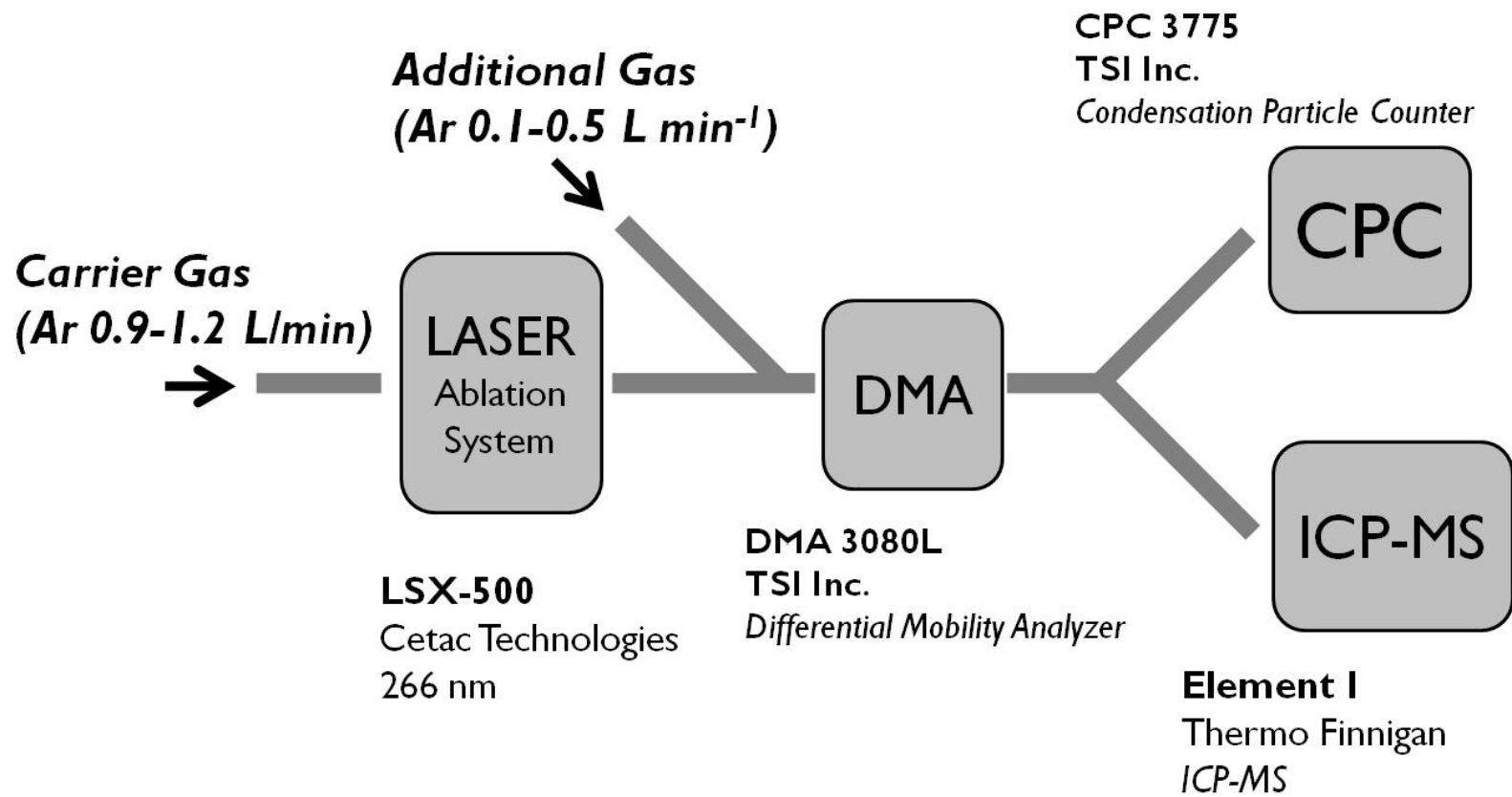| Sample Gas Flow Rate (L min^{-1})	Signal Level (x10^4 cps)	
	$^{65}Cu^+$	$^{66}Zn^+$
0.9	2.2	0.85
1.0	9.4	3.0
1.1	33	9.0
1.2	78	1.8

Figure 1. Experimental setup used to obtain the experimental results in Figure 3 and Figure 5.
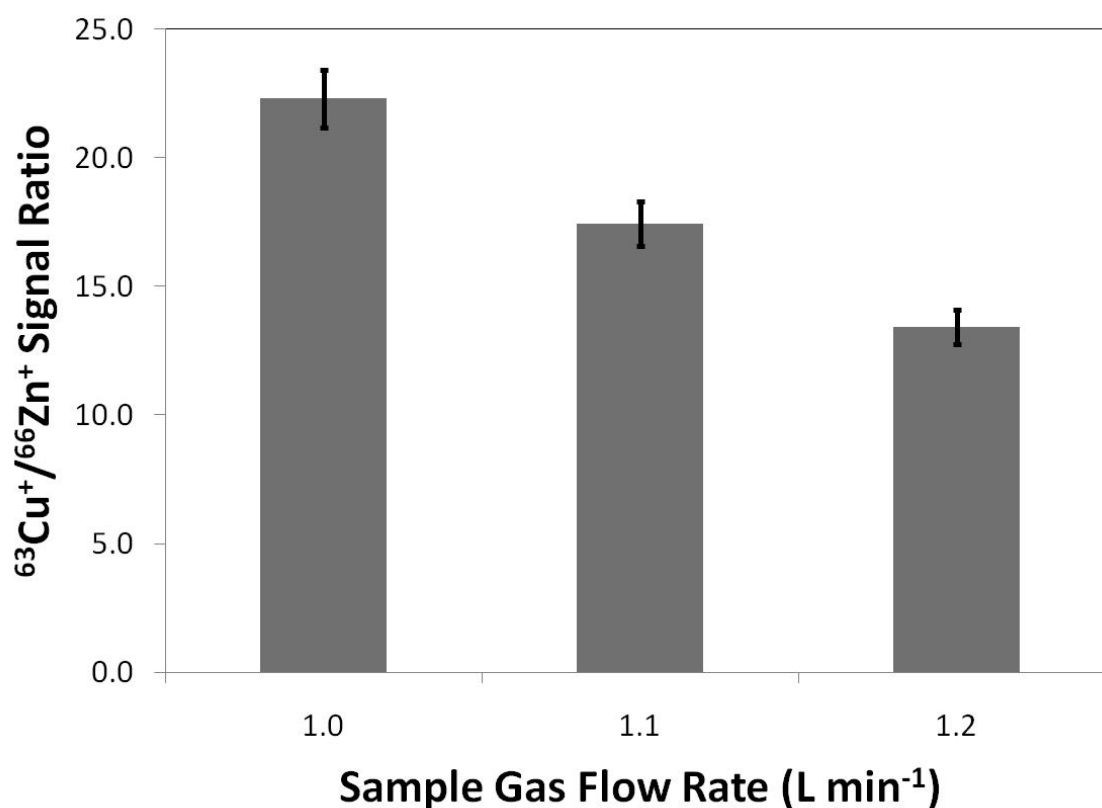
Figure 2. $^{63}Cu^+/^{66}Zn^+$ signal ratio as a function of sample gas flow rate. No DMA or CPC was used for this experiment. The signal levels for $^{63}Cu^+$ steadily increase from $5.5x10^6$ to $1.6x10^7$ and $4.0x10^7$ cps for sample flow rates of 1.0, 1.1, and 1.2 L min-1, respectively. The signal levels for $^{66}Zn^+$ steadily increase from $2.3x10^5$ to $8.6x10^5$ and $2.9x10^6$ cps for sample flow rates of 1.0, 1.1, and 1.2 L min-1, respectively.
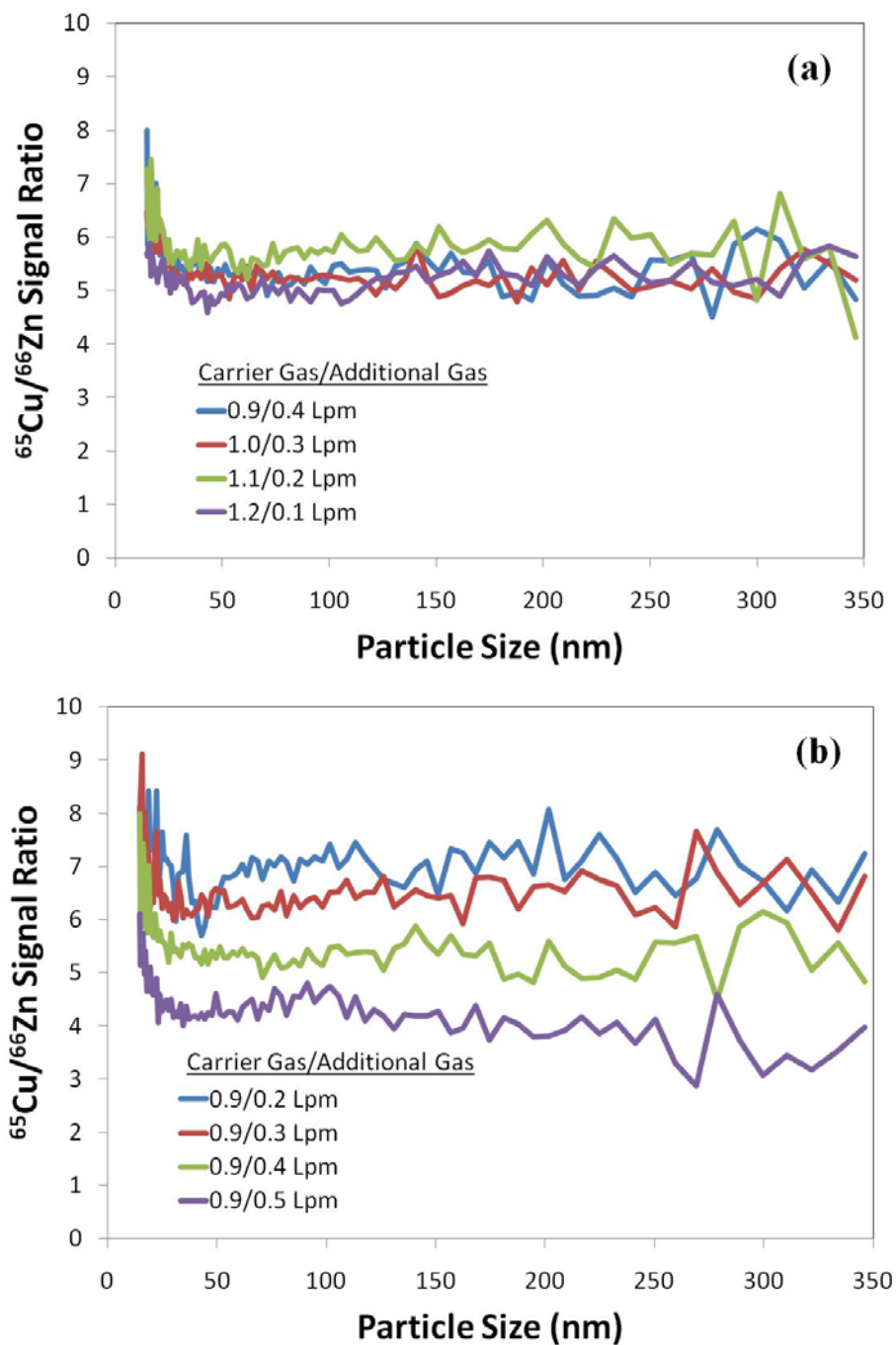
Figure 3. $^{65}Cu/^{66}Zn$ signal ratios as a function of particle size selected by the DMA for (a)varying carrier gas flow rate through the laser ablation cell (0.9-1.2 L min^{-1}) but keeping the final sample gas flow rate constant (1.0 L min^{-1}), (b) varying the final sample gas flow rate (0.8-1.1 L min^{-1}) while keeping the carrier gas flow through the cell constant (0.9 L min^{-1}. All final volumes are reduced by 0.3 L min^{-1} by sending that amount of gas flow to the CPC.
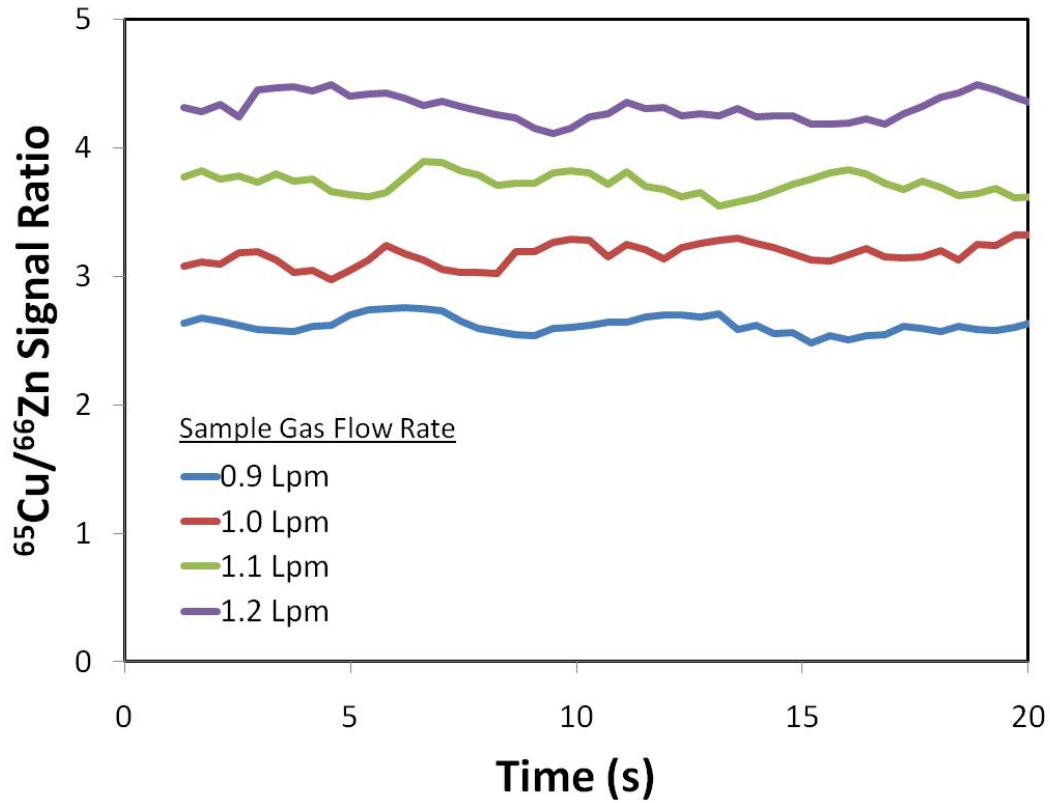
Figure 4. ^{65}Cu/^{66}Zn signal ratios as a function of time while nebulizing a 10 ppb concentrated solution of copper and zinc. The solution was self aspirated at flow rate of ~100 µL min^{-1}. The solution was nebulized into a Scott-type double pass spray chamber.

Figure 5. Measurement of number of particles (a) and (b) (Y-Axis is number of particles per unit volume), and the calculated mass associated with those particles (c) and (d) (Y-axis is µg of particles per unit volume). Carrier gas is varied for measurements taken (a) and (c), while the final sample gas flow rate is changed for (b) and (d). Gas flow rates listed in key are carrier gas flow rates/additional gas flow rates.

CHAPTER 5 – ATMOSPHERIC PRESSURE LASER DESORPTION/IONIZATION OF PLANT METABOLITES AND PLANT TISSUE USING COLLOIDAL GRAPHITE

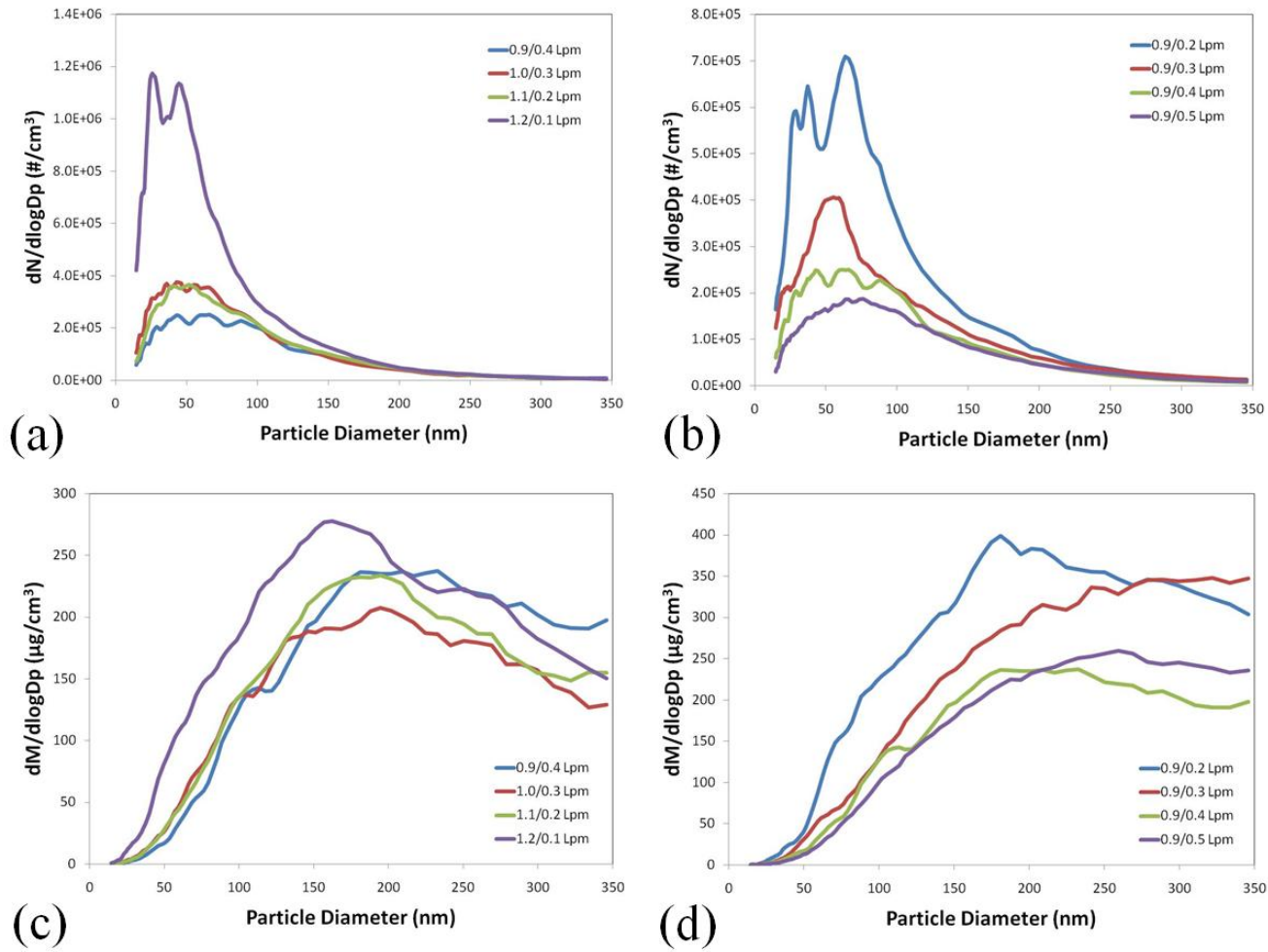A paper to be submitted to the *Journal of the American Society of Mass Spectrometry*

D. C. Perdian, Gregg M. Schieffer, and R. S. Houk*

ABSTRACT

Colloidal graphite works as a suitable matrix for atmospheric pressure laser desorption/ionization mass spectrometry. This technique effectively produces intact molecular ions from a wide range of small molecule plant metabolites particularly anthocyanins, fatty acids, lipids, glycerides, and ceramides. Experiments using colloidal graphite for laser desorption/ionization mass spectrometric analysis has advantages over the use of traditional organic acid matrices for the analysis of small molecules. Specifically colloidal graphite is able to ionize small hydrophobic molecules more efficiently, and has a much cleaner background spectrum especially in negative ion mode. This technique proves to be a somewhat softer ionization technique at atmospheric pressure than at lower pressures while maintaining comparable signal-to-noise ratios. This technique is shown to be sensitive enough to analyze *Arabidopsis Thaliana* leaf and flower petal tissues for plant metabolites *in situ*.

*Corresponding Author

INTRODUCTION

Since its development[1, 2], matrix-assisted laser desorption/ionization (MALDI) has become an invaluable tool for the analysis of a large number of biological molecules including proteins[3-5], peptides[4, 6], oligonucleotides[7] and oligosaccharides[8, 9]. MALDI-MS techniques have been applied to study numerous biological functions including protein-protein interactions[10], and bio-marker discovery[11]. Due to the fact that MALDI is able to directly analyze biological tissues, it has become a popular method for imaging mass spectrometry (IMS).[12-14] For the spatial imaging analysis a MALDI matrix can be sprayed onto the tissue, a series of micro-droplets can be applied to the sample, or both methods can be employed on the same sample.[15]

The most popular matrices for MALDI experiments have been organic acid compounds, such as α-cyano-4-hydroxycinnamic acid, 2, 3-dihydroxybenzoic acid, as well as other organic acids.[16, 17] These organic acid matrices readily generate singly-charged protein and peptide ions, but like any analytical technique have limitations analyzing certain analytes. Efficient ionization of the analyte in MALDI requires that the analyte and matrix co-crystallize. The amount of co-crystallization varies with the hydrophobicity of the analyte molecules, with the more hydrophilic molecules co-crystallizing better. A variety of sample preparation methods have been developed to increase the successfulness of MALDI methods for hydrophobic proteins, such as varying temperature during the co-crystallization step[18] and using organic solvent mixtures to facilitate the analyte/matrix co-crystallization[19, 20]. The crystalline structure of the organic acids also causes spatial inhomogeneity for a given sample.[21] For imaging experiments, spatial homogeneity is extremely important for quality

mass spectral images. The use of organic acids as matrices also generates many background ions at low m/z values which can create a problem when trying to detect small analyte molecules.

A variety of methods have been developed to overcome these limitations. Room temperature molten salts, or ionic liquids, have been used as matrices and provide more homogeneous signal compared to traditional MALDI matrices.[22] Ionic liquids have also been used to improve the ionization efficiencies of some molecules, such as glycosaminoglycan disaccharides.[23] Atmospheric pressure infrared MALDI using concomitant water as a matrix has been used to image plant metabolites.[24, 25] Using the native water as a matrix produces a cleaner background spectrum, as no additional matrix is required. A variety of nanomaterials have been used as alternate methods for MALDI experiments. Silver nanoparticles were used as a matrix in a surface-assisted laser desorption/ionization experiments to analyze estrogen molecules.[26] Colloidal Ag was used as a matrix for LDI-IMS experiments which monitored the spatial distribution of metabolites in *Arabidopsis Thaliana* plant tissue.[27] Gold nanoparticles have been used to analyze small bio-molecules using visible lasers.[28]

Graphite has been used in various forms as a pseudo matrix for LDI-MS experiments.[29-34] Sunner et al. used graphite for surface-assisted laser desorption ionization of peptides and proteins from liquid solutions.[29] Dale et al. used graphite/liquid mixtures to successfully ionize several types of molecules including proteins, peptides, polysaccharides, and polymers.[30] Graphite was incorporated into a thin layer chromatography (TLC) plate and used as matrix for LDI.[31] Graphite-assisted laser desorption/ionization (GALDI) was also used to study light-induced aging in tri-terpene dammar and mastic varnishes.[32] Low

molecular weight polymers were analyzed on a graphite plate by LDI-MS without the use of any additional matrices.[33] GALDI also effectively ionized fatty acid molecules from triglycerides, food, and phospholipids samples.[34]

Recently, the use of colloidal graphite has been used to analyze and image small molecules with the sample at intermediate pressures (~100-200 mTorr).[35, 36] Colloidal graphite ionized small hydrophobic analytes with a greater efficiency when compared to traditional organic acid MALDI matrices. It was shown previously that polar phospatidyl choline and sphingomyelins suppressed the signal of other less-polar lipids within a sample using MALDI-MS.[37] This was not the case using colloidal graphite LDI-MS. Colloidal graphite also provides a simple sample preparation procedure that provides very homogeneous sample coverage. This method of GALDI was able to successfully ionize a variety of compounds including: phospholipids, cerebrosides, phospatidylcholines, and sulfatides.[35] This method was also used to determine fatty acids, organic acids, flavonoids, and oligosaccharides.[36]   Cha et al. also used colloidal graphite to image plant metabolites *in situ* from the tissue of various parts of the *Arabidopsis Thaliana* plant.[38]

Presented in this paper are the first experiments showing the effectiveness of colloidal graphite LDI-MS at atmospheric pressure. The advantages and figures of merit of this technique described above are maintained the elevated pressure. Being able to perform IMS experiments using colloidal graphite at atmospheric pressure will offer the ability to achieve higher throughput as well as the possibility of performing molecular imaging on living tissues.

EXPERIMENTAL SECTION

Samples – Standards, MALDI matrices, and solvents used were purchased from Fisher Scientific (Fairlawn, NJ). Total brain lipid extract was purchased by Avanti Polar Lipids Inc. (Alabaster, AL) The colloidal graphite in 2-propanol (IPA) aerosol spray (Aerodag G®) was purchased from Acheson Colloids (Port Huron, MI). The *Arabidopsis Thaliana* wild type plant samples were provided by Dr. Basil Nikolau, Iowa State University, Ames, IA.

Sample Preparation – For the analysis of standards, 2 or 3 µL of standard solutions were pipetted onto the stainless steel sample plate and allowed to air dry. All sample loadings were 20 to 50 ng, except stearic acid in which 20 µg of the sample was deposited. The actual amount of analyte that is sampled by the laser is much less than that amount. Colloidal graphite in IPA was then sprayed on to the sample plates in three 5-second bursts from a distance of approximately 20 cm. The sprayed samples were air dried for 5 minutes.

Plant tissue samples were attached the stainless steel sample plates via conducting double sided tape. Colloidal graphite in IPA was sprayed in the same manner as the standard samples, and allowed to dry for 5 minutes.

MALDI samples were prepared by making a 1:1 by volume analyte-to-matrix solution, and pipetting 3 µL of the 1:1 mixture onto the sample plate and allowed to air dry for 30 minutes. The 2, 3-dihydroxybenzoic acid (DHB) matrix solution was a saturated solution of DHB in 50/50% (% v/v) H_2O/acetonitrile with 0.1 % TFA (trifluoroacetic acid).

Laser – A solid state Nd:YAG laser (Cetac Technologies, Omaha, NE) quadrupled to a wavelength of 266 nm was used for these experiments. Other operating conditions of the laser are: 20 Hz, 1.9 mJ per pulse, spot size 200 μm diameter. The pulse energy was attenuated to approximately 200 μJ by reducing the flash lamp energy and placing neutral density filters (Thor Labs, Newton, NJ) in the path of the beam. The incident angle of the laser beam onto the sample was approximately 25º from the sample surface.

Mass Spectrometers - An LCQ Advantage 3D ion trap mass spectrometer (Thermo Finnigan, Bremen, Germany) was used for these experiments. The atmospheric pressure chemical ionization (APCI) source designed for use on the LCQ advantage was modified to hold a stainless steel sample plate. The sample plate was placed orthogonal to the MS heated capillary inlet at a distance of 4 mm. A high voltage of 200 to 4000 V was applied to the sample plate. The automatic gain control of the mass spectrometer was turned off; instead injection times of 100 to 250 ms were used.

To compare some figures of merit of this experimental procedure an LTQ linear ion trap with a vMALDI source (Thermo Finnigan, Bremen, Germany) was used to obtain the results for Fig 4b. The LTQ operates at an intermediate pressure of 170 mTorr and uses a N_2 laser (355 nm, 200 μJ/pulse, 20 Hz) for desorption and ionization. The use of LTQ vMALDI instrument for colloidal graphite for LDI-MS experiments has been described previously.[35, 36]

RESULTS AND DISCUSSION

Analysis of Standards – The analysis of standards was used for the initial determination of the effectiveness of colloidal graphite to assist the desorption and ionization of typical plant metabolite molecules at atmospheric pressure. LDI-MS using colloidal graphite can be used in both positive and negative modes. The mass spectra for molecules from ceramide (Fig 1a), phospatidyl cholines (Fig 1b), and glycerol (Fig 1c) molecular classes show mainly protonated molecular ions in positive mode. The mass spectra for molecules from the anthocyanin (Fig. 2a and 2b) and fatty acid (Fig. 2c) molecular classes show mainly deprotonated molecular ions in negative mode.

The anthocyanin isomers morin (Fig. 2a) and quercetin (Fig. 2b) were successfully distinguished from each other using tandem mass spectrometric techniques (Fig. 3). The diagnostic fragment ion for flavonoid molecules[39] is observed at m/z 151 both spectra. The diagnostic fragment for morin[39], m/z 149, and the diagnostic fragment ion for quercetin[39], m/z 179, are both observed from the respective parent ions. All spectra show reasonable signal to noise ratios. The peaks at m/z 675 (Fig. 1b) and m/z 373 (Fig. 1c) are from unknown contaminations of the standard samples.

The most prominent peaks in all mass spectra are the intact molecular ions, providing evidence that the use of colloidal graphite for AP-LDI-MS experiments is a soft ionization technique. The mass spectrum of 24:0 ceramide (Fig. 1a) does show a peak at m/z 633 which corresponds to the loss of H_2O fragment ion. However, when comparing the mass spectra of 24:0 ceramide taken at atmospheric pressure (Fig. 4a) to the mass spectra of the same molecule at a reduced pressure of 170 mTorr (Fig. 4b) the intact molecular ion is the most

prominent peak at atmospheric pressure and the loss of H_2O fragment ion is the most prominent peak at lower pressure. The same observations were seen when traditional MALDI experiments were first conducted at atmospheric pressure.[40]

The signal-to-noise ratios for mass spectra at intermediate pressure and atmospheric pressure show that a better S/N is achieved at intermediate pressure. This observation was also seen when traditional vacuum MALDI experiments were compared to AP-MALDI experiments.[41] It must be noted that the comparison of pressure regimes is on two separate mass spectrometers, and therefore not a completely ideal comparison. Improvements in S/N ratios at atmospheric pressure are planned in the future by employing a pulsed dynamic focusing ion extraction method.[42]

The advantages of using colloidal graphite over traditional MALDI matrices can be seen by comparing the mass spectra for a total brain lipid extract analyzed with colloidal graphite (Fig. 5a) and DHB (Fig. 5b). Many of the peaks of this complex mixture are not seen when using DHB as a matrix. This is especially apparent in the m/z range of 400 to 550, where most of the ions detected by colloidal graphite LDI-MS are not observed in the MALDI mass spectrum. The total brain lipid extract is approximately 16.7% phosphatidylethanolamine molecules, 10.6% phosphatidylserine molecules, 9.6% phosphatidylcholine molecules, 2.8% phosphatidic acid, 1.6% phosphatidylinositol molecules, and 58.7% other molecules. These hydrophobic molecules do not co-crystallize with the DHB matrix and therefore do not desorb and/or ionize as efficiently as the molecules do when analyzed with colloidal graphite. A similar effect was seen when using α-cyano-4-hydroxycinnamic acid as the MALDI matrix.

Analysis of Plant Tissue – Two different types of plant tissue were analyzed to determine if using colloidal graphite for LDI-MS experiments is sensitive enough for analysis of plant metabolites at atmospheric pressure. A leaf from an *Arabidopsis thaliana* wild type sample was analyzed and several peaks that correspond to fatty acid molecules from the cuticular wax are observed (Fig. 6). The analysis of a flower petal from the same Arabidopsis thaliana wild type sample displays several peaks that could correspond to mono-glycoside flavonoid molecules (Fig. 7a) as well as several di-glycoside flavonoid molecules (Fig. 7b). The molecular identification shown in the figures are based on matches to metabolite identification made by MS/MS methods in previous work.[27, 38]

CONCLUSIONS

The evidence provided in this paper shows that using colloidal graphite for LDI-MS at atmospheric pressure is sensitive enough to analyze plant metabolites *in situ* and raises the possibility of performing molecular imaging mass spectral analysis of plant tissues *in vivo*. Future work will involve employing pulse dynamic focusing ion extraction method[42] and/or a counter-current N_2 flow[43] to improve sensitivity. Incorporation of a software controlled translational stage to move the sample stage during mass analysis will provide the means for molecular imaging.

Technology for providing the *Arabidopsis thaliana* plant samples. We would also like to thank Sangwon Cha for advice on the use of colloidal graphite as a matrix. This work is supported by the Ames Laboratory U. S. Department of Energy, Office of Basic Energy Sciences. The Ames Laboratory is operated by Iowa State University of Science and Technology under DOE Contract #DE-AC02-07CH11358.

REFERENCES

1.   M. Karas, D. Bachmann and F. Hillenkamp, *Analytical Chemistry*, 1985, **57**, 2935-2939.

2.   K. Tanaka, Hiroaki Waki, Yutaka Ido Satoshi, Akita Yoshikazu, Yoshida Tamio, Yoshida T. Matsuo, *Rapid Communications in Mass Spectrometry*, 1988, **2**, 151-153.

3.   P. Jungblut, Bernd Thiede, *Mass Spectrometry Reviews*, 1997, **16**, 145-162.

4.   Y. Dai, R. M. Whittal and L. Li, *Analytical Chemistry*, 1999, **71**, 1087-1091.

5.   P. Chaurand, M. Stoeckli and R. M. Caprioli, *Analytical Chemistry*, 1999, **71**, 5263-5270.

6.   R. Kaufmann, D. Kirsch and B. Spengler, *International Journal of Mass Spectrometry and Ion Processes*, 1994, **131**, 355-385.

7.   P. Lecchi and L. K. Pannell, *Journal of the American Society for Mass Spectrometry*, 1995, **6**, 972-975.

8.   B. Finke, B. Stahl, A. Pfenninger, M. Karas, H. Daniel and G. Sawatzki, *Analytical Chemistry*, 1999, **71**, 3755-3762.

9.   Z. Joseph, *Mass Spectrometry Reviews*, 2004, **23**, 161-227.

10.   T. B. Farmer, Richard M. Caprioli, *Journal of Mass Spectrometry*, 1998, **33**, 697-704.

11.   P. H. Pevsner, J. Melamed, T. Remsen, A. Kogos, F. Francois, P. Kessler, A. Stern and S. Anand, *Biomarkers in Medicine*, 2009, **3**, 55-69.

12.   D. S. Cornett, M. L. Reyzer, P. Chaurand and R. M. Caprioli, *Nature Methods*, 2007, **4**, 828-833.

13. K. E. Burnum, S. L. Frappier and R. M. Caprioli, *Annual Review of Analytical Chemistry*, 2008, **1**, 689-705.

14. Y. Hsieh, J. Chen and W. A. Korfmacher, *Journal of Pharmacological and Toxicological Methods*, 2007, **55**, 193-200.

15. Y. Sugiura, S. Shimma and M. Setou, *Analytical Chemistry*, 2006, **78**, 8227-8235.

16. R. C. Beavis, T. Chaudhary B. T. Chait, *Organic Mass Spectrometry*, 1992, **27**, 156-158.

17. J. Kampmeier, K. Dreisewerd, M. Schürenberg and K. Strupat, *International Journal of Mass Spectrometry and Ion Processes*, 1997, **169-170**, 31-41.

18. G. H. Bird, A. R. Lajmi and J. A. Shin, *Analytical Chemistry*, 2002, **74**, 219-225.

19. K. B. Green-Church and P. A. Limbach, *Analytical Chemistry*, 1998, **70**, 5322-5325.

20. Y. J. Kim, A. Freas and C. Fenselau, *Analytical Chemistry*, 2001, **73**, 1544-1548.

21. S. L. Luxembourg, L. A. McDonnell, M. C. Duursma, X. Guo and R. M. A. Heeren, *Analytical Chemistry*, 2003, **75**, 2333-2341.

22. D. W. Armstrong, L.-K. Zhang, L. He and M. L. Gross, *Analytical Chemistry*, 2001, **73**, 3679-3686.

23. T. N. Laremore, Robert J. Linhardt, *Rapid Communications in Mass Spectrometry*, 2007, **21**, 1315-1320.

24. Y. Li, B. Shrestha and A. Vertes, *Analytical Chemistry*, 2008, **80**, 407-420.

25. Y. Li, B. Shrestha and A. Vertes, *Analytical Chemistry*, 2007, **79**, 523-532.

26. T.-C. Chiu, L.-C. Chang, C.-K. Chiang and H.-T. Chang, *Journal of the American Society for Mass Spectrometry*, 2008, **19**, 1343-1346.

27. S. Cha, Z. Song, B. J. Nikolau and E. S. Yeung, *Analytical Chemistry*, 2009, **81**, 2991-3000.

28. M. T. Spencer, H. Furutani, S. J. Oldenburg, T. K. Darlington and K. A. Prather, *The Journal of Physical Chemistry C*, 2008, **112**, 4083-4090.

29. J. Sunner, E. Dratz and Y.-C. Chen, *Analytical Chemistry*, 1995, **67**, 4335-4342.

30. M. J. Dale, R. Knochenmuss and R. Zenobi, *Analytical Chemistry*, 1996, **68**, 3321-3329.

31. S. Peng, Michael Edler, Norman Ahlmann, Thorsten Hoffmann, and Joachim Franzke, *Rapid Communications in Mass Spectrometry*, 2005, **19**, 2789-2793.

32. S. Zumbuhl, R. Knochenmuss, S. Wulfert, F. Dubois, M. J. Dale and R. Zenobi, *Analytical Chemistry*, 1998, **70**, 707-715.

33. H.-J. Kim, J.-K. Lee, S.-J. Park, H. W. Ro, D. Y. Yoo and D. Y. Yoon, *Analytical Chemistry*, 2000, **72**, 5673-5678.

34. K.-H. Park, Hie-Joon Kim, *Rapid Communications in Mass Spectrometry*, 2001, **15**, 1494-1499.

35. S. Cha and E. S. Yeung, *Analytical Chemistry*, 2007, **79**, 2373-2385.

36. H. Zhang, S. Cha and E. S. Yeung, *Analytical Chemistry*, 2007, **79**, 6575-6584.

37. M. Petkovic, J. Schiller, M. Müller, S. Benard, S. Reichl, K. Arnold and J. Arnhold, *Analytical Biochemistry*, 2001, **289**, 202-216.

38. S. Cha, Hui Zhang Hilal I. Ilarslan Eve Syrkin Wurtele Libuse Brachova Basil J. Nikolau Edward S. Yeung, *The Plant Journal*, 2008, **55**, 348-360.

39.   N. Buchner, A. Krumbein, S. Rohn, and L. W. Kroh, *Rapid Communications in Mass Spectrometry*, 2006, **20**, 3229-3235.

40.   S. C. Moyer and R. J. Cotter, *Analytical Chemistry*, 2002, **74**, 468 A-476 A.

41.   B. B. Schneider, C. Lock and T. R. Covey, *Journal of the American Society for Mass Spectrometry*, 2005, **16**, 176-182.

42.   P. V. Tan, V. V. Laiko and V. M. Doroshenko, *Analytical Chemistry*, 2004, **76**, 2462-2469.

43.   C. A. Miller, Donghui Yi Patrick D. Perkins, *Rapid Communications in Mass Spectrometry*, 2003, **17**, 860-868.
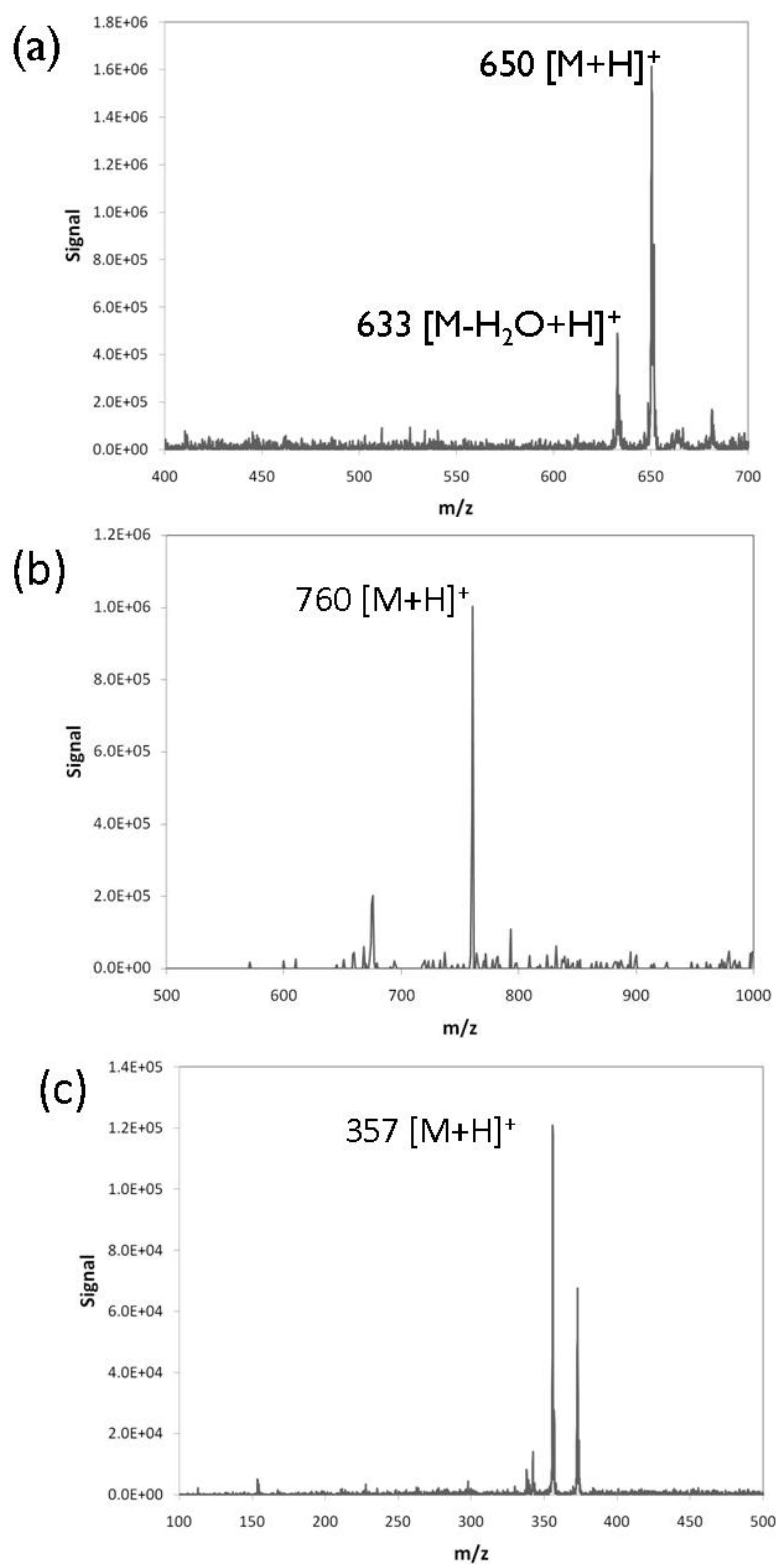
Figure 1. Positive ion mass spectrum of standards of sample load of (a) 24:0 ceramide, 50 ng (b) 1,2-diacyl-sn-glycerol-3-phosphocholine, 20 ng and (c) 1-oleoylglycerol, 20ng.
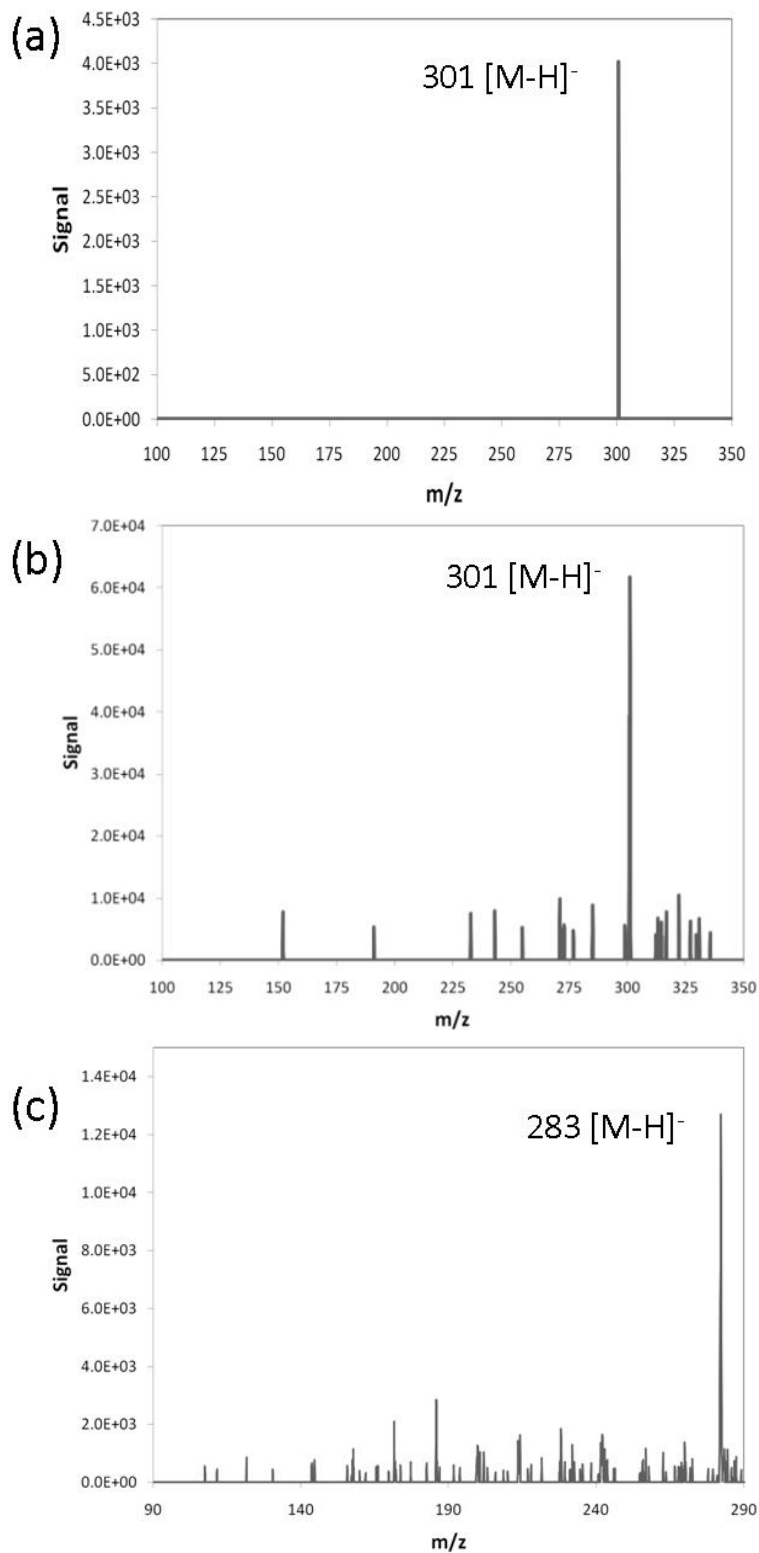
Figure 2. Negative ion mass spectra of (a) morin, 18 ng (b) quercetin, 20 ng and (c) stearic acid, 18 μg.
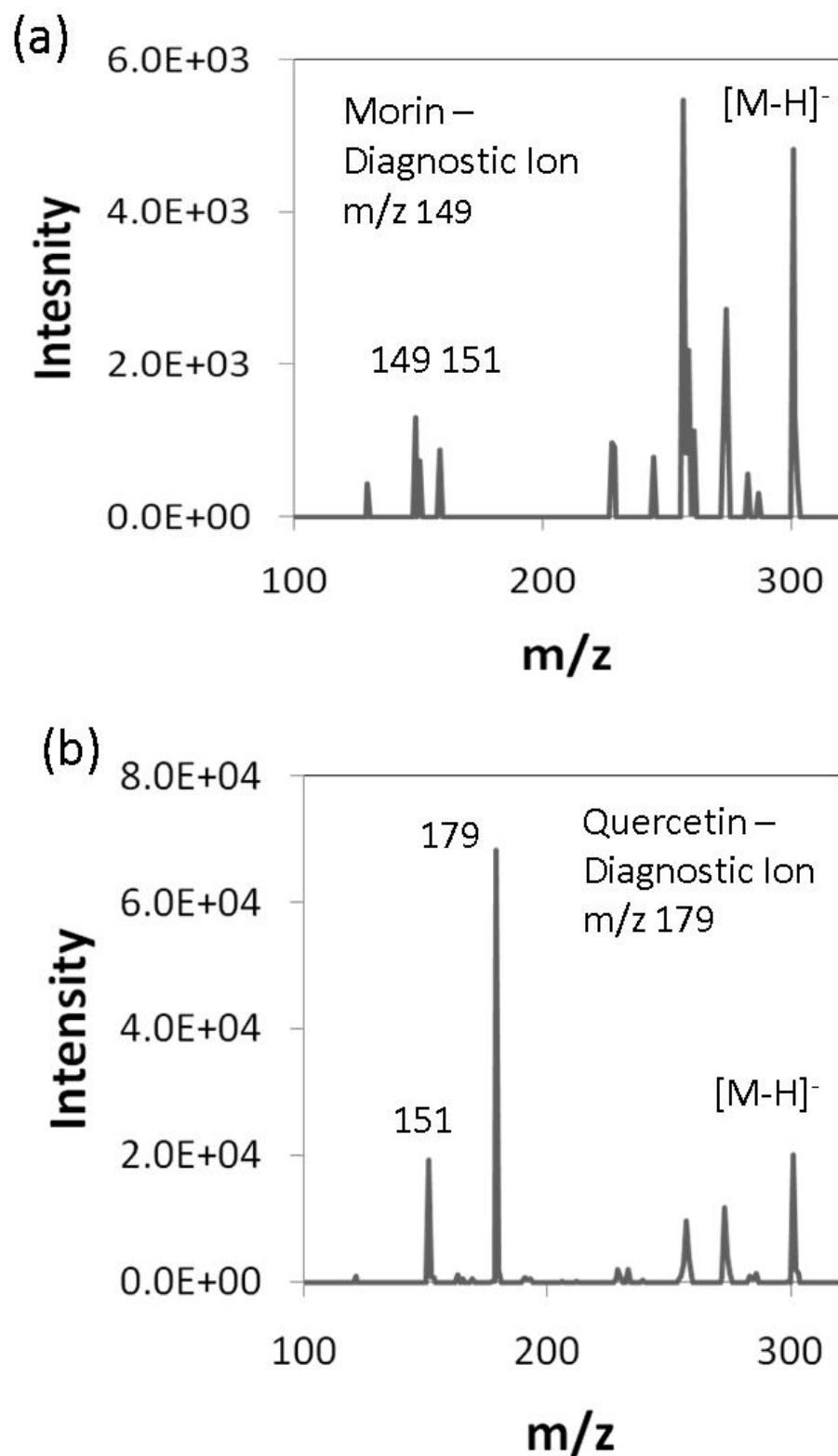
Figure 3. MS/MS spectra anthocyanin isomers (a) morin and (b) quercetin. The diagnostic fragment ion for anthocyanin molecules is m/z 151.
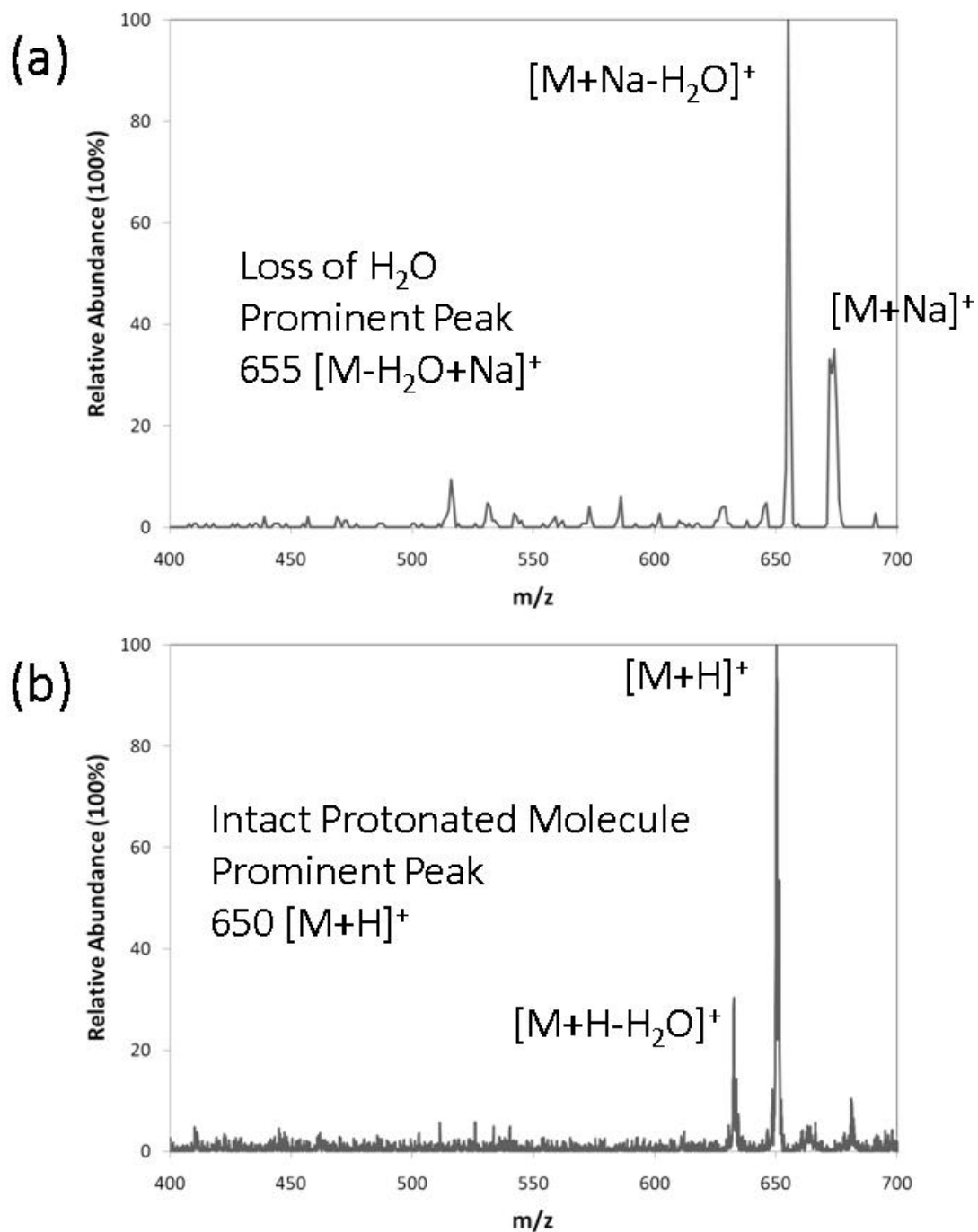
Figure 4. Mass spectra of 24:0 ceramide where ionization occurs at (a) intermediate pressure of 170 mTorr LTQ and (b) atmospheric pressure LCQ. The most prominent peak in the mass spectra is (a) loss of H_2O fragment ion and (b) intact molecular ion.
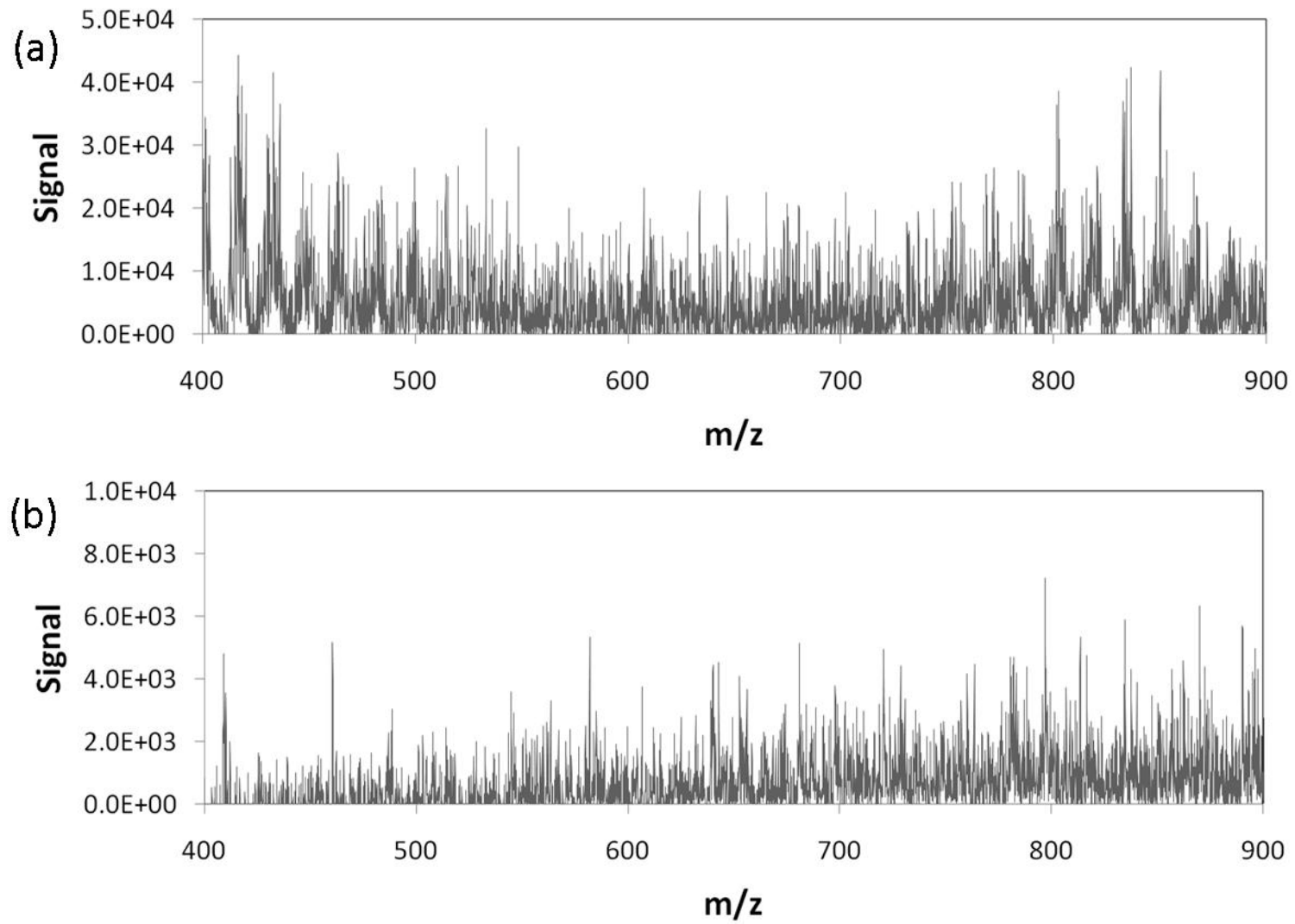
Figure 5. Mass spectra of total brain lipid extract using (a) colloidal graphite LDI and (b) DHB MALDI analysis.
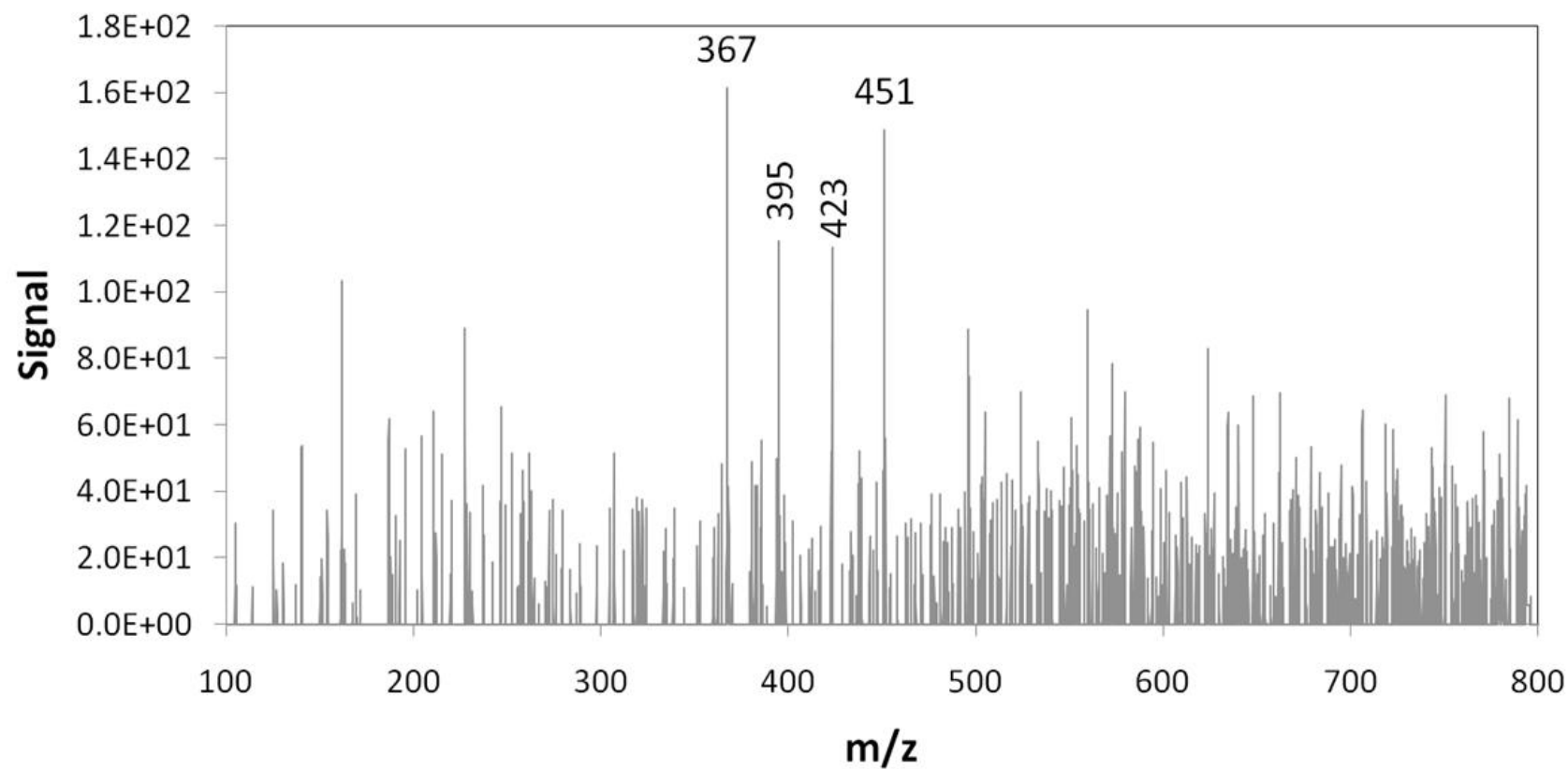
Figure 6. Mass spectrum of *Arabidopsis Thaliana* leaf using colloidal graphite LDI-MS in negative ion mode. Possible molecular identifications for peaks are m/z 367 [M-H]⁻ C24 fatty acid - tetracosanoic acid, m/z 395 [M-H]⁻C26 fatty acid - octacosanoic acid, m/z 423 [M-H]⁻C28 fatty acid - hexacosanoic acid, and m/z 451 [M-H]⁻ C30 fatty acid tricosanoic acid.
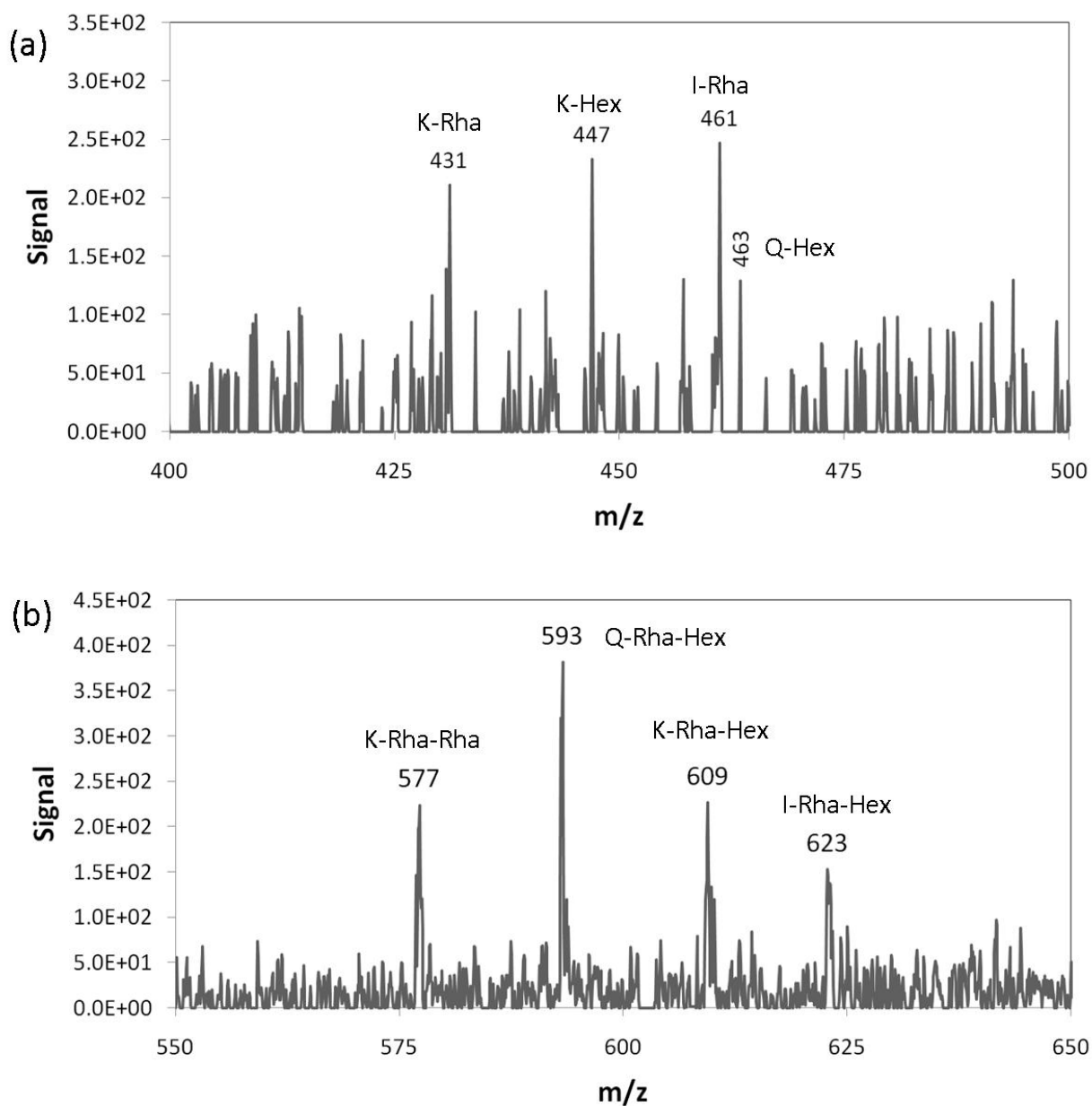
Figure 7. Mass spectra of *Arabidopsis Thaliana* flower petal using colloidal graphite in negative ion mode. Possible molecular identifications for assigned peaks for (a) are m/z 431 [M-H]⁻ Kaempferol-Rhamnoside, m/z 461 [M-H]⁻ Isorhamnnetin-Rhamnoside m/z 447 [M-H]⁻ Kaempferol-Hexoside, and m/z 463 [M-H]⁻ Quercertin-Hexoside. Possible molecular identifications for assigned peaks for (b) are m/z 577 [M-H]⁻Kaempferol-Rhamnoside-Rhamnoside, m/z 593 [M-H]⁻Kaempferol-Rhamnoside-Hexoside, m/z 609 [M-H]⁻ Quercetin-Rhamnoside-Hexoside, and m/z 623 [M-H]⁻ Isorhamnetin-Rhamnoside-Hexoside

CHAPTER 6 – TOWARD SINGLE CELL MASS SPECTRAL IMAGING: ASTROCYTE CELL IMAGING WITH COLLOIDAL SILVER LASER DESORPTION/IONIZATION MASS SPECTROMETRY

D. C. Perdian, Sangwon Cha, Jisun Oh, Don Sakaguchi, R. S. Houk, E. S. Yeung, and Young-Jin Lee*

Abstract

Mass spectral images of mouse brain Astrocyte cells are obtained in single-cell level with 25 µm spatial resolution using colloidal silver laser desorption/ionization mass spectrometry. The silver adduct ion of membrane bound cholesterol was used to monitor each single-cell. Good correlation between mass spectral and optical images at different cell concentration indicates its usefulness for single cell monitoring. In spite of a few technical limitations, semi-quantitative cholesterol distribution can be obtained on individual cell basis. This is the first time study of single cell level population of a molecular component using MALDI MS imaging.

*Corresponding Author

INTRODUCTION

The analysis of biological molecules by matrix-assisted laser desorption/ionization mass spectrometry (MALDI-MS) has led to many great developments in fundamental and applied research since the first experiments showing the power of MALDI-MS by Hillenkamp[1] and Tanaka[2]. MALDI-MS analysis has provided a robust tool for many biological and chemical fields including proteomics[3, 4], metabolomics[5-7], and polymer research[8-10]. MALDI-MS methods give scientists the ability to directly analyze samples in the localized area, and therefore have become the premier method for the mass spectral imaging of molecules *in situ* in biological tissues.[11] Use of mass spectrometry to gain spatial information of molecules of interest has become a popular research area because of its ability to offer insights into many biological processes.[12, 13] Imaging mass spectrometry (IMS) has been mostly employed using traditional MALDI matrices (sinapinic acid, α-cyano-4-hydroxycinnamic acid, 2,5-dihidroxy benzoic acid, etc.) to image proteins and peptides in biological tissues.[14, 15] The matrix can be applied by several methods: a matrix solution can be sprayed directly onto the sample; small aliquots of the matrix can be sequentially deposited to cover the sample; or a combination of the two methods can be used.[16] MALDI IMS experiments have been able to construct 3-dimensional images of protein expression in brain tissues by reconstructing multiple 2-dimensional images of thin layers of the tissue.[17]

Several new matrices have been developed and adopted for MALDI IMS experiments. Li and coworkers used IR-MALDI at atmospheric pressure to image plant metabolites using native water as IR absorbing matrix.[18, 19] Colloidal graphite has been used in IMS experiments to image cerebrosides in rat brain tissue[20], oligosaccharide molecules in

fruit[21], and plant metabolites in various plant organs[22]. Cha and coworkers recently adopted colloidal silver as a matrix to differentiate the surface wax metabolite distributions between a wild-type and mutant form of the *Arabidopsis Thaliana* plant.[23]

Spatial resolution in MALDI IMS experiments is often dictated by the laser spot size from which the analytes are desorbed and ionized. Typical values of spatial resolution for MALDI IMS experiments are in the $20 - 200$ µm range. Secondary ion mass spectrometry (SIMS) can achieve much higher spatial resolutions, <1µm, allowing image acquisition at the subcellular level.[24, 25] Recently, Piehowski and coworkers utilized MS/MS method to perform subcellular mapping of cholesterol on macrophage cells with C_{60} SIMS.[26] The In^+ SIMS source was able to achieve a spot size of roughly 200 nm. Typical MALDI instrumentation is not able to achieve laser spots sizes below the diffraction limit of the wavelength (usually 337 nm), but practical applications were mostly limited to even large dimensions, 100-200µm. Mass spectral analysis using MALDI as the ionization source has the advantage of being a much softer ionization source than SIMS methods and better sensitivity. For the majority of analytes of interest MALDI is able to produce primarily intact molecular ions, whereas the ionization mechanism for SIMS technique produces primarily fragment ions of the analyte of interest.

We achieved mass spectrometry imaging of 25 µm scale high spatial resolution and applied to study single cell imaging of Astrocyte cells. MALDI MS has typical detection limit of about subfemtomole, requiring minimum of $\sim 10^7$ molecules to detect a single cell. Cholesterol is a major component in cell membrane consisting up to 50% and is enough to be detected by mass spectrometry. The molecular images are generated from cholesterol-Ag

adduct ions using colloidal silver as matrix. The cell counts are compared with optical images showing plausibility of the method and also some limitations. Single-cell level distribution of cholesterol concentration was achieved for the first time in MALDI MS imaging.

EXPERIMENTAL SECTION

Chemicals. Sterol standards were purchased from Steraloids Inc. (Newport, RI USA). Poly-l-lysine was purchased from Sigma-Aldrich (St. Louis, MO USA). All solvents were purchased from Fischer Scientific (Fairlawn, NJ). MesoSilver, an aqueous colloidal silver solution was purchased from Purest Colloids, Inc. (Westampton, NJ USA). The colloidal silver is at a concentration of 20 ppm.

Colloidal Ag Spraying. The colloidal Ag is sprayed from a nebulizer with an uptake rate of 150 µL min^{-1}. 12. 5 µL aliquots of the colloidal silver are sprayed onto the sample eight times. The small volumes and multiple spraying events were used to ensure homogeneous sample coverage and inhibit aggregation of silver products during the evaporation of solvent. The spraying device for applying colloidal silver solution utilized a syringe pump (Kloehm Ltd., Las Vegas, NV), controlled by *WinPump* software, which was provided by Kloehm. The syringe pump was connected to a MicroFlow PFA-ST nebulizer (Elemental Scientific Inc., Omaha, NE) with a 0.25 mm i.d. sample uptake capillary. Helium was used as the nebulizing gas. The samples were placed 12.5 cm below the nebulizer. The size of the area

sprayed was much larger than the sample size, so the sample plates did not need to be moved during the spraying event.

Standard Cholesterol Sample Preparation. A 0.01% poly-L-lysine solution, mol wt 70,000-150,000, was applied to a stainless steel sample plate, covered and allowed to set for a period of three hours. The stainless steel plate was then washed with 18 MΩ H$_2$O. One μL cholesterol standard (0.1 mg/mL) was pipetted onto the poly-L-lysine-coated stainless steel sample plate. After drying, the sample was sprayed with colloidal Ag via the method described above.

Astrocyte Cells Sample Preparation. Astrocyte cells were dissected from the hippocampal region of mouse brain. The method used to extract the cells has been described previously.[27] Samples of varying cell concentration (6 x 10^3, 3 x 10^3, 1.5 x 10^3, 7.5 x 10^2 and 3.7 x 10^2 cells mL^{-1}) were deposited onto a poly-L-lysine coated stainless steel sample plate and a poly-L-lysine coated glass microscope slide. After culturing for 24 hours, cells were fixed in 4% paraformaldehyde in 0.1M phosphate buffer (pH 7.4) for 20 minutes and kept in 0.5% PFA. The samples were then dried under moderate vacuum (50 torr) for 30 minutes, and subsequently sprayed with colloidal Ag.

Mass Spectrometer. A Thermo Finnigan LTQ linear ion trap (Bremen, Germany) was used for mass analysis. The LTQ is fitted with a vMALDI source, which uses a N$_2$ laser (337 nm, 270 μJ/pulse, 20 Hz repetition rate) and maintains the sample at an intermediate pressure of

170 mTorr. A multi-mode optical fiber (OZ Optics, Ottawa, Ontario Canada) with a core

diameter of 50 μm was used to deliver the laser beam from the laser to the optics contained

in the mass spectrometer. The laser spot size is mostly determined by the laser optical fiber

diameter and it was measured by an optical microscope as 25 μm for the 50 μm size optical

fiber. The sample plate stage was moved in 25 μm increments for imaging. Three mass

spectra were collected in each position. Mass spectral images were produced using

ImageQuest software provided by Thermo Finnigan.

RESULTS AND DISCUSSION

To ensure homogeneous coverage of samples with colloidal Ag, a 1000 μm x 1000 μm area

of a sample spot of cholesterol (cholest-5-en-3β-ol) was analyzed by LDI-MS and a mass

spectral image was created (Fig. 1). The mass spectral image is created by transposing a

colorimetric plot of the signal ratio of cholesterol-Ag adduct ions and the average of total ion

count (TIC). In the colorimetric plot for this signal ratio ($[M+Ag]^{+}$/TIC) low signals are

represented by a blue color and high signal being represented by a red color. The median

signal/color combination is green. The subsequent 3-dimensional plot shows very good

signal homogeneity which is a reflection of how well the sample is covered by the colloidal

Ag and the reproducibility of the colloidal Ag LDI-MS technique.

Analysis of Astrocyte cells with colloidal Ag LDI-MS produces a mass spectrum

(Fig. 2) with ions that correspond to the cholesterol-Ag adduct ions. The peak at m/z 493

corresponds to the cholesterol and the ^{107}Ag isotope, and the peak at m/z 495 corresponds to

adduct ion of cholesterol and the ^{109}Ag isotope. The two other peaks of interest that should be

noted are the Ag_2^+ ions located at m/z 214, 216, and 218 for $^{107}Ag_2$, $^{107}Ag^{109}Ag$, $^{109}Ag_2$, respectively, and the Ag_3^+ ions observed at m/z 321, 323, 325, and 327 for $^{107}Ag_3$, $^{107}Ag_2{}^{109}Ag$, $^{107}Ag^{109}Ag_2$, $^{109}Ag_3$, respectively. These peaks can be used as bench marks to determine the quality of experimental parameters, and have also been used as reference peaks for relative concentration studies.[23]

The comparison of optical images on glass slides to the mass spectral images on stainless steel sample plates of cholesterol signal abundance reveals very similar-appearing images, especially at low concentrations (Fig. 3a-e). As the concentration of cells is decreased apparent correlation between the two images is observed. A more quantitative correlation between the two types of images is shown by the plot in Figure 4. In this plot, cells are counted manually in both optical and mass spectral images. In case of mass spectral images, there were cholesterol ion signals virtually everywhere, presumably coming from extracellular cholesterols leaked out of the cells. We arbitrarily defined that there is a cell if the signal ratio ($[M+Ag]^+$/TIC) is greater than a value of 15 and counted those pixels. A signal ratio level greater than 15 corresponds to $[M+Ag]^+$ peaks that are well above the signal-to-noise ratio and show good isotopic peak distributions, including ^{13}C peaks. Cells in the optical images were counted by hand. The optical images were divided into four equal quadrants and counted individually so that a standard deviation value could be determined. Standard deviations for the number of cells counted in the mass spectral images were calculated based on the analysis of three individual mass spectral images.

The optical images show linear relationships between the number of cell count and the cell concentration, suggesting that the sample preparation procedure was appropriate.

Mass spectral image also shows a linear relationship overall and there was a good agreement between the numbers of cells counted in both types of images, especially at the low concentrations of 3.7×10^2 and 7.5×10^2 cells mL^{-1}. It seems that the MS imaging overestimates the number of cells at the medium concentrations, 1.5×10^3 and 3×10^3 cells mL^{-1} and underestimates at the highest concentration, 6×10^3 cells mL^{-1}. This approach currently has several limitations in counting cells from the mass spectral images of cholesterol. At high concentrations, there is the possibility that two or more cells can overlap and therefore be counted as one cell, which explains why the number of cells levels off at the highest concentration. Cells that are larger than 25 μm or cells that occupy a region in more than one raster area can be sampled by the laser more than once which causes one real cell to be counted as two or more cells in the mass spectral image. There is also the possibility that a cell will not have a sufficient cholesterol concentration to be counted in the mass spectral image and in this case can lower the cell count.

The real advantage of this single cell mass spectral image comes from its ability to measure the cholesterol level on an individual cell basis. Figure 5 shows the cellular population of cholesterol levels. The plot of number of cells as a function of cholesterol levels shows that there is a greater than 2 orders of magnitude distribution of cholesterol concentration levels. The fact that cholesterol levels reported are referenced to the TIC which is primarily Ag-related ions, and that the homogeneity of colloidal Ag is high (as shown by Fig. 1) we have great confidence that the differences in cholesterol levels are a direct reflection of different concentrations in individuals cells. There are some limitations in this plot for the same reasons discussed above in counting the cells: i.e., if a cell occupies the

two pixels, its overall cholesterol level might have separated into two lower levels. In spite of this limitation, however, it shows a proof of concept that single cell mass spectral imaging can be used to monitor cholesterol level in single cell level. TOF-SIMS technique also could monitor the level of cholesterol in each single cell level at very high resolution ($<1\mu m$) without having problem of overlapping between the pixels (ref 25); however, it appears to have its own limitations of low sensitivity (a total ion count of only 20~30) and limited field of view to get a sufficient enough cell population. Once we overcome the current technical limitations, we believe our approach of using MALDI MS imaging for single cell has more promise because of better sensitivity and large field of view.

The current plot of cholesterol population (Fig. 5) uses arbitrary unit of signal ratios of $[M+Ag]^+$/TIC as individual cell concentration. Two methods are planned in the future for more accurate quantification of cholesterol levels in Astrocyte cells. The first method is to use an internal standard, such as deuterated cholesterol, add it to the cell culture for the known amount so that the cells can uptake the molecule. The internal standard could also be added to the colloidal Ag and sprayed homogenously across the entire sample and subsequently used to quantify cholesterol. Another method would be to measure the total concentration of cholesterol by using a bulk method of analysis to get an average cholesterol concentration. The cellular cholesterol population can be, then, normalized to give the average cholesterol concentration.

CONCLUSIONS

We achieved high spatial resolution of ~25μm in colloidal silver LDI-MS and applied it for mass spectral imaging of Astrocyte single cells. Although currently we have a few technical limitations, we demonstrated a proof of concept that this technique can be used to monitor single cells and achieve population of cholesterol in single cell level. We intend to overcome current limitations by achieving much higher spatial resolutions, down to 1-5μm using a Nd:YAG laser system.

ACKNOWLEDGEMENTS

REFERENCES

1. M. Karas, D. Bachmann and F. Hillenkamp, *Analytical Chemistry*, 1985, **57**, 2935-2939.

2. K. Tanaka, Hiroaki Waki, Yutaka Ido Satoshi, Akita Yoshikazu, Yoshida Tamio, Yoshida T. Matsuo, *Rapid Communications in Mass Spectrometry*, 1988, **2**, 151-153.

3. J. Rappsilber, M. Moniatte, M. L. Nielsen, A. V. Podtelejnikov and M. Mann, *International Journal of Mass Spectrometry*, 2003, **226**, 223-237.

4. M. Vestal and K. Hayden, *International Journal of Mass Spectrometry*, 2007, **268**, 83-92.

5. S. Vaidyanathan, Simon Gaskell, Royston Goodacre, *Rapid Communications in Mass Spectrometry*, 2006, **20**, 1192-1198.

6. *Journal of Proteome Research*, 2005, **4**, 215-218.

7. J. Szpunar, *The Analyst*, 2005, **130**, 442-465.

8. G. Montaudo, F. Samperi and M. S. Montaudo, *Progress in Polymer Science*, 2006, **31**, 277-357.

9. K. Jen Wu, and Robert W. Odom, *Analytical Chemistry*, 1998, **70**, 456A-461A.

10. D. Hercules, *Analytical and Bioanalytical Chemistry*, 2008, **392**, 571-573.

11. D. S. Cornett, M. L. Reyzer, P. Chaurand and R. M. Caprioli, *Nature Methods*, 2007, **4**, 828-833.

12. L. A. McDonnell, Ron M. A. Heeren, *Mass Spectrometry Reviews*, 2007, **26**, 606-643.

13. R. M. A. Heeren, D. F. Smith, J. Stauber, B. Kükrer-Kaletas and L. MacAleese, *Journal of the American Society for Mass Spectrometry*, 2009, **20**, 1006-1014.

14. P. Chaurand, M. Stoeckli and R. M. Caprioli, *Analytical Chemistry*, 1999, **71**, 5263-5270.

15. R. J. A. Goodwin, S. R. Pennington, and A. R. Pitt, *PROTEOMICS*, 2008, **8**, 3785-3800.

16. Y. Sugiura, S. Shimma and M. Setou, *Analytical Chemistry*, 2006, **78**, 8227-8235.

17. A. C. Crecelius, D. S. Cornett, R. M. Caprioli, B. Williams, B. M. Dawant and B. Bodenheimer, *Journal of the American Society for Mass Spectrometry*, 2005, **16**, 1093-1099.

18. Y. Li, B. Shrestha and A. Vertes, *Analytical Chemistry*, 2007, **79**, 523-532.

19. Y. Li, B. Shrestha and A. Vertes, *Analytical Chemistry*, 2008, **80**, 407-420.

20. S. Cha and E. S. Yeung, *Analytical Chemistry*, 2007, **79**, 2373-2385.

21. H. Zhang, S. Cha and E. S. Yeung, *Analytical Chemistry*, 2007, **79**, 6575-6584.

22. S. Cha, Hui Zhang Hilal I. Ilarslan Eve Syrkin Wurtele Libuse Brachova Basil J. Nikolau Edward S. Yeung, *The Plant Journal*, 2008, **55**, 348-360.

23. S. Cha, Z. Song, B. J. Nikolau and E. S. Yeung, *Analytical Chemistry*, 2009, **81**, 2991-3000.

24. S. G. Ostrowski, C. T. Van Bell, N. Winograd and A. G. Ewing, *Science*, 2004, **305**, 71-73.

25. S. G. Ostrowski, M. E. Kurczy, T. P. Roddy, N. Winograd and A. G. Ewing, *Analytical Chemistry*, 2007, **79**, 3554-3560.

26.   P. D. Piehowski, A. J. Carado, M. E. Kurczy, S. G. Ostrowski, M. L. Heien, N.

      Winograd and A. G. Ewing, *Analytical Chemistry*, 2008.

27.   J. B. Recknor, J. C. Recknor, D. S. Sakaguchi and S. K. Mallapragada, *Biomaterials*,
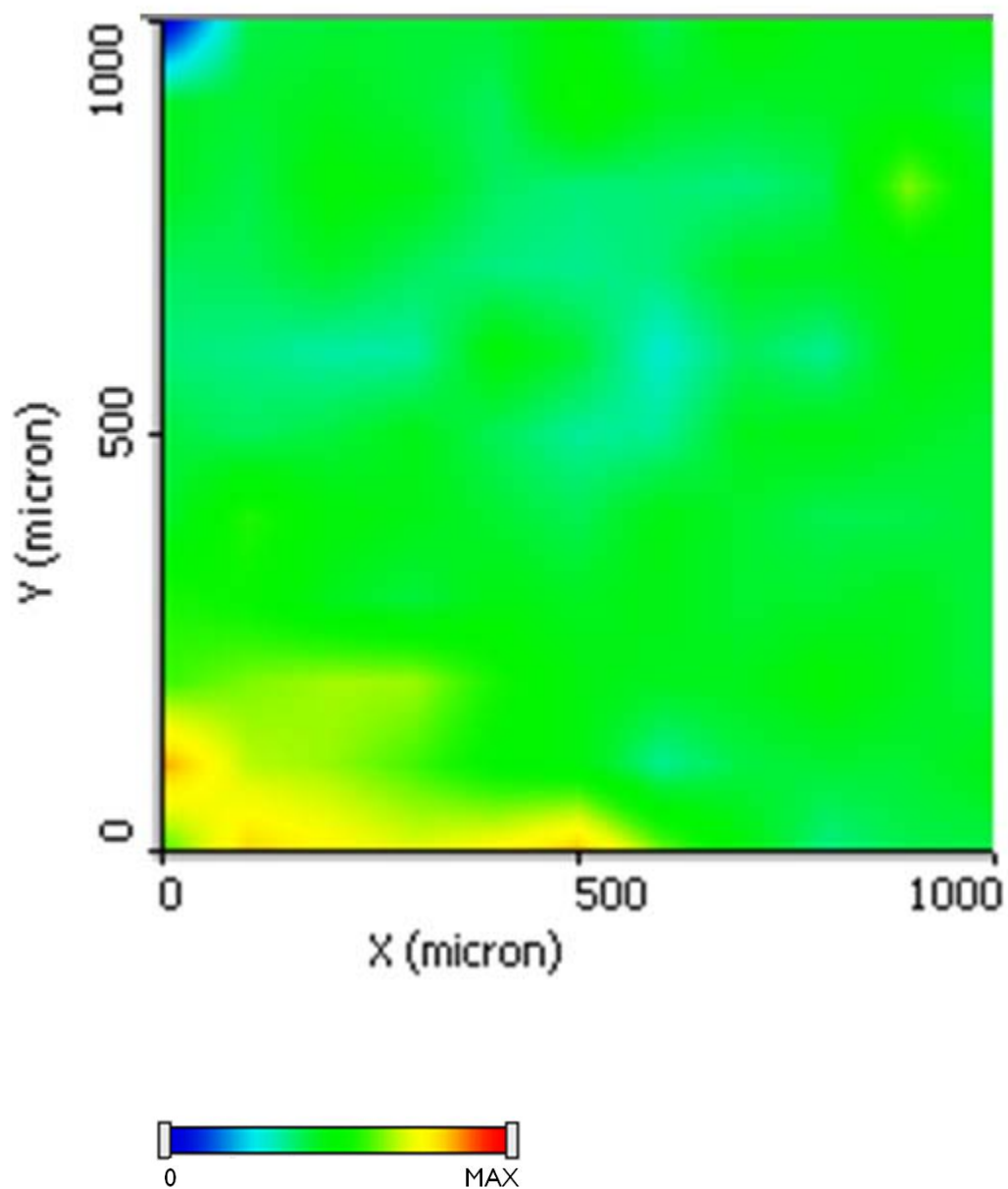
      2004, **25**, 2753-2767.

Figure 1. Mass spectral image illustrating homogeneity of colloidal Ag coverage on a cholesterol standard sample. MS image is 3-dimensional plot of [M+Ag]/TIC signal ratio.
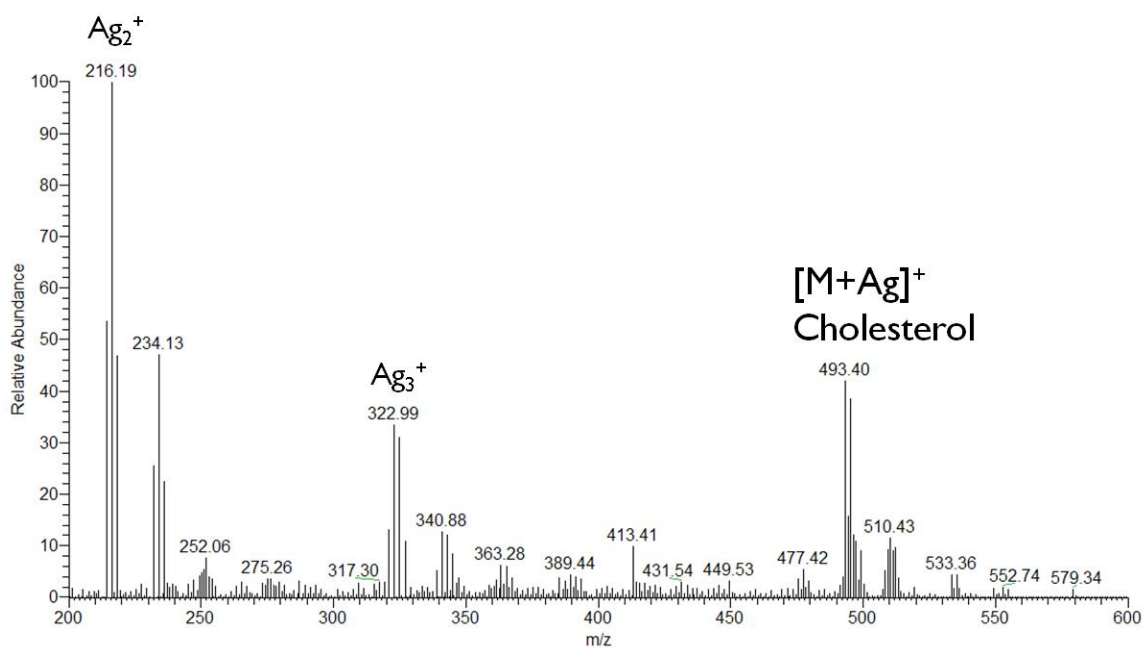
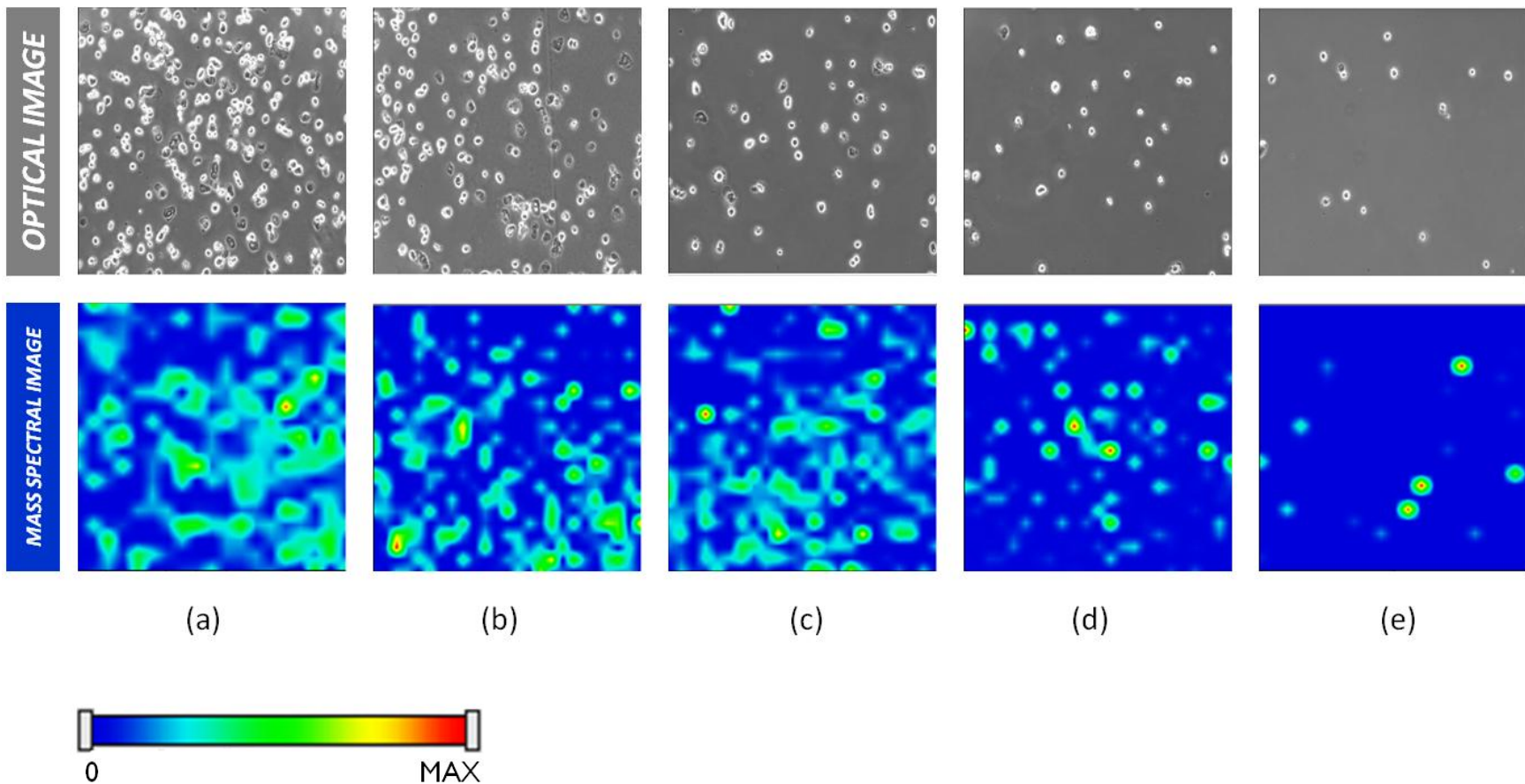Figure 2. Mass spectrum of colloidal Ag LDI-MS of Astrocyte Cell sample.

Figure 3. Comparison of optical images (on glass slide) taken of Astrocyte cells and mass spectral image (on stainless steel sample plate) of cholesterol in cells. MS image is 3-dimensional plot of [M+Ag]/TIC signal ratio. Cell concentrations for both images are (a) 6×10^3, (b) 3×10^3, (c) 1.5×10^3, (d) 7.5×10^2, and (e) 3.7×10^2 cells mL^{-1}.
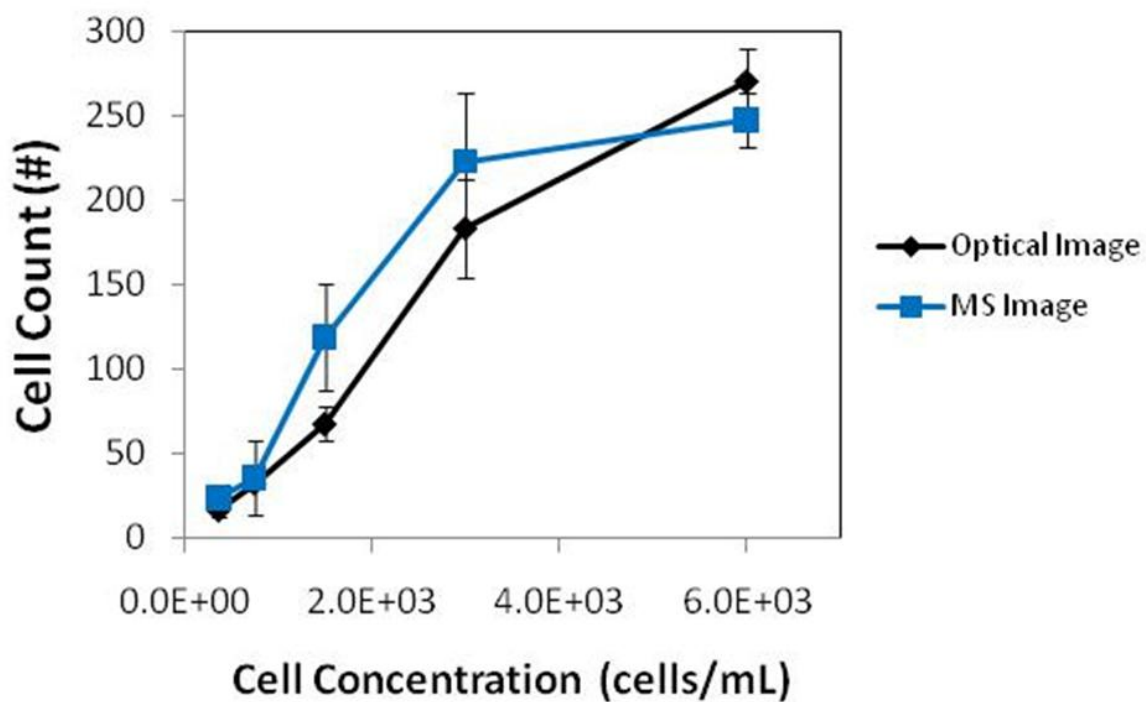
Figure 4. Comparison between the numbers of cells counted in optical image and mass spectrometry imaging. In MS imaging, cells were counted for those pixels having a $[M+Ag]+/TIC$ signal ratio greater than 15. Error bars correspond to one (1) standard deviation value.
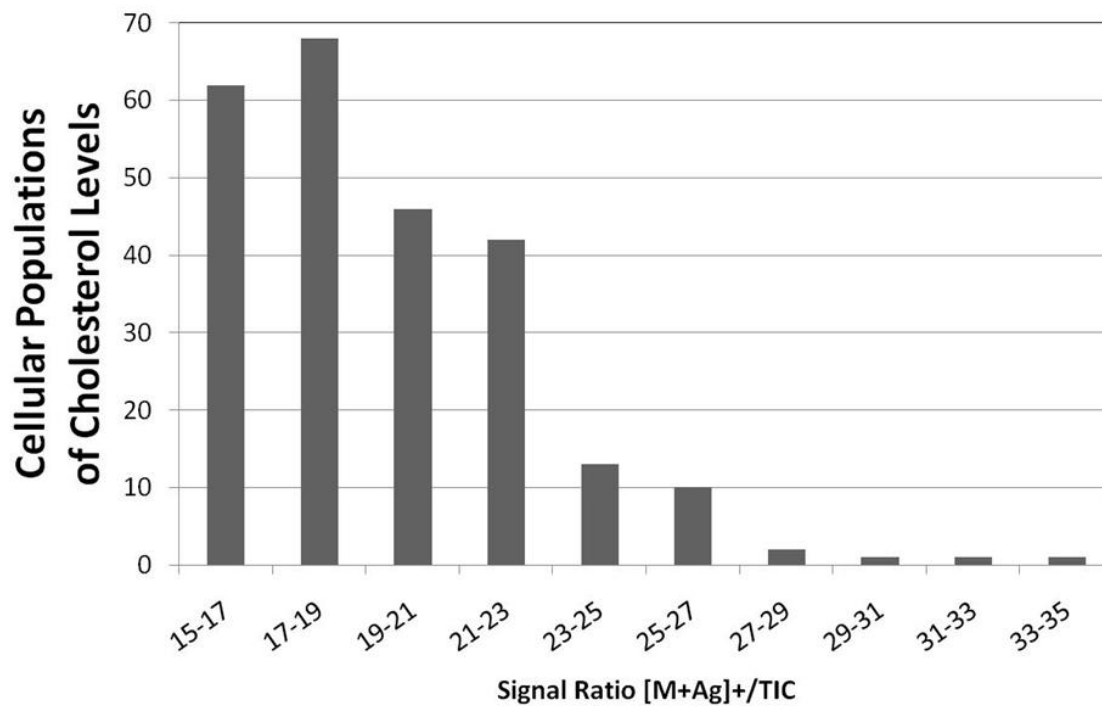
Figure 5. Cholesterol levels in individual cells from the mass spectral image in Fig. 3a as detected by colloidal Ag LDI-MS.

CHAPTER 7 – GENERAL CONCLUSIONS

Fundamental research and method development using mass spectrometry to directly analyze samples will have a significant impact on many fields and will help to answer questions and solve problems in biological, geological, medical, and countless other fields. Improvements of the figures of merit such as spatial resolution, sensitivity, and accuracy of quantification will further the ability of these analytical techniques to contribute to the scientific community and their ability to solve real world problems.

For the elemental analysis by LA-ICP-MS it was found that the experimental parameters that prove to reduce the effects of fractionation are the pulse length of the laser and the size of the aerosol particles that enter the plasma. Experimental/instrumental parameters such as the type of carrier gas used, the flow rate of the sample gas, laser raster rate, laser spot size, and the composition of the sample must also be carefully selected, however accurate quantification should be very possible with the use of fs lasers and limiting the size of aerosol particles that enter the plasma.

Molecular analysis by LDI-MS using colloidal graphite and colloidal silver shows promise to be able to answer biological questions. Performing the analysis at atmospheric pressure creates a softer ionization method, enables a higher throughput technique, and offers the ability to perform in vivo analysis. AP-LDI-MS techniques can be performed on MS instruments that can also be used with other ionization sources (ESI, APCI, APPI) which gives scientists more options when selecting an analytical method. Increasing the spatial resolution of these techniques will provide more information about biological processes.

ACKNOWLEDGEMENTS

First, I would like to thank Dr. R. S. Houk for guiding my research and scientific development while at Iowa State University. I would like to thank Mary Fassel for her supporting my education with the Mary K. and Velmer Fassel Fellowship. I am truly honored to have received the award. I would also like to thank all past and present Houk Group members for not only their help in my research endeavors but also for their friendship. Much of the research I conducted in LA-ICP-MS could not have been done without the help of Dan Zamzow, Stan Bajic, and David Baldwin, and so I owe them all many thanks for their assistance and helpful advice. I would like to thank Dr. Young-Jin Lee and his research group for their help in my research in LDI-MS and look forward to joining the group.

I would like to thank my parents who have always supported me in every aspect of my life. I would not be the person I am today if it wasn't for their unending love and guidance. They are truly great parents who showed me the importance of education, hard work, respect, and love of family and friends which are now attributes that help me in every aspect of my life. Last, but certainly not least, I want to thank my wife Kim for constantly supporting me during my graduate studies, I'm not sure if I could have finished without her. She is my best friend and the real reason why I moved to Iowa.